

**Microstructural Aspects of  
Localized Corrosion Behavior of Mg Alloys**

by

Peng-Wei Chu

A dissertation submitted in partial fulfillment  
of the requirements for the degree of  
Doctor of Philosophy  
(Materials Science and Engineering)  
in the University of Michigan  
2017

Doctoral Committee:

Associate Professor Emmanuelle Marquis, Chair  
Professor J. Wayne Jones  
Associate Professor Stephen Maldonado  
Professor Katsuyo Thornton

Peng-Wei Chu

[pengwchu@umich.edu](mailto:pengwchu@umich.edu)

ORCID iD: [0000-0002-8147-2880](https://orcid.org/0000-0002-8147-2880)

© Peng-Wei Chu 2017

## ACKNOWLEDGEMENTS

This dissertation would not be possible without the support of many individuals. First and foremost, I would like to thank my advisor, Professor Emmanuelle Marquis, for all her mentoring throughout the course of my Ph.D. training. She not only guides me through all the projects I worked on and polishes my written and oral skills, but also shows me how a scientist should be like. I would also like to thank my committee members, Professor J. Wayne Jones, Professor Katsuyo Thornton, and Professor Stephen Maldonado, for reading through my thesis and providing me all the insightful suggestions to complete this dissertation.

I acknowledge Magnesium Elektron Ltd and nanoMag LLC for providing the Mg alloys used in this study. I'm especially grateful to Dr. Ray Decker from nanoMag for giving me all the insights about biodegradable Mg alloys and showing me the passion a material scientist should have.

All current and former members of Marquis group are greatly appreciated for their support and friendship. Dr. Yimeng Chen, thank you for being my first mentor in the lab, showing me how to do APT, FIB, TEM, and working with me on the Ti precipitation project. I would like to give special acknowledgements to Andrew Chen, Lindsay Purvis-Kriss, and Etienne Le Mire for helping me with the Mg corrosion experiments. It would not be possible to finish all these experimental works without your help. I also thank Kathleen Chou for working with me on the Ti oxidation project and taking it over so I can focus on my Mg corrosion works. Lastly, I would like

to thank Dr. Kevin Fisher and Dr. Ellen Sitzmann-Solomon for their support and company, and I really enjoy our race to the finish line of Ph.D.

Many thanks to the staff of (MC)<sup>2</sup>, Dr. Allen Hunter, Dr. Haiping Sun, Dr. Kai Sun, Dr. Bobby Kerns, and Ying Qi, and the staff of CMSC at the University of Toledo, Dr. Joseph Lawrence and Dr. Sam Imanieh, for their help with microscope training and problem solving.

I also appreciate the Ministry of Education back in Taiwan for the generosity by providing me the Government Scholarship to Study Abroad, which supported my living expense for the first two years I'm in the US, especially when I was struggling to find an advisor in the first semester.

Finally, I would not be able to survive this journey without the support of all the friends I met here in Michigan and my family back in Taiwan. My lovely wife Yen-Ling Chang (Giselle), especially, thank you so much for letting me know how strong I can be when you're on my side.

## TABLE OF CONTENTS

ACKNOWLEDGEMENTS .....	ii
LIST OF TABLES .....	vii
LIST OF FIGURES .....	viii
LIST OF APPENDICES.....	xiv
LIST OF ABBRIVATIONS AND ACRONYMS .....	xv
ABSTRACT.....	xvi
INTRODUCTION .....	1
CHAPTER 1 : Corrosion Behavior and Mechanism of Pure Mg and Mg Alloys: Literature Review .....	3
1.1 Mg Alloys: with Great Potentials Comes Great Problems.....	3
1.2 Corrosion Behavior and Mechanism of Mg .....	4
1.2.1 Corrosion Reactions and Features on Mg .....	4
1.2.2 The Mystery: Negative Difference Effect (NDE) .....	6
1.2.3 Uni-Positive Magnesium (Mg <sup>+</sup> ) Model.....	8
1.2.4 Localized Corrosion and Enhanced Catalytic Activity Model.....	10
1.3 Effect of Alloy Chemistry and Microstructure on Corrosion of Mg Alloys .....	13
1.3.1 Role of Alloying Elements .....	13
1.3.2 Roles of Second Phases .....	15
1.3.3 Role of Grain Structure .....	19
1.4 Summary .....	21
CHAPTER 2 : Corrosion Microstructure and Behavior on a Heat-Treated Mg-Y-Nd-Zr Alloy. 22	
2.1 Motivation .....	22
2.2 Materials and Methods .....	23
2.2.1 Materials and Sample Preparation.....	23
2.2.2 Corrosion Tests and In-Situ Observation .....	24

2.2.3 Microstructure Characterization .....	25
2.3 Results .....	26
2.3.1 Microstructure of the Heat-Treated WE43 Alloy before Corrosion Testing .....	26
2.3.2 Corrosion Rate Measurements .....	28
2.3.3 Characterization of the Corrosion Products .....	30
2.4 Discussion .....	39
2.5 Conclusions .....	43
CHAPTER 3 : Hydrogen Evolution and Localized Corrosion during Anodic Polarization of a Peak-Aged Mg-Y-Nd-Zr Alloy.....	45
3.1 Motivation .....	45
3.2 Materials and Methods .....	46
3.2.1 Materials and Sample Preparation.....	46
3.2.2 Electrochemical Tests.....	46
3.2.3 Microstructure Characterization.....	47
3.3 Results .....	48
3.3.1 Hydrogen Evolution Rate under Galvanostatic Polarization.....	48
3.3.2 Localized Corrosion Induced by Anodic Polarization .....	52
3.3.3 Microstructure of the Localized Corrosion .....	55
3.3.4 Cathodic Response of Anodic Polarized Samples .....	61
3.4 Discussion .....	64
3.5 Conclusions .....	66
CHAPTER 4 : Microstructure of Localized Corrosion Front on Pure Mg, Mg-Zn-Ca-Mn, and Mg-Y Alloys .....	68
4.1 Motivation .....	68
4.2 Materials and Methods .....	69
4.2.1 Materials and Sample Preparation.....	69
4.2.2 Corrosion and Electrochemical Tests.....	69
4.2.3 Microstructure Characterization.....	71
4.3 Results .....	72
4.3.1 Alloy Microstructures.....	72
4.3.2 Localized Corrosion and Hydrogen Evolution Sites .....	75

4.3.3 Microstructure Characterization of Localized Corrosion Fronts.....	77
4.3.4 Hydrogen Evolution Responses under Anodic Polarization .....	86
4.4 Discussion .....	88
4.5 Conclusions .....	92
CHAPTER 5 : Summary and Future Directions.....	93
5.1 Summary .....	93
5.2 Future Directions.....	95
5.2.1 Corrosion Mechanisms.....	95
5.2.2 Alloy Investigation and Design .....	97
APPENDICES .....	101
BIBLIOGRAPHY .....	106

## LIST OF TABLES

Table 2.1 Chemical composition and impurity level of WE43 alloy as measured by ICP-MS. ..	23
Table 2.2 Corrosion current densities and corrosion rates measured by linear Tafel extrapolation. .....	29
Table 2.3 Chemical composition analysis by EDS for the dome and the underlying particles. (The EDS spectra are shown in Fig. 2.6(b) and (c))......	35
Table 3.1 EDS chemical composition of the localized corrosion region after anodic galvanostatic polarization at 1 mA/cm <sup>2</sup> for 5 seconds averaged from 25 separate measurements.....	61
Table 3.2 Current densities at -2.3 V vs SCE for cathodic polarization measurements on anodic polarized samples after 2 C/cm <sup>2</sup> of charge passed.....	62
Table 4.1 Chemical composition and impurity level of the studied Mg alloys measured by ICP- MS (wt%)......	70



## LIST OF FIGURES

Figure 1.1 Pourbaix (E-pH) diagram of Mg (reproduced from Ref. [1] with permission).....	5
Figure 1.2 Schematic illustration of negative difference effect (NDE) on Mg (reproduced from Ref. [11] with permission).....	7
Figure 1.3 Schematic illustration of the corrosion mechanism of Mg involving uni-positive $Mg^+$ ion (reproduced from Ref. [11] with permission). Production of univalent $Mg^+$ ion (reaction 1.8) was proposed to occur in a film-free region on Mg surface. ....	9
Figure 1.4 Schematic illustration of the localized corrosion mechanism of Mg with enhanced catalytic activity (reproduced from Ref. [19] with permission). A film-free region was proposed at the localized corrosion front where Mg dissolves into the solution. ....	11
Figure 1.5 A compilation of alloying elements effect on the cathodic and anodic reaction rates of Mg (reproduced from Ref. [8] with permission). ....	15
Figure 1.6 Corrosion rates as a function of alloying element concentrations in Mg. The corrosion rate dramatically increases upon exceeding the tolerance limit (reproduced from Ref. [1] with permission).....	16
Figure 1.7 Collection of polarization curves of common second phases in Mg alloys (reproduced from Ref. [8] with permission). ....	18
Figure 1.8 Schematic illustration of corrosion barrier effect for Mg <sub>17</sub> Al <sub>12</sub> phase in die-cast AZ91 alloy (reproduced from Ref. [11] with permission). ....	19
Figure 2.1 Secondary electron (SE) SEM images of as-polished surfaces from the (a) solution-treated and (b) peak-aged WE43 showing Y-rich and Zr-rich particles. (c) Back-scattered electron (BSE) SEM image of peak-aged WE43 showing the fine scale $\beta_1$ and $\beta$ precipitates throughout the grains and along the grain boundaries. ....	27
Figure 2.2 (a) The open circuit potential evolution in 3.5 wt% NaCl solution saturated with $Mg(OH)_2$ (T=21°C). (b) Cathodic polarization curves in the test solution after 24 hours of	

immersion. (c) Representative hydrogen evolution curves and (d) the estimated average corrosion rates from seven measurements (the error bars are the standard deviations). .....	29
Figure 2.3 in situ observation of the corrosion morphology on (a) solution-treated and (b) peak-aged WE43 after 100 hours of immersion showing a uniform corrosion morphology and hydrogen bubbles. ....	31
Figure 2.4 SEM surface images of the corrosion morphologies after 1 hour and 6 hours of immersions for solution-treated and peak-aged WE43 alloys. The labels “thin” and “thick” in (c) indicate regions with thin and thick surface films, respectively. ....	32
Figure 2.5 SEM image of a protruding dome formed on peak-aged WE43 after 24 hours of immersion. (Stage tilt = 52°).....	32
Figure 2.6 (a) Cross sectional STEM images of a protruding dome and the underlying particles of solution-treated WE43 after 1 hour immersion. EDS spectra for (b) the underlying particles and (c) the dome (quantitative analysis of the EDS spectra are shown in Table 2.3), and (d)-(f) electron diffraction pattern evolution of the dome from inner to outer portions. (Elements in the spectra which are not included in the quantification are from the TEM sample holder (Cu and Al), contamination during sample preparation (Si), carbon deposition during imaging (C) and Ga damage during ion milling (Ga).) .....	34
Figure 2.7 Cross sectional SEM/FIB images illustrating the local protecting effect of the dome on peak-aged WE43 after 5 days of immersion. ....	35
Figure 2.8 Cross sectional TEM images of the corrosion films after 1 hour and 6 hours of immersion for solution-treated and peak-aged WE43 alloy. (c) and (e) are from the thin and thick regions indicated in Fig. 2.4(c). ....	37
Figure 2.9 Electron diffraction patterns of (a) outer and (b) inner layers, and (c) the EDS compositional depth profile of the corrosion film on solution-treated WE43 after 6 hours of immersion shown in Fig. 2.8(c). ....	38
Figure 2.10 EDS mapping of the corrosion film on peak-aged WE43 after 6 hours of immersion. ....	38
Figure 2.11 Schematic illustration of the proposed corrosion models. (a) Microgalvanic effect of the Zr-rich particles and (b) corrosion film formation mechanism and the effect of the finely dispersed precipitates on the corrosion evolution. ....	42

Figure 3.1 Volume of evolved hydrogen collected as a function of application time for peak-aged Mg-Y-Nd-Zr alloy in 0.1M NaCl solution under galvanostatic polarization at different (a) cathodic and (b) anodic current densities. A total charge of 15 C/cm<sup>2</sup> was applied. .... 49

Figure 3.2 Average hydrogen evolution rates, calculated by averaging the slopes between each data points in Fig. 3.1, as a function of applied current density. The error bars shown here are the standard deviations of the slopes. .... 50

Figure 3.3 (a) Applied current density,  $i_{\text{appl}}$ , and current density inferred from hydrogen evolution rate,  $i_{\text{H}_2}$ , as a function of steady state potential. The potential values are not corrected for ohmic potential drops. (b) Ratio of the current density calculated from hydrogen evolution rate to the applied current density,  $i_{\text{H}_2}/i_{\text{appl}}$ , as a function of applied current density. .... 51

Figure 3.4 Evolution of the potential under galvanostatic anodic polarization for different applied current densities. The potentials here are not corrected for ohmic potential drops. .... 52

Figure 3.5 In situ OM observations. (a) Image taken at 2 seconds under anodic polarization at 1 mA/cm<sup>2</sup>. (b) The same area after 60 seconds of anodic polarization. The image was taken after the polarization stopped. .... 54

Figure 3.6 Surface morphology after galvanostatic anodic polarization at (a) 0.25, (b) 0.5, (c) 2.5 and (d) 10 mA/cm<sup>2</sup> (Charge passed: 15 C/cm<sup>2</sup>). .... 55

Figure 3.7 Same localized corrosion region formed after anodic polarization at 1 mA/cm<sup>2</sup> for 5 seconds imaged with (a) top-view SEM image using the secondary electron (SE) detector, (b) cross sectional SEM image using the SE detector showing the finger-like corrosion front morphology, and (c) cross sectional high angle annular dark field (HAADF) STEM image showing the finely dispersed precipitates presented in both the corrosion region and WE43 matrix. Yellow dashed line outlines the interface between corrosion region and WE43 matrix. .... 57

Figure 3.8 Cross sectional bright field (BF) TEM image of the edge of the same localized corrosion region (the box shown in Fig. 3.7(b)) formed after anodic polarization at 1 mA/cm<sup>2</sup> for 5 seconds showing the porous structure and finger-like features. Yellow dashed line outlines the interface between corrosion region and WE43 matrix. .... 58

Figure 3.9 Cross sectional SEM/FIB images showing the evolution of localized corrosion regions after anodic polarization at 1 mA/cm<sup>2</sup> for (a) 5, (b) 30 and (c) 120 seconds. (Another trench is also present on the opposite side in (a) because this is during a TEM specimen preparation.) .... 59

Figure 3.10 (a) SE, (b) STEM cross sectional images, and (c)-(f) the corresponding elemental EDS maps taken from the edge of the same localized corrosion region (the box shown in Fig. 3.7(b)) formed after anodic polarization at 1 mA/cm<sup>2</sup> for 5 seconds. Yellow dashed line in (b) outlines the interface between corrosion region and WE43 matrix, which was determined using the O map. 60

Figure 3.11 Selected area electron diffraction (SAED) from the corrosion region compared to Mg(OH)<sub>2</sub> diffraction ring pattern generated from Powder Diffraction File 44-1482. .... 61

Figure 3.12 (a) Selected cathodic polarization curves of samples without prior polarization and after anodic polarization with 2 C/cm<sup>2</sup> of charge passed, and the corresponding surface morphology right before cathodic polarization test for samples (b) anodic polarized at 10 mA/cm<sup>2</sup> for 2 C/cm<sup>2</sup> and (c) immersed at open circuit for 10 minutes. .... 63

Figure 4.1 Grain structure of the investigated alloys. (a) pure Mg, (b) Mg-Zn-Ca-Mn, and (c) Mg-Y alloys. (a) and (c) are optical microscopy (OM) images, and (b) is a SEM secondary electron (SE) image. Samples were etched with Acetic Glycol for 10 seconds. .... 73

Figure 4.2 (a) a SEM back-scattered electron (BSE) image of a Fe-rich impurity particle on pure Mg. (b) high angle annular dark field (HAADF) STEM image of the precipitates structure in Mg-Zn-Ca-Mn alloy with the corresponding EDS elemental maps of Mn, Zn, and Ca. (c) phase-contrast bright field (BF) STEM image of a grain boundary in Mg-Zn-Ca-Mn alloy with the corresponding EDS elemental maps of Zn and Ca. .... 74

Figure 4.3 (a) APT reconstruction of a volume containing a grain boundary with Y segregation. (b) 1D concentration profile across the grain boundary (obtained using a cylinder of 10 nm diameter). .... 75

Figure 4.4 Surface corrosion morphology of (a) pure Mg, (b) Mg-Zn-Ca-Mn alloy, and (c) Mg-Y alloys immersed in 1M NaCl solution for 1 hour. White arrows indicate the localized corrosion regions. Dashed curve in (a) marked the circular propagation front. .... 76

Figure 4.5 High magnification observation of actively propagating fronts of the localized corrosion on (a) pure Mg, (b) Mg-Zn-Ca-Mn, and (c) Mg-Y alloys in 1M NaCl solution. Red arrows indicate the propagation direction of localized corrosion. .... 78

Figure 4.6 High magnification observation of actively propagating localized corrosion regions on Mg-Zn-Ca-Mn alloy in 0.1M NaCl solution under anodic polarization at 1 mA/cm<sup>2</sup> for 300 seconds. Regions arrowed in the figure indicate some of the hydrogen evolution sites. .... 79

Figure 4.7 Surface corrosion morphology observed by SEM for (a) pure Mg, (b) Mg-Zn-Ca-Mn, and (c) Mg-Y alloys in 0.1M NaCl solution after anodic polarization at 10 mA/cm<sup>2</sup> for 100 seconds. Regions arrowed in the figure indicate some of the localized corrosion regions. (All images are secondary electron images taken with 5kV electron beam using Everhart-Thornley detector.) .. 80

Figure 4.8 Cross sectional SEM image of an actively propagating localized corrosion front on Mg-Zn-Ca-Mn alloy immersed in 1M NaCl solution for 1 hour. The red arrow indicates the propagation direction. (Secondary electron image taken with 5kV electron beam using through lens detector.) ..... 81

Figure 4.9 Cross sectional SEM image of a propagating localized corrosion region for (a) pure Mg, (c) Mg-Zn-Ca-Mn, and (e) Mg-Y alloys in 0.1M NaCl solution after anodic polarization at 10 mA/cm<sup>2</sup> for 100 seconds. The red arrows indicate the propagation direction. (All images are secondary electron images taken with 5kV electron beam using through lens detector.) ..... 81

Figure 4.10 (a) Corrosion morphology of a Mg-Y sample after free immersion in 1M NaCl solution for 100 minutes and (b) the corresponding EBSD grain orientation map. (c) and (d) Cross sectional SEM images of localized corrosion fronts stopping at grain boundaries (secondary electron images taken with 5kV electron beam using through lens detector). Locations of the cross sections are indicated by the white rectangles in (a). ..... 82

Figure 4.11 (a) High magnification bright field (BF) TEM image of the localized corrosion region on Mg-Zn-Ca-Mn alloys immersed in 1M NaCl solution for 1 hour and (b) the corresponding electron diffraction pattern. The reference Mg(OH)<sub>2</sub> diffraction ring pattern was generated from Powder Diffraction File 44-1482. Cross sectional (c) secondary electron (SE) and (d) high angle annular dark field (HAADF) STEM image of the active propagating localized corrosion front with the corresponding EDS elemental maps of (e) O, (f) Mg, (g) Cl, and (h) Zn. The red arrows in (c) and (d) indicate the propagation direction. Dashed lines in (c) and (d) outline the interface between film/localized corrosion region and localized corrosion region/alloy, respectively. .... 84

Figure 4.12 Cross sectional (a) bright field (BF) TEM, (c) secondary electron (SE), and (d) high angle annular dark field (HAADF) STEM images of an actively propagating localized corrosion front on Mg-Zn-Ca-Mn alloys in 0.1M NaCl solution after anodic polarization at 10 mA/cm<sup>2</sup> for 100 seconds, and (b) the corresponding electron diffraction pattern of the corrosion region and EDS elemental maps of (e) O, (f) Mg, (g) Cl, and (h) Zn. The reference Mg(OH)<sub>2</sub> diffraction ring pattern was generated from Powder Diffraction File 44-1482. The red arrows in (a), (c), and (d)

indicate the propagation direction. Dashed lines in (a) and (d) outline the interface between localized corrosion region and alloy. .... 85

Figure 4.13 (a) Average hydrogen evolution rates of the investigated alloys in 0.1M NaCl and 0.1M Na<sub>2</sub>SO<sub>4</sub> solutions as a function of applied anodic current density. The error bars shown here are the standard deviations of the slopes during collection of hydrogen as described in previous chapter. (b) Comparison of average hydrogen evolution rates and amounts of Mg<sup>2+</sup> dissolved in the test solutions to the applied current density. (A total charge of 10 C/cm<sup>2</sup> was passed for all tests.) ..... 87

Figure 5.1 Schematic illustration of corrosion mechanism on Mg alloys. (a) to (d) shows the temporal evolution of a Mg alloy immersed in a NaCl solution. The grain on the right shows the microgalvanic effect induced by the impurity particles, while the grain on the left shows the localized corrosion propagation inside the alloy. .... 99

Figure A.1 Ga ion beam damage during cross sectional TEM sample preparation in SEM/FIB. (a) and (d) cross sectional TEM samples prepared with and without cryogenic SEM/FIB stage, respectively, (b) and (e) same region as (a) and (d) after 40 minutes continuous TEM observation, (c) and (f) selected area diffraction pattern for the corrosion film shown in (a) and (d). .... 102

Figure A.2 Electron beam damage during cross sectional STEM observation. (a) and (b) cross sectional images before and after 50 minutes of continuous observation without cryogenic TEM stage, (c) and (d) cross sectional images before and after 50 minutes of continuous observation with cryogenic TEM stage. (Continuous STEM observation parameters: 512x512 with pixel dwell time 1000 μs.) ..... 103

Figure A.3 (a) MgO and (b) Mg(OH)<sub>2</sub> powders used for preparation of TEM specimens, and locations of the EDS quantification (outlined with blue lines) used for O/Mg ratio on (c) MgO and (d) Mg(OH)<sub>2</sub> specimens. .... 105

## LIST OF APPENDICES

Appendix I Mitigation of Ion and Electron Beam Damage on the Corrosion Film with Cryogenic Stage.....	101
Appendix II Calibration of X-Ray EDS Quantification with MgO and Mg(OH) <sub>2</sub> Powders in STEM .....	104

## LIST OF ABBRIVATIONS AND ACRONYMS

APT: Atom Probe Tomography  
BF: Bright Field  
BSE: Back-Scattered Electron  
CCD: Charge Coupled Device  
DF: Dark Field  
EBSD: Electron Back-Scattered Diffraction  
EDS: Energy Dispersive Spectroscopy  
EIS: Electrochemical Impedance Spectroscopy  
FIB: Focused Ion Beam  
GB: Grain Boundary  
HAADF: High Angel Annular Dark Field  
ICP-MS: Inductively Coupled Plasma-Mass Spectroscopy  
NDE: Negative Difference Effect  
OCP: Open Circuit Potential  
OM: Optical Microscopy  
SAED: Selected Area Electron Diffraction  
SCE: Saturated Calomel Electrode  
SE: Secondary Electron  
SECM: Scanning Electrochemical Microscopy  
SEM: Scanning Electron Microscopy  
SHE: Standard Hydrogen Electrode  
STEM: Scanning Transmission Electron Microscopy  
SVET: Scanning Vibrating Electrode Technique  
TEM: Transmission Electron Microscopy



## ABSTRACT

Combining high specific strength and unique electrochemical properties, magnesium (Mg) alloys are promising lightweight materials for various applications from automotive, consumer electronics, biomedical body implant, to battery electrodes. Engineering solutions such as coatings have enabled the use of Mg alloys, despite their intrinsic low corrosion resistance. Consequently, the fundamental mechanisms responsible for the unique localized corrosion behavior of bare Mg alloys, the associated abnormal hydrogen evolution response, and the relationships between corrosion behavior and alloy microstructure are still unsolved.

This thesis aims to uncover the specificities of Mg corrosion and the roles of alloy chemistry and microstructure. To this end, multiscale site-specific microstructure characterization techniques, including *in situ* optical microscopy, scanning electron microscopy with focused ion beam milling, and transmission electron microscopy, combined with electrochemical analysis and hydrogen evolution rate monitoring, were performed on pure Mg and selected Mg alloys under free corrosion and anodic polarization, revealing key new information on the propagation mode of localized corrosion and the role of alloy microstructures, thereby confirming or disproving the validity of previously proposed corrosion models.

Uniform surface corrosion film on Mg alloys immersed in NaCl solution consisted a bi-layered structure, with a porous Mg(OH)<sub>2</sub> outer layer on top of a MgO inner layer. Presence of fine scale precipitates in Mg alloys interacted with the corrosion reaction front, reducing the

corrosion rate and surface corrosion film thickness. Protruding hemispherical dome-like corrosion products, accompanied by growing hydrogen bubbles, formed on top of the impurity particles in Mg alloys by deposition of  $\text{Mg}(\text{OH})_2$  via a microgalvanic effect. Localized corrosion on Mg alloys under both free immersion and anodic polarization was found to be governed by a common mechanism, with the corrosion front propagating laterally a few  $\mu\text{m}$  inside the alloy and underneath the surface corrosion film, with finger-like features aligned with (0001) Mg basal planes at the localized corrosion/alloy interface. Rising streams of hydrogen bubbles were found to follow the anodic dissolution of Mg and formation of  $\text{Mg}(\text{OH})_2$  corrosion products at the propagating localized corrosion fronts. Alloying elements segregation to the grain boundaries showed the ability to stop localized corrosion propagation momentarily.

By revealing the microstructure of corrosion features on Mg alloys, a descriptive model was proposed. Relationships between the corrosion behavior and alloy microstructures were also identified. This microscopic information can serve as a guideline for future development of Mg alloys by tailoring the microstructure to achieve proper corrosion responses for applications under different environments.

## INTRODUCTION

Magnesium (Mg) alloys are one of the most promising lightweight materials for future automotive, consumer electronics, and biomedical applications. However, the mechanisms controlling the corrosion and electrochemical responses of Mg alloys in aqueous solutions, and the relationship with alloy microstructures are not fully understood. This knowledge gap significantly limits the possibility of designing alloys and formulating strategies to control the corrosion responses for applications under different environments.

Localized corrosion, accompanied by rising streams of hydrogen bubbles, is the dominant form of corrosion occurs on Mg alloys in chloride ions ( $\text{Cl}^-$ ) containing aqueous solutions. This form of corrosion can lead to extraordinary fast corrosion rate and structural failure. The origin and mechanisms of localized corrosion are still unknown and under active investigations. Most if not all studies focusing on Mg corrosion limited to surface observations, translating into very little known about the initiation and propagation of localized corrosion, and the relationship with alloy chemistry and microstructure.

To address these knowledge gaps, this thesis focused on the corrosion behavior of pure Mg and selected Mg alloys to investigate the morphology and chemistry of corrosion features, and their relationship with hydrogen evolution response and alloy microstructures. The experimental work relied on multiscale microstructure characterization, using *in situ* optical microscopy (OM), scanning electron microscopy (SEM) with focused ion beam (FIB) milling, and transmission

electron microscopy (TEM). This work revealed the detailed chemistry, structure, and morphology of corrosion features formed on pure Mg and different Mg alloys for the first time. Different exposures to aqueous solutions testing the effect of chloride ions and anodic polarization were considered. In addition, interactions between alloy microstructure, in particular second phases and grain structure, and corrosion propagation were also discovered.

**Chapter 1** provides a review of our current understanding of corrosion behavior and mechanism of pure Mg and Mg alloys in aqueous solutions. In **Chapter 2**, the corrosion behavior was first studied on a Mg-Y-Nd-Zr alloy that does not exhibit localized corrosion, to understand the development of surface corrosion film and the general effect of second phase particles. **Chapter 3** focuses on anodic polarization controlled localized corrosion and associated hydrogen evolution response on the same Mg-Y-Nd-Zr alloy to understand the microstructural specificities of localized corrosion. **Chapter 4** expands the localized corrosion study to three Mg alloys with different chemistries and alloy microstructures under both free immersion and anodic polarization conditions. The similarity between the characteristics of corrosion features under different test conditions confirmed that localized corrosion on Mg alloys is controlled by a common mechanism irrespective of alloy chemistry or microstructure. Nonetheless, a strong dependence of localized corrosion propagation on the alloy grain structure and grain boundary chemistry was revealed. Finally, **Chapter 5** summarizes the findings by proposing a corrosion model for Mg alloys and provides suggestions for future investigations.

## **CHAPTER 1:**

### **Corrosion Behavior and Mechanism of Pure Mg and Mg Alloys: Literature Review**

#### **1.1 Mg Alloys: with Great Potentials Comes Great Problems**

Combining low density and high specific strength, Mg alloys are promising lightweight materials for aerospace, automobile, and consumer electronics applications [1-3]. The biocompatibility and biodegradability of Mg also make them suitable for body implants for medical treatments, which avoids subsequent removal surgeries [4, 5]. In addition, the high reactivity and unique electrochemical properties make them candidates as next-generation battery electrodes [6] and hydrogen generation materials [7].

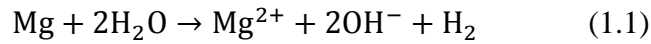
Even though the corrosion behavior and electrochemical response of pure Mg and Mg alloys have been studied for decades, significant ambiguities and unanswered questions regarding the corrosion mechanisms need further investigations [8]. A particular phenomenon that still puzzles the Mg corrosion community is the so-called “negative differential effect (NDE)” [9], which labels the increase in hydrogen evolution rate with increasing anodic polarization [8, 9], and the related localized corrosion behavior [10]. This phenomenon not only accelerates the corrosion rate of Mg alloys under anodic polarization [11], but also leads to possible structural failure by localized corrosion [12]. The roles of alloy microstructure on the corrosion behavior is also not fully understood. The lack of fundamental understandings about the corrosion mechanism and

alloy microstructure effects greatly limits the development of Mg alloys with better corrosion performance or proper electrochemical responses for applications under different environments.

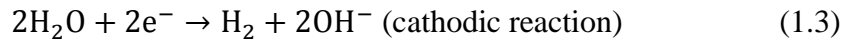
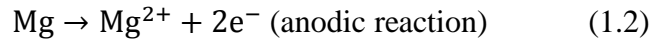
## 1.2 Corrosion Behavior and Mechanism of Mg

### 1.2.1 Corrosion Reactions and Features on Mg

Mg is one of the most active elements among all structural alloys, with a standard electrode potential of -2.37 V vs standard hydrogen electrode (SHE) [11, 13]. The overall dissolution reaction of Mg in aqueous solutions can be written as [11, 14]:



This reaction can be decomposed to the anodic and cathodic parts:



From the cathodic reaction (**reaction 1.3**), the dissolution of Mg in aqueous solution is accompanied by the production of hydroxide ion ( $\text{OH}^-$ ), which increases the pH value of the solution. According to the Pourbaix diagram of Mg [15] (**Fig. 1.1**), the increase in pH value moves the equilibrium condition of Mg into the magnesium hydroxide ( $\text{Mg}(\text{OH})_2$ ) passivation region, resulting in the formation of a  $\text{Mg}(\text{OH})_2$  layer on the Mg surface, which can be described by:



Therefore, the overall reaction can be rewritten as:



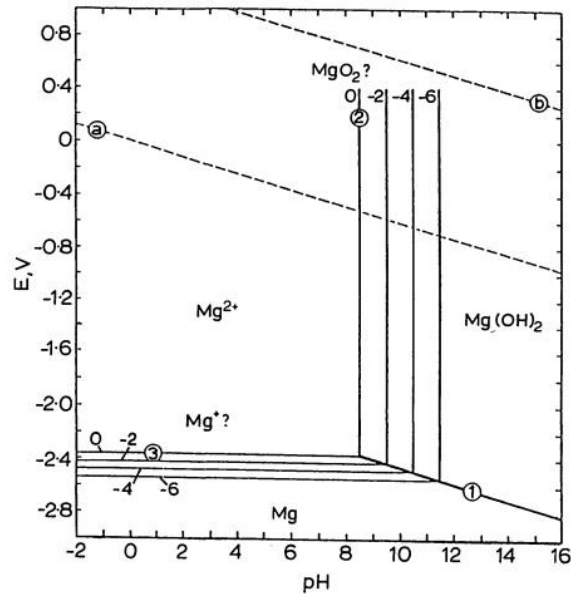


Figure 1.1 Pourbaix (E-pH) diagram of Mg (reproduced from Ref. [1] with permission).

The presence of a  $\text{Mg}(\text{OH})_2$  layer on Mg surface may explain why the measured corrosion potential of Mg alloys is always higher than  $-2.37$  V vs SHE, usually in the range of  $-1.25$  to  $-1.55$  V vs SHE (about  $-1.5$  to  $-1.8$  V vs saturated calomel electrode (SCE)) when immersed in aqueous solution [1, 13, 16].

Corrosion of Mg and Mg alloys can be more complicated than simple surface reaction and continuous film formation. The presence of second phases/precipitates in the alloys induces microgalvanic effects by coupling with the Mg matrix and acting as local cathodes/anodes [8, 17]. Also, Mg was shown to suffer from localized corrosion under corrosive environments, especially in the presence of chloride ions ( $\text{Cl}^-$ ) [18, 19]. The localized corrosion morphology on pure Mg depends strongly on the  $\text{Cl}^-$  concentration in the test solution. While circular form of localized corrosion was observed under high  $\text{Cl}^-$  concentration, filiform-like localized corrosion tracks were spotted under lower  $\text{Cl}^-$  concentration [18]. This localized form of corrosion on Mg is usually

accompanied by intense hydrogen evolution [20, 21]. While the detailed mechanism of localized corrosion and the associated hydrogen evolution is still under debate, it was shown to be related to the abnormal hydrogen evolution behavior of Mg under anodic polarization [8, 10], i.e. the NDE, which will be discussed in the following sections.

### ***1.2.2 The Mystery: Negative Difference Effect (NDE)***

Because of the low electrochemical potential, Mg alloys are almost always anodically polarized when connected to other alloys. During anodic polarization, a notoriously peculiar electrochemical phenomenon occurs on pure Mg and Mg alloys. It is known as the negative difference effect, or NDE, and was first observed by Beetz [22] back in 1866. **Fig. 1.2** presents an illustration of the NDE phenomenon [11]. On normal electrodes, the anodic and cathodic reaction rates are assumed to obey Tafel kinetics, as shown by the solid lines marked as  $I_a$  and  $I_c$  for the anodic and cathodic reactions, respectively. The reaction rates are equal to  $I_0$  at the open circuit potential ( $E_{oc}$ ), or corrosion potential ( $E_{corr}$ ), where no anodic/cathodic bias is applied on the electrode. When applying an external voltage to the system to change the potential to a more positive (anodic) value, the anodic reaction rate increases and the cathodic reaction rate decreases along the solid line. However, on Mg, the cathodic hydrogen evolution rate also increases with increasing potential, as shown by the dashed line marked  $I_H$ . The NDE is usually defined by the difference  $\Delta$ :

$$\Delta = I_0 - I_{H,m} \quad (1.6)$$

where  $I_0$  is the spontaneous hydrogen evolution rate at  $E_{corr}$  and  $I_{H,m}$  is the hydrogen evolution rate under a given anodic polarization. Normally, the  $\Delta$  value is expected to be positive since the



cathodic reaction rate would decrease with anodic polarization. But for Mg, the hydrogen evolution rate is faster than the spontaneous rate under anodic polarization, resulting in a negative  $\Delta$  value, i.e. NDE.

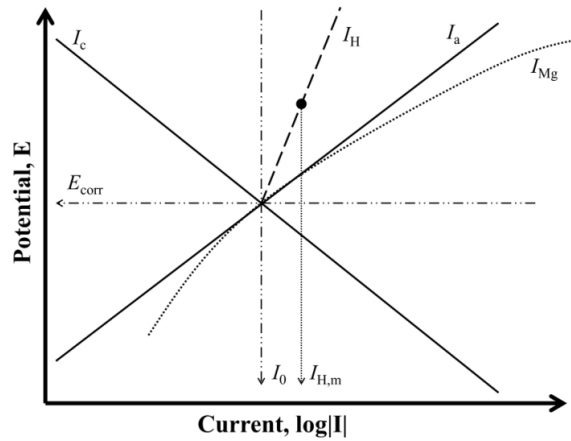


Figure 1.2 Schematic illustration of negative difference effect (NDE) on Mg (reproduced from Ref. [11] with permission).

The accelerating hydrogen evolution rate also implies that the anodic dissolution rate of Mg increases faster than the expected Tafel kinetics, as shown by the dotted line marked  $I_{Mg}$  in **Fig. 1.2**. Indeed, in a potentiodynamic polarization experiment, the measured current for a given polarization,  $I_{appl}$ , is related to the anodic and cathodic currents according to:

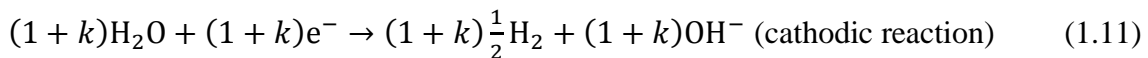
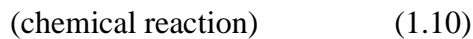
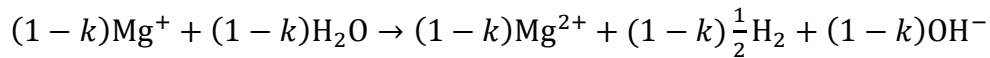
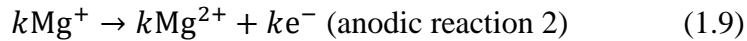
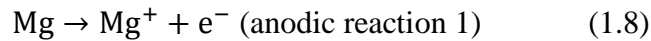
$$I_{appl} = I_{Mg} - I_H \quad (1.7)$$

Because of the unusual electrochemical behavior of Mg, the amount of Mg dissolved measured from the current,  $I_{appl}$ , using Faraday's law is smaller than the actual weight loss (corresponding to

$I_{Mg}$ ) by the amount  $I_H$ . Therefore, the commonly used Tafel method [23] results in inaccurate estimations of the corrosion rates of Mg.

### 1.2.3 Uni-Positive Magnesium ( $Mg^+$ ) Model

One of the initial models that attempted to explain the Mg NDE is the uni-positive  $Mg^+$  ion model, first proposed by Turrentine [24] in 1908. In 1954, Petty *et al.* [25] used indirect evidence to argue for the existence of  $Mg^+$  ion. After flowing a test solution through a pure Mg surface and down to a beaker filled with  $KMnO_4$  solution,  $MnO_2$  precipitates were found at the bottom of the beaker. It was proposed that  $MnO_2$  was formed through the reaction between  $Mg^+$  ions in the down flow solution and  $MnO_4^-$  ions in the beaker. This experiment was later widely cited as a proof of the existence of uni-positive  $Mg^+$  ion [1, 11, 17]. However, no direct experimental results have ever confirmed the existence of  $Mg^+$  ion in aqueous solution. The uni-positive  $Mg^+$  ion model was then used by Song and Atrens [9, 26, 27] to describe the abnormal hydrogen evolution response under anodic polarization during corrosion of Mg and Mg alloys. In their model, the anodic partial reaction of Mg dissolution was proposed to occur in two steps, involving uni-positive  $Mg^+$  ions as an intermediate oxidation state. The reaction sequence is as follows [28]:



Summation of **reactions 1.8-1.11** gives the overall **reaction 1.1**.

In this reaction sequence, **reaction 1.10** is a chemical reaction between the  $Mg^+$  ion and water molecules producing hydrogen gas that occurs away from the electrode surface and does not involve exchanging electrons with the electrode. This results in the acceleration of hydrogen evolution rate and excess  $Mg^{2+}$  under anodic polarization. A schematic illustration of Mg corrosion involving the  $Mg^+$  ion is shown in **Fig. 1.3** [11].

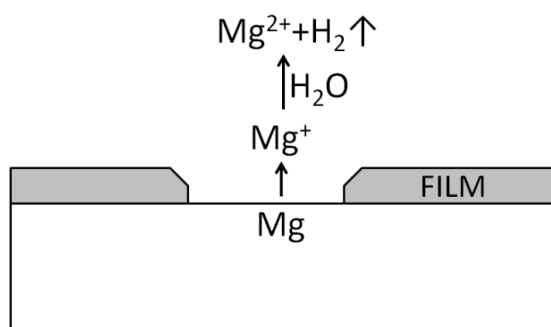


Figure 1.3 Schematic illustration of the corrosion mechanism of Mg involving uni-positive  $Mg^+$  ion (reproduced from Ref. [11] with permission). Production of univalent  $Mg^+$  ion (**reaction 1.8**) was proposed to occur in a film-free region on Mg surface.

The  $Mg^+$  model was widely accepted as the corrosion mechanism of Mg for years, until the utilization of combined experimental techniques [29-31] and improvement of *in-situ* electrochemical techniques [18, 19, 32, 33] questioned its validity. The experiments performed by Petty *et al.* [25] were replicated recently by Samaniego *et al.* [29] with added *in-situ* Raman spectroscopy. In their experiment,  $MnO_2$  precipitates were again observed in the beaker. However, Raman analysis of the reacting surface showed a peak corresponding to  $SO_2$ , strongly suggesting

that the reducing agent flowing down to the bottom beaker was  $\text{SO}_2$ , instead of  $\text{Mg}^+$  ions, thereby invalidating the evidence for the existence of  $\text{Mg}^+$  ion during Mg dissolution. More recently, another model was proposed based on additional experimental techniques, which will be reviewed in the next section.

#### ***1.2.4 Localized Corrosion and Enhanced Catalytic Activity Model***

When immersed in  $\text{Cl}^-$  containing aqueous solutions, a wide variety of Mg alloys were reported to exhibit localized corrosion [18, 19, 34-38], characterized by dark corrosion tracks forming on the alloy surface. Similar localized corrosion morphologies were also observed on Mg alloys under anodic polarization [39-41], which was accompanied by rising streams of hydrogen bubbles from the localized corrosion regions [18, 20, 21]. These observations implied that the excess hydrogen evolution might be related to the formation of localized corrosion regions. By *in situ* scanning vibrating electrode technique (SVET) experiments on pure Mg [18, 19, 42] and Mg alloys [43-45] in NaCl solutions, the dark localized corrosion tracks were found to be cathodic, while the propagating localized corrosion fronts were anodic.

In a separate work by Birbilis *et al.* [39], a set of potentiostatic cathodic measurements was performed on Mg after galvanostatic anodic polarizations. The cathodic response current was found to increase with the degree of prior anodic polarization. Importantly, the surface coverage of localized corrosion also increased with the degree of anodic polarization. Based on this observation and previous SVET results, Birbilis *et al.* [39] proposed that NDE originates from the increase of catalytic activity towards hydrogen evolution in the cathodic localized corrosion regions formed during anodic polarization, i.e. “enhanced catalytic activity”. A schematic illustration of the proposed model is shown in **Fig. 1.4** [19].

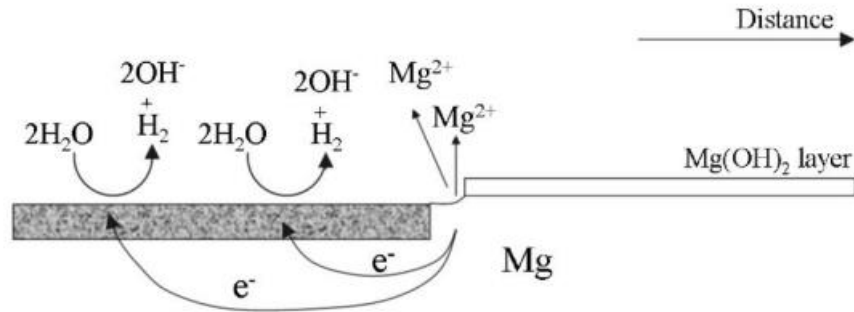


Figure 1.4 Schematic illustration of the localized corrosion mechanism of Mg with enhanced catalytic activity (reproduced from Ref. [19] with permission). A film-free region was proposed at the localized corrosion front where Mg dissolves into the solution.

Various experimental studies sought to find the origin of this so-called “catalytic activity”. Taheri *et al.* [46] examined a pure Mg immersed in 0.01M NaCl solution for 24 hours, followed by a potentiostatic anodic polarization at -1.0 V vs SCE for 0.5 hour. Tiny Fe-rich impurity particles were found to embed in the outer layer of the corrosion film, close to the film/electrolyte interface. They proposed that Fe-rich impurity particles were responsible for the increase in catalytic activity of localized corrosion regions on Mg. Hoche *et al.* [47] proposed that Fe impurity in Mg might dissolve into the solution and redeposit in the localized corrosion regions during immersion tests. By Rutherford backscattering spectrometry on a pure Mg anodically polarized at -1.6 V vs SCE for 24 hours, Cain *et al.* [48] showed that the interface between the corrosion film and Mg matrix could be another possible enrichment site for Fe impurities. Cross sectional TEM observations were performed on the localized corrosion regions on Mg-Al-Zn [49], Mg-Al-Mn [50], and Mg-Zn-Zr alloys [51] by Kish *et al.*. Second phase precipitates were found to incorporate in the localized corrosion products. Also, interfacial enrichment of alloying elements (Al in Mg-

Al-Mn, Zn in Mg-Al-Zn and Mg-Zn-Zr alloys) was also identified at the corrosion region/alloy interface. The second phase incorporation and elemental interfacial enrichment were then proposed to be another possible source for the enhanced catalytic activity. However, in a study by Fajardo *et al.* [40], an obvious NDE was still observed on an ultra-high purity Mg (99.9999%), indicating impurity enrichment or second phase incorporation might not be the only origin of enhanced catalytic activity.

The Mg(OH)<sub>2</sub> phase itself was proposed as another possible source of the enhanced catalytic activity. Salleh *et al.* [52] used scanning electrochemical microscopy (SECM) to study the electrochemical response difference between a pristine Mg surface and a Mg(OH)<sub>2</sub> covered Mg surface. A faster hydrogen evolution rate was observed on the latter during both free corrosion and cathodic polarization. However, the increase in hydrogen evolution rate during anodic polarization on pure Mg was reported to be several orders of magnitude higher than that observed by Salleh *et al.* [40], indicating the increase in hydrogen evolution rate on Mg(OH)<sub>2</sub> cannot solely contribute to the NDE. To date, origin of the proposed “enhanced catalytic activity” is still unknown.

A major limitation of the enhanced catalytic activity model is the assumption that hydrogen is generated at the cathodic regions, i.e. the cathodic localized corrosion tracks left on Mg surface. However, it was reported that rising streams of hydrogen bubbles were observed predominantly at the anodic localized corrosion fronts instead of the cathodic corrosion tracks [44, 45, 53, 54]. In a very recent series of experiments, NDE was observed on a pure Mg tested in a citric acid solution buffered at pH 3, while no dark localized corrosion track was observed on the sample surface [55]. This confirmed that the increase in hydrogen evolution rate under anodic polarization is primarily associated with the anodic reactions and the anodic dissolution regions [41, 55], and the cathodic

localized corrosion tracks play a relatively minor role. This concludes our current understanding of NDE, and the mechanisms responsible for the NDE have yet to be elucidated.

### **1.3 Effect of Alloy Chemistry and Microstructure on Corrosion of Mg Alloys**

#### ***1.3.1 Role of Alloying Elements***

The presence of alloying elements in Mg was proposed to change the passivity and stability of the surface corrosion film. On pure Mg, a three-layered corrosion film structure was revealed after immersion in distilled water for 48 hours, consisting of an inner cellular layer, a dense intermediate region, and a platelet-like outermost layer [56, 57]. The corrosion film formed on Al containing Mg alloys after immersed in water for 48 hours was shown to have a similar three-layered structure [58, 59]. However, the thickness of the inner cellular layer and the platelet-like outer layer both decreased significantly after the incorporation of Al into the film. This presence of Al was proposed to slow down the corrosion reactions by increasing the surface film passivity. Additionally, Danaie *et al.* [60, 61] observed a thin Al-rich layer at the corrosion film/matrix interface in a high Al content region on a sand cast Mg-Al-Mn alloy immersed in 1.6 wt% NaCl solution for 96 hours. This interfacial enrichment of Al was proposed to contribute to the observed better corrosion resistance for regions with higher Al content. A similar interfacial enrichment of Zn in Mg-Al-Zn [62, 63] and Mg-Zn-Zr [63] alloys was also reported and proposed to increase the passivity of corrosion film on Mg alloys. Rare earth elements and yttrium (Y) were also proposed to increase the surface film passivity by incorporation in the surface film during corrosion [37, 64-66]. However, no systematic high resolution microscopy characterization study has been performed to confirm this hypothesis.

The presence of alloying elements as solid solution also affects the chemistry and electrochemical response of Mg. **Fig. 1.5** [8, 66] shows a compilation of the effect of different alloying elements on the cathodic and anodic reactions of Mg. Elements that are nobler than Mg were usually observed to increase the cathodic reaction rate of Mg. This enhanced cathodic reaction was attributed to the incongruent dissolution of Mg that results in the surface enrichment of alloying elements and preferential hydrogen evolution on the relatively nobler surface. The preferential cathodic reaction on the surface also contributes to the reduction of the anodic reaction rate. Some other elements were reported to enhance the anodic reaction. Ca was proposed to increase the anodic reaction rate because of the higher reactivity (-2.87 V vs SCE) compared to Mg [67]. Sn and Pb were proposed to disrupt the formation of the surface corrosion film formation and enhance anodic dissolution because of the low melting temperature [66]. However, further investigations are needed to confirm these theories. Last but not the least, recent investigations reported that certain elements, such as Arsenic (As) [68, 69], cadmium (Cd) [70], and germanium (Ge) [71], can retard the cathodic hydrogen evolution reaction by blocking the recombination of hydrogen atoms and greatly improve the corrosion resistance of Mg alloys.

Very recently, computational modeling was utilized to calculate the kinetics of reduction of water and hydrogen evolution on Mg surface and the effect of different alloying elements [72-74], which might give further insights to the effect of alloying addition.



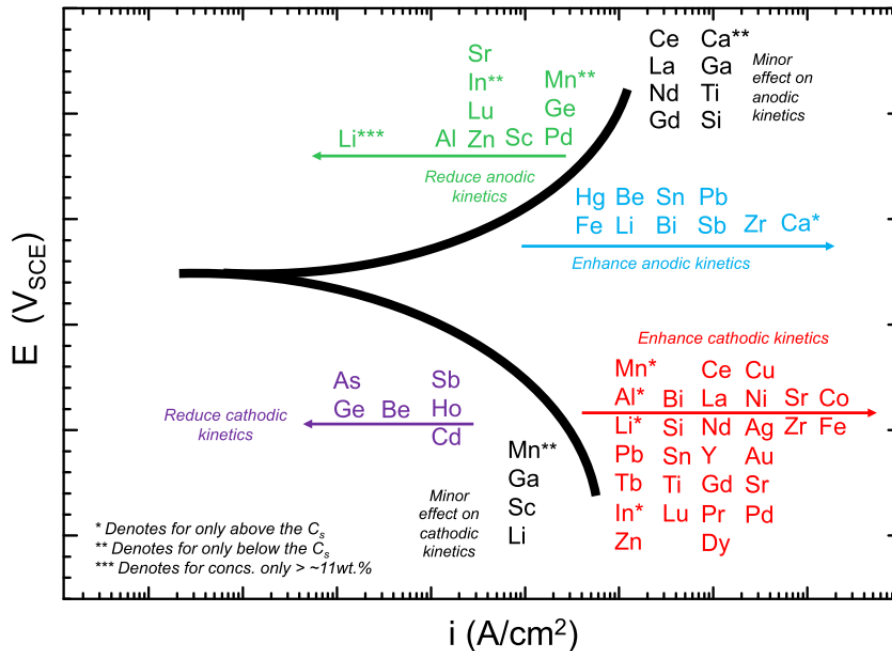


Figure 1.5 A compilation of alloying elements effect on the cathodic and anodic reaction rates of Mg (reproduced from Ref. [8] with permission).

### 1.3.2 Roles of Second Phases

Experimental evidence suggests that there is a “tolerance limit” in the elemental concentration, above which Mg corrosion rate accelerates dramatically (**Fig. 1.6**) [1, 8, 75]. Some alloying elements, such as Fe, Ni, Co, and Cu, have a notoriously low tolerance limit (usually less than 1000 ppm in pure Mg) and cause dramatic acceleration of corrosion rate upon exceeding the limit. Other alloying elements, such as Al, Zn, and Sn, have relatively higher tolerance limits, and are less detrimental to the corrosion resistance of Mg. Hanawalt *et al.* [75] suggested that the tolerance limit of a given alloying element is linked to its solubility in Mg. If an alloying element is added in excess of its solubility, second phases form and result in microgalvanic acceleration of

the corrosion rate, which depends on the volume fraction of second phases and the potential difference between the second phases and the Mg matrix.

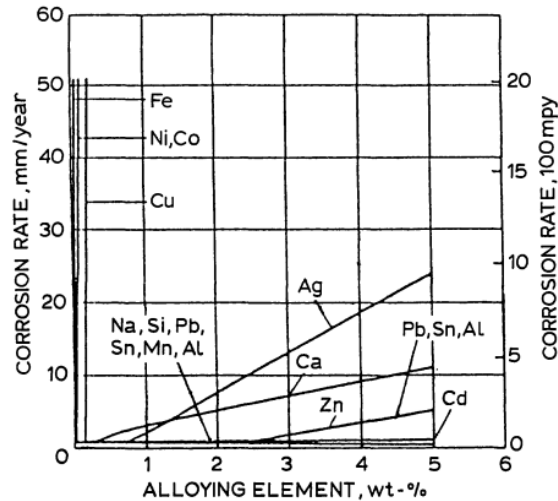


Figure 1.6 Corrosion rates as a function of alloying element concentrations in Mg. The corrosion rate dramatically increases upon exceeding the tolerance limit (reproduced from Ref. [1] with permission).

However, synergies between elements can complicate this simple description. For instance, addition of Mn is known to increase the tolerance limit of Ni and Fe in Mg alloys [75], by forming less detrimental second phases that sequester the harmful alloying elements [76]. This reduces the potential difference between the second phases and Mg matrix, and reduces the microgalvanic effect. Recently, Zirconium (Zr) was found to have a similar sequestration effect as Mn when added to Mg alloys [77]. This concept was utilized to produce ultra-high purity Mg, when the high density  $FeZr_x$  particles settled to the bottom of the melt and can be separated. Conversely, the addition of Si to Mg alloys was shown to promote the formation of Fe-Si impurity particles that

accelerate corrosion rate even for Fe content well below the tolerance limit [78]. In summary, it is not surprising that the tolerance limit of Mg alloys was found to depend on the overall chemistry, processing, and thermal history of the alloys [8, 11].

From a mechanistic view, the effects of second phases can be understood from their electrochemical potential as summarized in **Fig. 1.7** [79]. Because of the high reactivity of Mg matrix, the potential of most second phases present in Mg alloys is higher than that of Mg, promoting anodic reaction in the Mg matrix. Increasing the amount of alloying elements increases the volume fraction of high potential second phases and leads to a monotonic increase in corrosion rate, as reported in Mg-cerium (Ce) [80], Mg-neodymium (Nd) [80], and Mg-Y [37] alloys. Alternatively, some second phases, such as  $Mg_2Ca$  shown in **Fig. 1.7**, have a lower potential than Mg and play an inverse role that promotes cathodic reaction in Mg matrix. This local anode effect was reported for Mg-gadolinium (Gd)-Y based alloys where second phases with a lower potential than the Mg matrix, served as local anodes, and preferentially dissolved during the corrosion tests [81, 82].

The presence of second phases was also shown to play an important role in localized corrosion on Mg alloys. Initiation of localized corrosion under free immersion was found close to second phases in Mg-Li [35] and Mg-Zn-Y-Zr [36] alloys. This was again explained with the microgalvanic effect of the second phases that promoted anodic dissolution and initiation of localized corrosion in the Mg matrix.

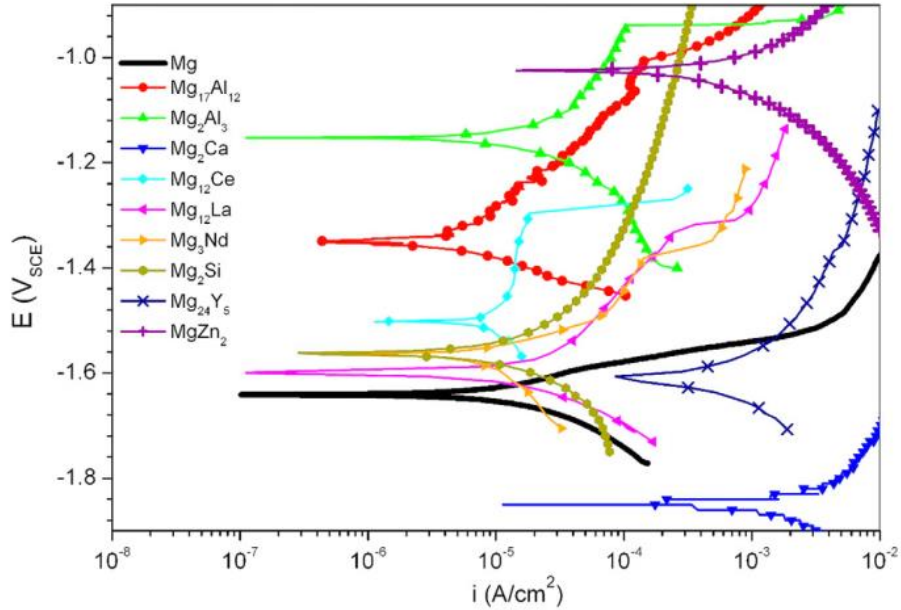


Figure 1.7 Collection of polarization curves of common second phases in Mg alloys (reproduced from Ref. [8] with permission).

In addition to the microgalvanic effect, some second phases can be used as a corrosion barrier to stop the corrosion reaction. For example, it was reported that in cast AZ91 (Mg-9 wt% Al-1 wt% Zn) alloys, the  $Mg_{17}Al_{12}$  phase can serve as an effective corrosion barrier because of the continuous network structure along the grain boundaries [83]. The corrosion reaction in AZ91 alloys occurred primarily in the Mg matrix initially, and eventually ceased once most of the Mg matrix is dissolved and a continuous  $Mg_{17}Al_{12}$  phase network was exposed, as shown in **Fig. 1.8**. Furthermore, it was found that the corrosion rate of a die-cast AZ91 alloy is much slower than the sand-cast AZ91 because of the finer and more continuous  $Mg_{17}Al_{12}$  phase resulting from the faster cooling rate during casting. In conclusion, besides the electrochemical potential, the volume fraction, distribution and morphology of second phases are also important considerations when designing corrosion resistant Mg alloys.

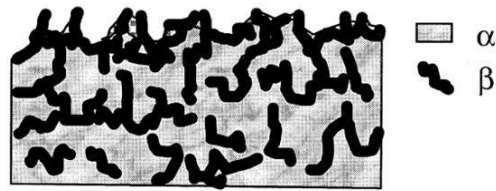


Figure 1.8 Schematic illustration of corrosion barrier effect for Mg<sub>17</sub>Al<sub>12</sub> phase in die-cast AZ91 alloy (reproduced from Ref. [11] with permission).

### 1.3.3 Role of Grain Structure

Beside second phases, grain structure is another factor that affects the corrosion behavior of Mg alloys. Slower corrosion rate was generally observed for (0001) oriented grains. Liu *et al.* [84] found that the dissolution depth of pure Mg on grains near (0001) basal orientation was shallower than the grains away from (0001) direction tested in 0.1M HCl solution. This observation was later confirmed by additional studies [85, 86]. Similarly, Song *et al.* [87] found that the rolling surface of a polycrystalline AZ31 (Mg-3 wt%Al-1 wt%Zn) Mg alloys, which mainly consisted of (0001) grains, had a slower corrosion rate than the (10 $\bar{1}$ 0) and (11 $\bar{2}$ 0) grains containing cross-section surface. This was attributed to the relatively higher atomic packing density and lower surface energy on (0001) grains that slowed down the Mg dissolution reaction [87, 88]. It was also noted that the galvanic coupling effect between grains with different crystal orientation might also play an important role when considering the grain orientation effect [89].

Even though a lower corrosion rate was generally observed on the (0001) grains, it was also reported that the (0001) grains are more susceptible to localized corrosion than other orientations [90, 91]. Song *et al.* [87] indeed found that the localized corrosion coverage on the

rolling surface (mainly (0001) grains) of a rolled AZ31 was higher than the cross-section surface (mainly (10 $\bar{1}$ 0) and (11 $\bar{2}$ 0) grains). The reason behind this susceptibility to localized corrosion for (0001) grains is still unclear. Recently, it was reported that the surface corrosion film thickness on (0001) grains, as measured by Raman spectroscopy and electrochemical impedance spectroscopy (EIS), was thinner than grains with other orientations [92]. This could result in a higher tendency to film breakdown and initiation of localized corrosion. Detailed microscopic study is needed to elucidate the real effect of grain orientation on the surface corrosion film.

Some evidence exists for a grain size effect on Mg alloys corrosion though it seems that it is usually shadowed by the impact of second phases [93]. Birbilis *et al.* [94] used equal channel angular pressing to produce pure Mg with various grain size from 2.6 to 125  $\mu\text{m}$ , and found the corrosion rate scaled linearly with the logarithm of grain size. Argade *et al.* [95] also reported a correlation between the corrosion rate and grain size on wrought Mg-Y-rare earth alloy, but with a power law relationship. This discrepancy in grain size dependence was attributed to the difference in alloy chemistry. Lu *et al.* [96] found that when the volume fraction of second phase was less 0.8% in a Mg-Zn-Ca alloy tested in simulated body fluid, the grain size became the controlling factor of corrosion rates. In general, it is agreed that Mg alloy with small grain corroded slower than its large grain counterparts. This was proposed to relate to a more homogeneous corrosion and better corrosion film stability because of higher number density of grain boundaries [95]. However, no microscopic support or mechanism for this theory was provided, which warrants further investigation.

## 1.4 Summary

Even though coatings and other protection methods enabled the application of Mg alloys in different fields, the lack of fundamental understanding of the corrosion mechanisms of bare Mg strongly limit the possibility to improve the corrosion resistance of Mg and decrease of the cost of post-treatments. Utilization of modern electrochemical techniques and delicate design of correlative experiments have provided great insights to the corrosion behavior, especially the localized corrosion on pure Mg and Mg alloys. However, detailed characterization of the chemistry, structure, and morphology of the corrosion features, and its relationship with underlying alloy microstructure is still missing.

Of note, in the models presented above, such as **Fig. 1.3** and **1.4**, a film-free region was invoked at the propagating propagation localized corrosion fronts to represent a surface corrosion film breakdown and direct exposure of Mg to the test solution. However, no experimental evidence exists of such film-free region or film breakdown. This is because most of the studies strictly relied on surface techniques or lacked a comprehensive view of the corrosion encompassing not only the macroscopic manifestations of corrosion through hydrogen evolution but also the sub-surface phenomena and alloy microstructure. The aim of this work is to provide the missing link between the corrosion response and localized corrosion microstructure, and further elucidate the roles of alloy microstructure using a multiscale microstructure characterization approach.

## CHAPTER 2:

### Corrosion Microstructure and Behavior on a Heat-Treated Mg-Y-Nd-Zr Alloy<sup>1</sup>

#### 2.1 Motivation

Before investigating the localized corrosion behavior and the NDE on Mg alloys, it is crucial to understand the microstructure of general corrosion features and identify other sources of hydrogen evolution. The heat-treated WE series Mg alloy is an ideal starting point because it does not suffer from localized corrosion during free corrosion. Therefore, the microstructure of surface corrosion film and the roles of second phase particles were first studied on a commercial WE43 Mg alloy.

Among all Mg alloys, the WE series Mg alloys, containing Y and rare earth elements, combine high specific strength, creep resistance, and good castability [3, 97]. Strengthening of these alloys is achieved by the formation of a dense distribution of fine scale precipitates that are formed by heat treatments, and remain stable up to 5000 hours in the 200 to 250 °C temperature range [3]. These unique precipitate structure and distributions make these alloys suitable for high temperature weight reduction applications.

---

<sup>1</sup> The results presented in this chapter were published in:

P.W. Chu, E.A. Marquis, Linking the Microstructure of a Heat-Treated WE43 Mg Alloy with Its Corrosion Behavior, *Corros. Sci.*, 101 (2015) 94-104 doi.org/10.1016/j.corsci.2015.09.005.



## 2.2 Materials and Methods

### 2.2.1 Materials and Sample Preparation

A bar of wrought Mg-Y-Nd-Zr (WE43) alloy was provided by Magnesium Elektron Ltd. The composition of the alloy measured by induced couple plasma-mass spectrometry (ICP-MS) is shown in **Table 2.1**. The bar was cut into cubes with a dimension of  $1 \times 1 \times 1 \text{ cm}^3$  before heat treatments. The cubes were sealed into a quartz tube filled with sulfur hexafluoride ( $\text{SF}_6$ ) gas to prevent oxidation. The sealed samples were solution-treated at  $525^\circ\text{C}$  for 8 hours, followed by water quenching. These samples are designated as “solution-treated WE43”. Half of the solution-treated samples were then placed into an oil bath at  $250^\circ\text{C}$  for 16 hours to reach the peak hardness as reported in [98, 99]. These aged samples are designated as “peak-aged WE43”.

The cubes were then mounted in Buehler EpoThin epoxy with an exposed surface area of  $1 \text{ cm}^2$ . Before all corrosion tests, the samples were ground and polished down to  $0.25 \mu\text{m}$  in alcohol-based diamond suspensions. The samples were cleaned with anhydrous alcohol and dried in flowing dry air.

Table 2.1 Chemical composition and impurity level of WE43 alloy as measured by ICP-MS.

	<b>Y</b>	<b>Nd</b>	<b>Zr</b>	<b>Gd</b>	<b>Zn</b>	<b>Mn*</b>	<b>Cu*</b>	<b>Fe*</b>	<b>Ni*</b>
<b>wt%</b>	3.74	2.10	0.45	0.52	0.016	<0.03	<0.02	<0.005	<0.002
<b>at%</b>	1.08	0.37	0.13	0.085	0.006	<0.014	<0.008	<0.002	<0.001

\* Impurity level from industry standard AMS4371.

### ***2.2.2 Corrosion Tests and In-Situ Observation***

All corrosion tests were performed in a solution of 3.5 wt% sodium chloride (NaCl) saturated with magnesium hydroxide ( $\text{Mg}(\text{OH})_2$ ) at a pH of 10.5. An AmScope stereo microscope with a CCD camera was used to record the corrosion process under open circuit without agitation. After immersion, the corroded samples were removed from the solution, cleaned with deionized water and dried in flowing dry air.

The open circuit potential (OCP) and cathodic polarization curves of the heat-treated samples were measured in a three-electrode configuration, with the WE43 samples as working electrode, a saturated calomel electrode (SCE) as reference electrode and a high-density graphite bar as counter electrode. An Ivium Vertex potentiostat/galvanostat was used for all tests. The cathodic polarization curve was performed from +50 mV vs OCP to -500 mV vs OCP at a scan rate of 1 mV/s in the same test solution after 24 hours of immersion. The corrosion current density was measured by linear Tafel extrapolation and the corrosion rate was then estimated by assuming the number of valence electron of Mg is 2 [23, 100].

Corrosion rates were evaluated by measuring the hydrogen evolution reaction rate. The setup was adapted from Ref. [101]. An upside-down centrifuge tube filled with the test solution was put over the sample to collect the evolved hydrogen gas. The corrosion rate was estimated from the hydrogen evolution rate by assuming an ideal gas behavior for the hydrogen gas [28].

### **2.2.3 Microstructure Characterization**

A FEI Helios Nanolab 650 scanning electron microscope/focused ion beam (SEM/FIB) system equipped with an EDAX X-ray energy dispersive spectroscopy (EDS) detector was used for the microstructure characterization before and after the corrosion tests. A standard site-specific liftout process was used for preparing cross section transmission electron microscopy (TEM) samples [102], with the surface of the sample protected by depositing a layer of platinum (Pt) and a final cleaning step with a 2 kV Ga ions. A Leica cryogenic stage with a temperature of 150 K was used during the thinning process of the TEM samples, in order to minimize possible beam damage during ion milling (see **Appendix I**).

A JEOL 3011 high-resolution TEM and a JEOL 2010F analytical TEM were used to perform cross sectional microstructure characterization. A Gatan 636 liquid nitrogen cooling holder with a temperature of 150 K was used during TEM observations in order to minimize degradation of the corrosion film during imaging (see **Appendix I**). X-ray EDS mapping was performed using a Hitachi HD-2300A scanning transmission electron microscopy (STEM) equipped with an Oxford EDS detector and the EDS spectrum images were analyzed using the Oxford INCA software.

The O/Mg ratio obtained from EDS analysis is argued not reliable for inferring the nature of corrosion film [49]. However, STEM/EDS composition quantification performed on TEM liftout samples prepared from standard MgO and Mg(OH)<sub>2</sub> powders successfully distinguished Mg(OH)<sub>2</sub> and MgO with the O/Mg ratio (see **Appendix II**). Therefore, a similar method was used for all EDS quantification in this thesis.

## 2.3 Results

### 2.3.1 Microstructure of the Heat-Treated WE43 Alloy before Corrosion Testing

The microstructure of WE43 in its two heat-treated conditions was analyzed before the corrosion tests. The grain size of the WE43 alloy is in the range of 50 to 100  $\mu\text{m}$ . Micron-sized particles were observed on the polished surface of the solution-treated WE43 sample (**Fig. 2.1(a)**). Two different morphologies of particles were observed, one with a rectangular shape and the other with an irregular shape. EDS analysis revealed that the rectangular shape particles are Y-rich and likely the  $\text{Mg}_{24}\text{Y}_5$  intermetallic [103]; the irregular shape particles contain Zr and impurity elements such as Fe, Ni, Cr or Mn. As mentioned in **Section 1.3.2**, Zr is effective in getting Fe from the Mg melt by forming intermetallic second phases [77]. The observed Y-rich and Zr-rich particles are not dissolved by the solution-treatment due to their high melting temperatures.

The Vickers microhardness of the alloy increases from  $68 \pm 3.3$  HV to  $82 \pm 2.5$  HV after aging-treatment, owing to the formation of the fine scale precipitates. A back-scattered electron (BSE) SEM image (**Fig. 2.1(c)**) shows the finely dispersed precipitates formed throughout the grains, as well as along grain boundaries with a zone depleted of precipitates along them. These precipitates are likely to be the  $\beta_1$  and  $\beta$  phases that are both Nd and Y rich [104]. We note that the large Y-rich and Zr-rich particles are also present after the aging-treatment (**Fig. 2.1(b)**).

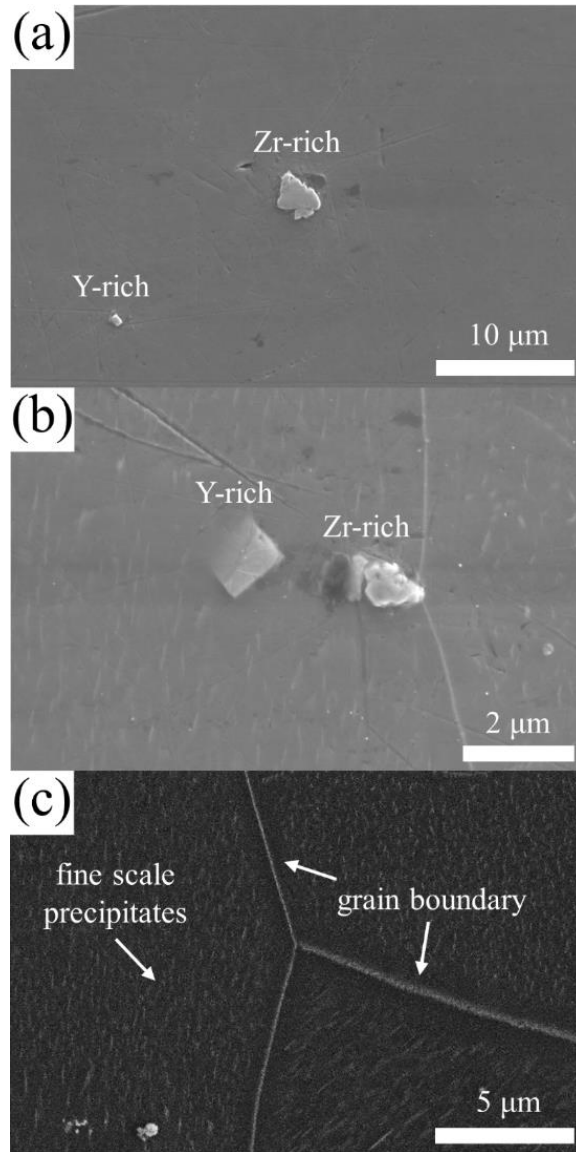


Figure 2.1 Secondary electron (SE) SEM images of as-polished surfaces from the (a) solution-treated and (b) peak-aged WE43 showing Y-rich and Zr-rich particles. (c) Back-scattered electron (BSE) SEM image of peak-aged WE43 showing the fine scale  $\beta_1$  and  $\beta$  precipitates throughout the grains and along the grain boundaries.

### 2.3.2 Corrosion Rate Measurements

The open circuit potential was measured for the first 24 hours of immersion in the 3.5 wt% NaCl solution saturated with  $\text{Mg}(\text{OH})_2$ . For both samples, the OCP increases drastically from about -1.92 V vs SCE up to about -1.78 to -1.80 V vs SCE in the first 10 to 20 minutes upon immersion (**Fig. 2.2(a)**). The potential then gradually drops to around -1.82 to -1.84 V vs SCE for the remaining of the measurement. The fast increase in the OCP in the first 10 to 20 minutes suggests the passivation of the surface and formation of a surface film. The slightly higher potential for the peak-aged sample suggests better film stability during passivation.

The cathodic polarization curves were obtained after 24 hours of immersion to estimate the corrosion rate (**Fig. 2.2(b)**). The corrosion potentials, cathodic Tafel slopes, corrosion current densities measured by linear Tafel extrapolation, and the estimated corrosion rates are shown in **Table 2.2**. The corrosion rate of the solution-treated WE43 is faster compared to that of the peak-aged WE43. However, evaluation of the corrosion rates from polarization curves was unreliable for Mg alloys owing to the complexity of the corrosion reactions (**Sections 1.2.2**) [105] and the results usually disagree with that from hydrogen evolution rate and weight loss [23, 100, 105]. Therefore, the hydrogen gas evolved from the corroding WE43 alloy surface was collected to assess the corrosion rates as a function of immersion time as shown in **Fig. 2.2(c)**. The solution-treated WE43 sample again showed a higher corrosion rate compared to that of peak-aged WE43 within an immersion timespan of 180 hours. The hydrogen evolution rate increases slightly with immersion time, possibly due to an increase in the effective surface area. The resulting corrosion rates for each alloy condition averaged from seven separate immersion tests are shown in **Fig. 2.2(d)**.

Table 2.2 Corrosion current densities and corrosion rates measured by linear Tafel extrapolation.

	Current Density ( $\mu\text{A}/\text{cm}^2$ )	Corrosion Rate (mm/yr)
<b>Solution-Treated WE43</b>	84.69	1.94
<b>Peak-Aged WE43</b>	69.94	1.60

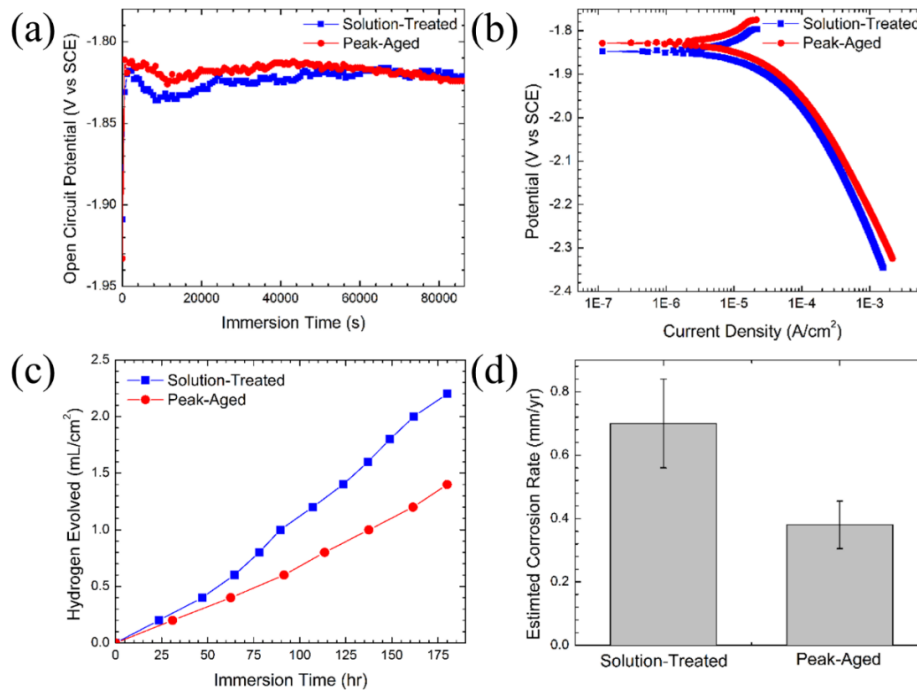


Figure 2.2 (a) The open circuit potential evolution in 3.5 wt% NaCl solution saturated with Mg(OH)<sub>2</sub> (T=21°C). (b) Cathodic polarization curves in the test solution after 24 hours of immersion. (c) Representative hydrogen evolution curves and (d) the estimated average corrosion rates from seven measurements (the error bars are the standard deviations).

### **2.3.3 Characterization of the Corrosion Products**

For both solution-treated and peak-aged WE43, uniform corrosion was observed with no localized corrosion features even after 100 hours of immersion (**Fig. 2.3**). Hydrogen bubbles were observed to form on both solution-treated and peak-aged WE43 surfaces. These hydrogen bubbles grew slowly with time and escaped from the sample surface once the bubbles had reached a critical size or some agitation was introduced in the solution. New hydrogen bubbles reformed at the very same locations. White dots were found at the locations where the hydrogen bubbles formed.

The corroded samples were removed from the test solution after various immersion times and transferred to a SEM to investigate the instantaneous corrosion morphology in more details. **Fig. 2.4** shows the observed corrosion morphology for both heat-treated samples after 1 hour and 6 hours of immersion. For both samples, the white dots, where the hydrogen bubbles initiated, are regions where corrosion products accumulated locally. These corrosion products protrude from the surface with a hemispherical shape or “domes” (**Fig. 2.5**) with sizes ranging from a few  $\mu\text{m}$  up to 100  $\mu\text{m}$  in diameter.

Away from the dome regions, a corrosion film was observed on the surface of both samples after 1 hour immersion (**Fig. 2.4(a) and (b)**). The film presented cracks, presumably from a dehydration reaction occurring during the transfer process to the SEM vacuum chamber. The underlying grain structure could still be discerned on the peak-aged WE43, suggesting that the corrosion film might still be thin in these areas.

After 6 hours of immersion, while a relatively uniform corrosion films was still observed on the surface of peak-aged WE43 (**Fig. 2.4(d)**), different morphologies on solution-treated WE43 were observed (**Fig. 2.4(c)**), suggesting the presence of two different regions: a thicker corrosion film with wide dehydration cracks and a thinner corrosion film with a surface appearance



comparable to that found on peak-aged WE43. The difference in thickness for the two regions of the corrosion film was confirmed by later cross sectional TEM observations.

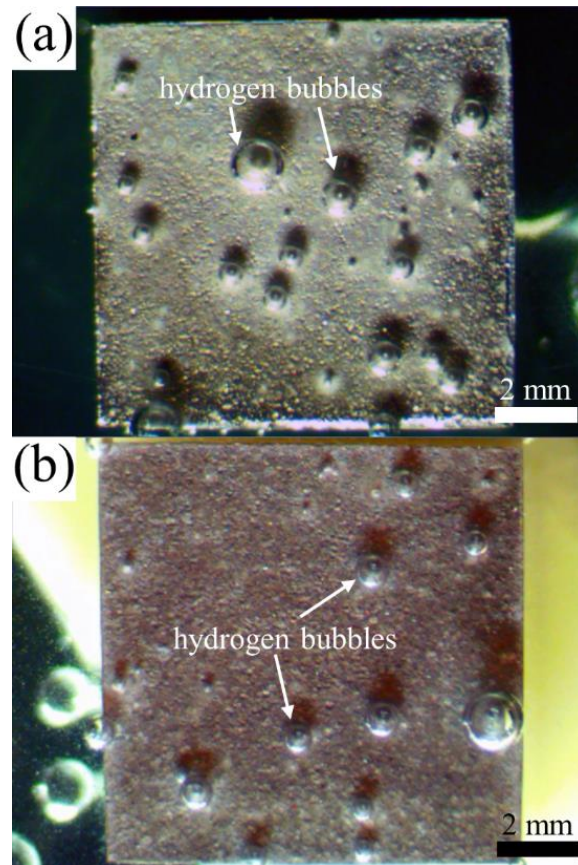


Figure 2.3 *in situ* observation of the corrosion morphology on (a) solution-treated and (b) peak-aged WE43 after 100 hours of immersion showing a uniform corrosion morphology and hydrogen bubbles.

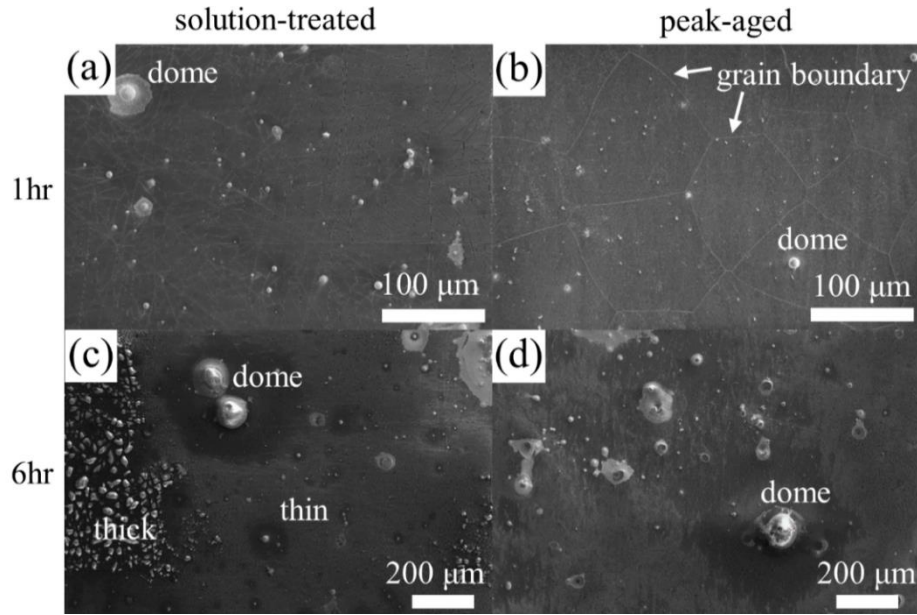


Figure 2.4 SEM surface images of the corrosion morphologies after 1 hour and 6 hours of immersions for solution-treated and peak-aged WE43 alloys. The labels “thin” and “thick” in (c) indicate regions with thin and thick surface films, respectively.

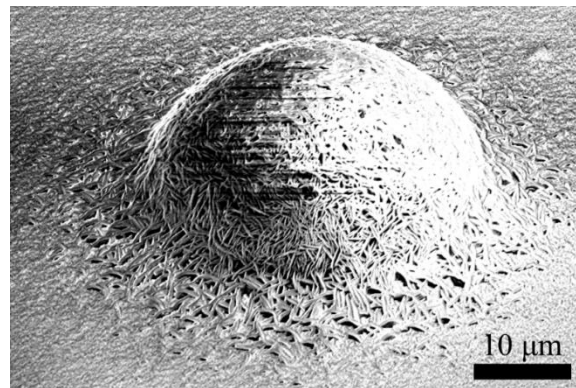


Figure 2.5 SEM image of a protruding dome formed on peak-aged WE43 after 24 hours of immersion. (Stage tilt = 52°)

In order to understand the formation mechanism of the domes, cross sectional TEM/STEM observations were performed on domes of different sizes. **Fig. 2.6(a)** shows a representative cross sectional STEM view of a dome formed on solution-treated WE43 after 1 hour immersion. Second phase particles were found at the alloy surface and underneath all the investigated domes. EDS analysis (**Fig. 2.6(b)**) confirmed that the analyzed particle contained Zr, Mg, Ni and Mn. All investigated domes were found to form on top of Zr-rich particles with impurity elements. No dome was found on top of Y-rich particles containing no Zr.

The domes have a porous structure, with increasing porosity from inner to the outer portions. The electron diffraction pattern for the inner portion coincide with  $\text{Mg}(\text{OH})_2$ , while the diffraction pattern changes gradually to MgO towards the outer portion of the dome (**Fig. 2.6(d)-(f)**). This gradual change of diffraction patterns indicate that the dehydration process occurs on the outer portion of the dome, while the inner parts are protected. EDS analysis (**Fig. 2.6(c)**) showed that the dome is mainly composed of Mg and O, with a trace amount of Cl. No alloying elements were identified in the EDS spectrum, suggesting that the domes are formed by precipitation of  $\text{Mg}(\text{OH})_2$  from the test solution. The chemical compositions of the particles and the dome are shown in **Table 2.3**.

The presence of a dome can affect the corrosion behavior of the surrounding surfaces, as illustrated by a 150  $\mu\text{m}$  wide SEM/FIB cross section cut across a dome region and shown **Fig. 2.7**, which shows the differences in the depth of the corrosion layer around the dome and away. The corrosion layer appears to be formed by deposition around the dome while it is penetrating into the alloy away from the dome. This suggests that the dome region is locally protective and this local effect can be explained by a microgalvanic effect from the Zr-rich particles, which will be discussed in **Section 2.4**.

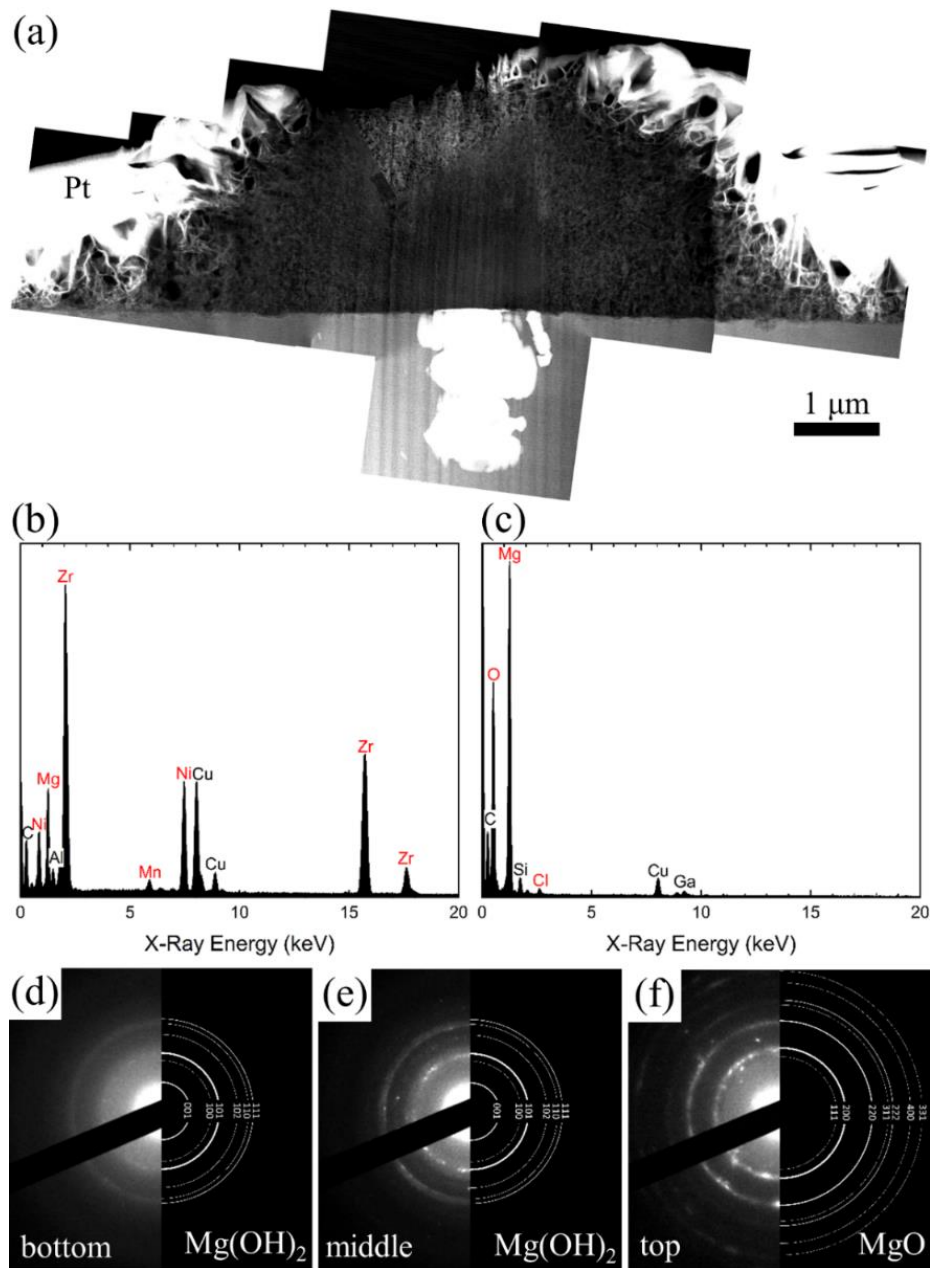


Figure 2.6 (a) Cross sectional STEM images of a protruding dome and the underlying particles of solution-treated WE43 after 1 hour immersion. EDS spectra for (b) the underlying particles and (c) the dome (quantitative analysis of the EDS spectra are shown in **Table 2.3**), and (d)-(f) electron diffraction pattern evolution of the dome from inner to outer portions. (Elements in the spectra

which are not included in the quantification are from the TEM sample holder (Cu and Al), contamination during sample preparation (Si), carbon deposition during imaging (C) and Ga damage during ion milling (Ga.)

Table 2.3 Chemical composition analysis by EDS for the dome and the underlying particles.

(The EDS spectra are shown in **Fig. 2.6(b)** and (c)).

at%	O	Mg	Cl	Y	Nd	Zr	Gd	Mn	Ni
<b>Particles</b>	-	21.4	-	-	-	57.5	-	1.6	19.5
<b>Dome</b>	58.5	40.9	0.6	-	-	-	-	-	-

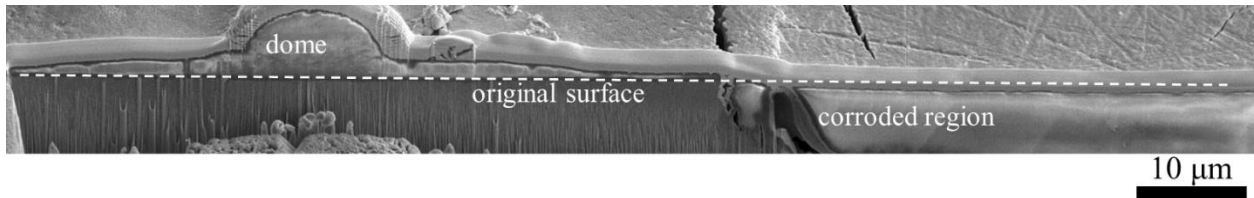


Figure 2.7 Cross sectional SEM/FIB images illustrating the local protecting effect of the dome on peak-aged WE43 after 5 days of immersion.

Since the dome regions are protected by the accumulation of corrosion products, the dominant corrosion process takes place away from the domes. Therefore, it is important to understand the microstructure of the corrosion film, its relationship with the underlying microstructure, and the resulting corrosion behavior. Cross sectional TEM/STEM investigations were performed on the corrosion film formed after immersions for 1 hour and 6 hours (**Fig. 2.8**).

The corrosion films formed on the solution-treated and peak-aged WE43 samples both showed a similar bi-layered porous structure, with the outer layer being more porous than the inner layer.

Representative electron diffractions and EDS analyses for the corrosion films are shown in **Fig. 2.9**. The electron diffraction pattern of the outer layer (**Fig. 2.9(a)**) only shows a diffuse diffraction halo, consistent with an amorphous structure; while the inner layer (**Fig. 2.9(b)**) shows a diffraction pattern which coincides with that of the MgO structure. From EDS analyses, the corrosion film is mainly composed of Mg and O, with trace amounts of alloying elements and Cl. The inclusion of alloying elements in the corrosion film indicates that the film is formed by corrosion reactions between the solution and the alloy. The outer layer of the corrosion film shows an O/Mg ratio around 2, consistent with Mg(OH)<sub>2</sub>; and the inner layer shows an O/Mg ratio close to 1, implying an MgO structure. The microstructure of the corrosion film can be summarized as an outer porous amorphous Mg(OH)<sub>2</sub> layer on top of an inner MgO layer.

The precipitates formed during aging of the alloy are incorporated into the corrosion film on peak-aged WE43 (**Fig. 2.8(b) and (d)**). This phenomenon is more obvious when EDS mapping is performed (**Fig. 2.10**), as the precipitates can be clearly discerned from the Nd map. This again confirms the inward growth of corrosion film, which was observed in **Fig. 2.7** away from the domes. Therefore, a region with thicker corrosion film correlates with a deeper corrosion depth, i.e. a faster corrosion rate. The film/alloy interface is rougher for the peak-aged WE43 than for the solution-treated. This is attributed to the presence of precipitates and their interactions with the inward propagation of the corrosion front.

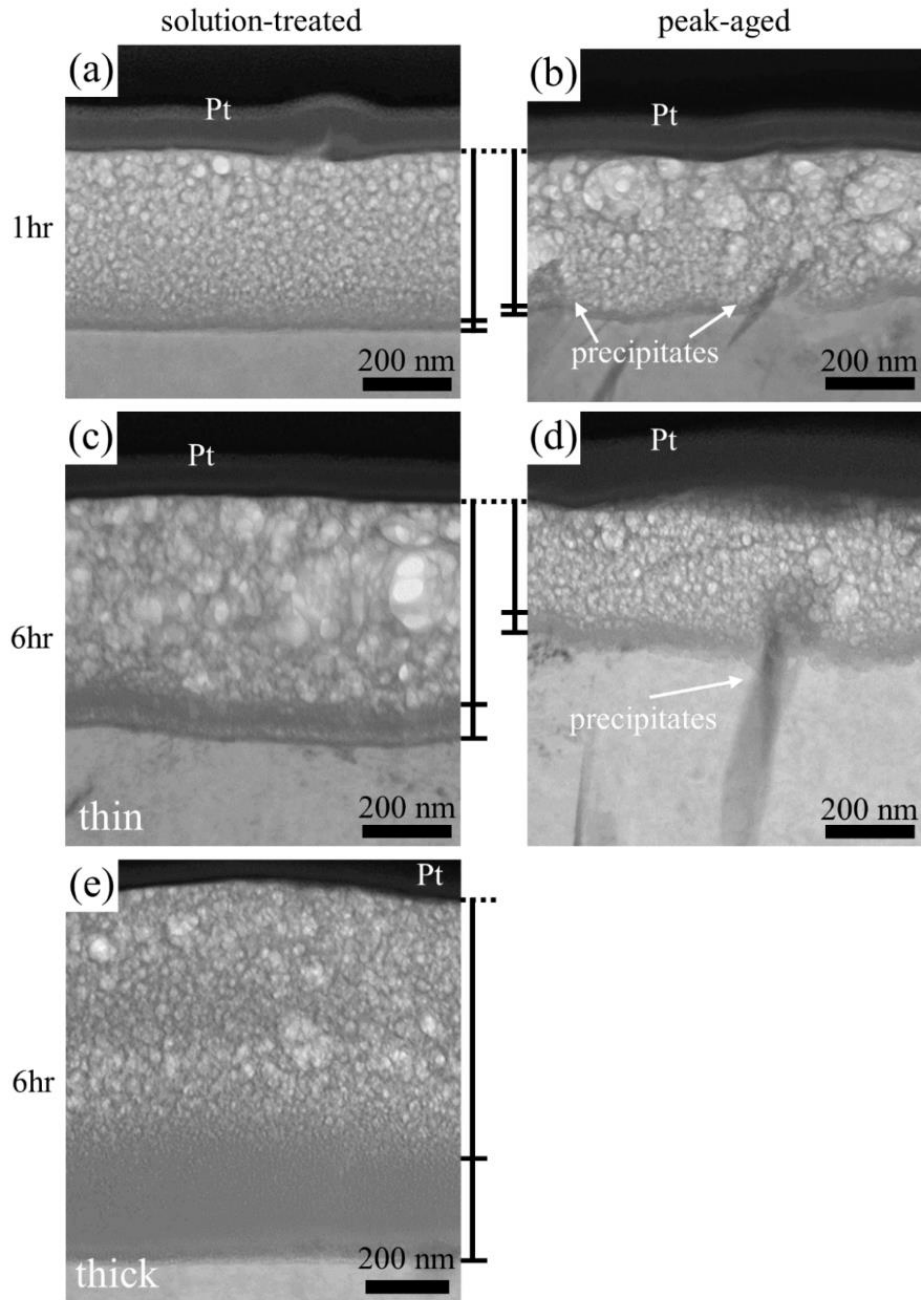


Figure 2.8 Cross sectional TEM images of the corrosion films after 1 hour and 6 hours of immersion for solution-treated and peak-aged WE43 alloy. (c) and (e) are from the thin and thick regions indicated in **Fig. 2.4(c)**.



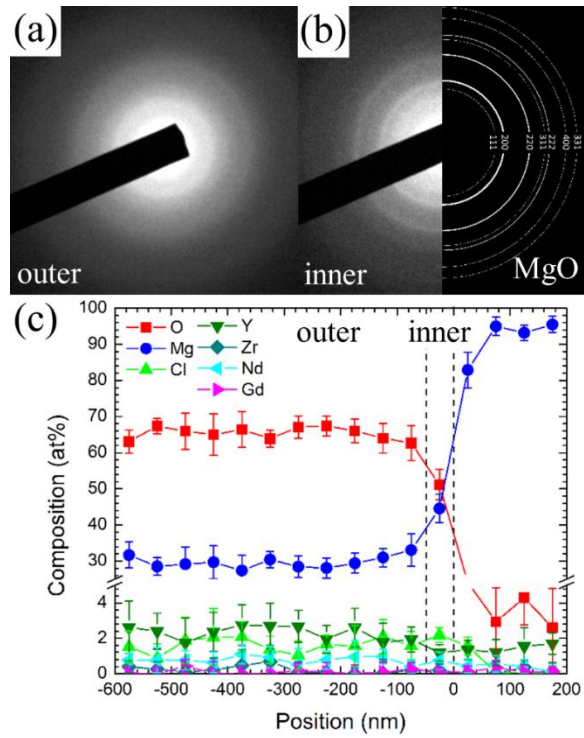


Figure 2.9 Electron diffraction patterns of (a) outer and (b) inner layers, and (c) the EDS compositional depth profile of the corrosion film on solution-treated WE43 after 6 hours of immersion shown in **Fig. 2.8(c)**.

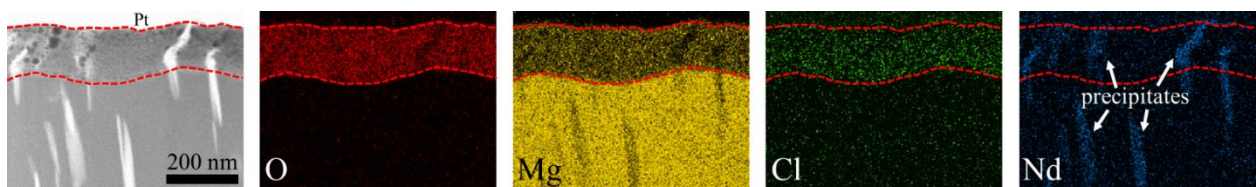


Figure 2.10 EDS mapping of the corrosion film on peak-aged WE43 after 6 hours of immersion.

Since the regions characterized by TEM are small, we will not attempt to quantitatively link the observed thickness of the corrosion film with the overall corrosion rate. However, it appears that the local thickness of the interfacial MgO layer correlates with the thickness of the



overall corrosion layer and therefore with local corrosion rate (**Fig. 2.8(c-e)**). The formation mechanism of the corrosion film and the relationship with the alloy microstructure will be discussed in next section.

## 2.4 Discussion

Both solution-treated and peak-aged WE43 shows a uniform corrosion morphology, i.e. no localized corrosion, when tested in 3.5 wt% NaCl solution saturated with  $\text{Mg(OH)}_2$ . This is in contrast with a previous study by Przondziono *et al.* [106] who reported localized pitting corrosion on as-extruded WE43 alloys tested in NaCl solutions. The uniform corrosion morphology reported here may be attributed to the change of microstructure after heat treatment.

The observation of hydrogen bubbles forming on the sample surface indicates the presence of second phase particles in the alloy, which accords with another study [107] on pure Mg and AZ series alloys published at the same time as this work. Three types of second phases (Zr-rich, Y-rich and finely dispersed precipitates) were observed on the as-polished surface. However, only the Zr-rich particles were found responsible for the hydrogen bubbles and formation of the domes, explained by microgalvanic effect where the Zr-rich particles serve as effect local cathodes. Indeed, the Zr-rich particles have the highest Volta potential difference with respect to the Mg matrix compared to other possible intermetallic second phases and precipitates [108, 109], and this is attributed to the inclusion of noble impurity elements, such as Fe, Ni, Cr, as discussed in **Section 1.3.2.**

The accumulation of  $\text{Mg(OH)}_2$  into the dome structures comes from the cathodic reaction 2.3 taking place at the Zr-rich particles, where the reduction of water molecules is accompanied

by the formation of  $H_2$  molecules and an increase in local pH value. The saturation of the test solution with  $Mg(OH)_2$  ensures that  $Mg(OH)_2$  can form readily. The observed hemispherical dome structure (**Fig. 2.5**) can be rationalized from a radially symmetric distribution of the pH values developing from a single point on the surface at the location of the Zr-rich particles. Because of the porous structure of the domes, the cathodic effect of the particles is maintained even after the formation of the domes. The locally increasing pH value around the Zr-rich particles also protects the neighboring region from corrosion as demonstrated by the deposition of  $Mg(OH)_2$  on the surface (**Fig. 2.7**). A schematic illustration of the formation process of the domes is shown in **Fig. 2.11(a)** below.

The presence of domes has been reported previously in different Mg alloys [61, 108, 110]. The domes formed over  $Al_8Mn_5$  precipitates in an AM50 alloy tested in 1.6 wt% NaCl solution [61] were reported to have two distinct phases: an inner section of MgO and an outer layer of  $Mg(OH)_2$ . This differs from the continuous  $Mg(OH)_2$  structure with a dehydrated MgO outer portion shown in **Fig. 2.6**. However, partial Al dissolution from the  $Al_8Mn_5$  particles under increasing pH make the dome formation process in Ref. [61] more complex.

Because of the local protective effect by the domes, the dominant corrosion reaction occurs on the regions away from the domes, which is galvanically coupled with the Zr-rich particles as anodes. Therefore, it is not surprising that a bi-layered structure of the corrosion film, similar to that previously reported for different Mg alloys [111-113], was observed away from the domes. The alloying elements from the WE43 matrix are found to be incorporated into the corrosion film; however, unlike Al in AM50 alloys [60] and Zn in AZ series [49, 62, 63, 114] and ZE series alloys [63, 114], no interfacial enrichment of the alloying elements at the film/alloy interface was observed. Even though the alloying elements are present inside the corrosion film, the film

microstructure does not change dramatically compared to the film formed on pure Mg immersed in NaCl solutions [112]. The proposed increase of passivity of surface corrosion film by incorporation of alloying elements proposed in Ref. [37, 64-66] cannot be confirmed and further investigations are still needed.

Based on the observed microstructure of the corrosion film, the film formation mechanism can be proposed as follows. Two reaction fronts, one for the oxidation reaction and one for the hydration reaction, propagate inward during the corrosion process, resulting in the bi-layered Mg(OH)<sub>2</sub>/MgO structure. This is consistent with the theory by Taheri *et al.* [112] that the inner MgO layer is formed by oxidation of Mg alloys and the outer Mg(OH)<sub>2</sub> layer is formed by the hydration of inner MgO layer. Because of the porosity of the corrosion film, the water molecules and solvated ions can easily penetrate through the layers for the corrosion reactions to proceed. According to an isotopic tracer study of the corrosion film growth on Mg alloys [114], the film growth mechanism is dominated by inward transport of oxygen and hydrogen diffusion rather than by the outward diffusion of Mg. The finely dispersed precipitates in peak-aged WE43 are embedded into the surface film after the corrosion reactions, again confirming the inward growth mechanism of the corrosion film, as reported in the literature [49, 63, 113].

In peak-aged WE43, even though the precipitates do not form a continuous network and cannot serve as a corrosion barrier similarly to the mechanism suggested by Song *et al.* for AZ91 [83], the spacing between precipitates are fine enough (50 to 200 nm) to interact with the propagation of corrosion fronts, contributing to a rough film/alloy interface (**Fig. 2.8 and 2.10**). Since the outer Mg(OH)<sub>2</sub> layer is highly porous and provides an easy penetration path for the solution [113], the propagation of the hydration front is believed to be unchanged despite the embedded precipitates in the film. Therefore, the main role of the precipitates appears to interact

and slow down the propagation of the oxidation front. The thinner interfacial MgO layer on peak-aged WE43, compared to that of solution-treated WE43, is also consistent with a slower propagation of oxidation. A schematic illustration of the propagation of oxidation and hydration fronts, and the interaction with the precipitates, is shown in **Fig. 2.11(b)**. After long-term immersion (>5 days), parts of the corrosion film on solution-treated WE43 fell off easily, while the film on peak-aged WE43 showed a better adhesion to the alloy surface. While the thicker corrosion films on solution-treated WE43 may develop larger stresses, changes of the film/alloy interfacial properties due to precipitate interactions could also contribute to the observed differences.

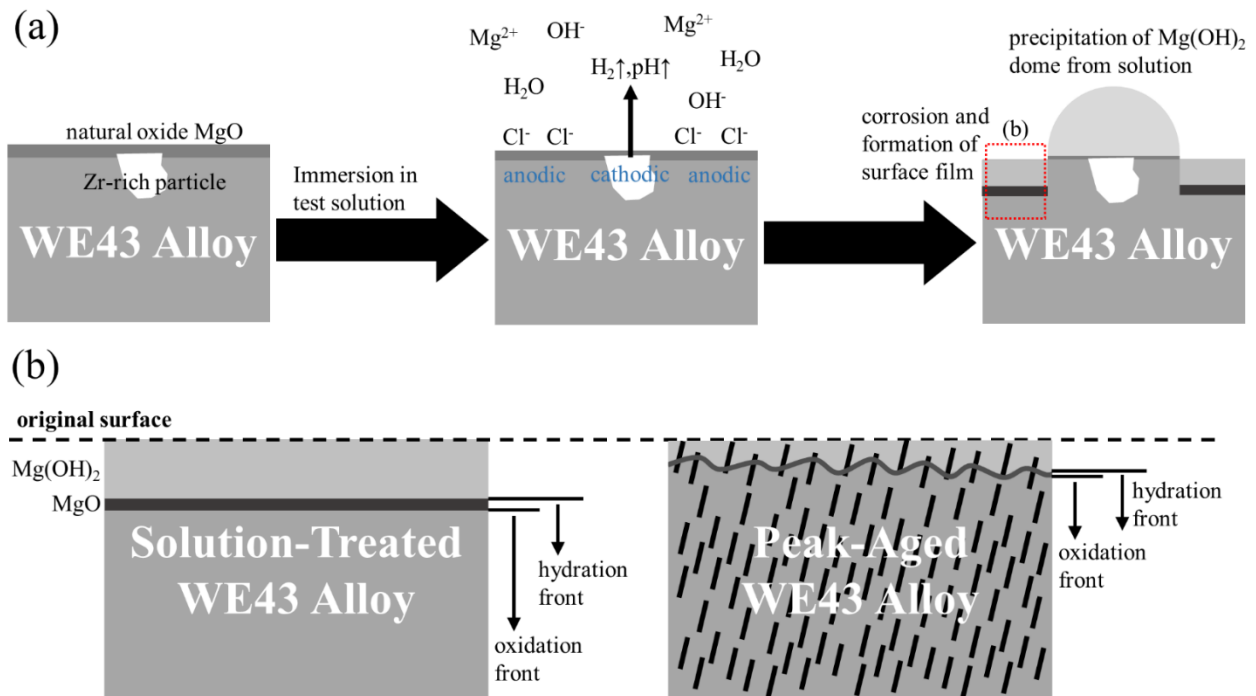


Figure 2.11 Schematic illustration of the proposed corrosion models. (a) Microgalvanic effect of the Zr-rich particles and (b) corrosion film formation mechanism and the effect of the finely dispersed precipitates on the corrosion evolution.

The local inhomogeneity of the corrosion rate on solution-treated WE43 may be attributed to local variations of the chemical composition that were previously reported [99]. It was argued that the presence of Nd and Y in solid solution might improve the corrosion resistance by forming a more protective corrosion layer [37, 65, 66, 115]. Whether solute concentration variations play a role in the development of thin and thick corrosion layer on solution-treated sample could not be confirmed. However, peak aging decreases the matrix solute concentrations through precipitation; yet it is associated with slower corrosion kinetics. Therefore, it is believed that the presence of finely dispersed precipitates in the peak-aged alloy plays a prominent role in interacting with and slowing down the inward propagation of the corrosion reactions.

## **2.5 Conclusions**

The corrosion behavior of solution-treated and peak-aged WE43 in a NaCl solution was investigated across different length scales to understand the general corrosion feature and the relationship between corrosion behavior and the underlying second phases. The new findings are summarized as follows:

1. A uniform corrosion morphology without localized corrosion was observed for both solution-treated and peak-aged WE43.
2. Protruding  $\text{Mg}(\text{OH})_2$  domes were found to form on Zr-rich impurity particles by a microgalvanic effect. The dome regions are protected by the local increase of pH value and deposition of  $\text{Mg}(\text{OH})_2$  on the surface.

3. The dominant corrosion reactions occur away from the dome regions. A bi-layered corrosion film microstructure was revealed by TEM/STEM investigation showing a porous outer  $\text{Mg}(\text{OH})_2$  layer on top of an inner MgO layer. This bi-layered structure is proposed to form by inward propagation of the corrosion front and sequential oxidation and hydration reactions. The finely dispersed precipitates after aging treatment decreases the corrosion rate of WE43 alloy by interacting with the propagation of corrosion reactions.

**CHAPTER 3:**  
**Hydrogen Evolution and Localized Corrosion during Anodic Polarization of  
a Peak-Aged Mg-Y-Nd-Zr Alloy<sup>2</sup>**

**3.1 Motivation**

In **Chapter 3**, a uniform corrosion morphology was observed on a WE43 alloy during free immersion in a NaCl solution, and detailed characterization of the corrosion products clarify the effect of second phases in hydrogen evolution and corrosion of Mg alloys. During anodic experiments, however, localized corrosion, accompanied by the evolution of hydrogen gas, was observed on the same peak-aged WE43 alloy. Therefore, anodic polarization can be used to initiate and control localized corrosion on this alloy, providing a unique condition for experiments to understand the relationship between the corrosion microstructure developing in localized corrosion regions and the abnormal hydrogen evolution under anodic polarization, i.e. NDE.

---

<sup>2</sup> The results presented in this chapter were published in:

P.W. Chu, E.A. Marquis, Anodic Hydrogen Evolution and Localized Corrosion during Galvanostatic Polarization of a Peak-Aged Mg-Y-Nd-Zr Alloy, *J. Electrochem. Soc.*, 163 (2016) C402-C409 doi: 10.1149/2.0201608jes.

Reprinted with permission from *J. Electrochem. Soc.*, 163, C402 (2016). Copyright 2016, The Electrochemical Society.

## 3.2 Materials and Methods

### 3.2.1 Materials and Sample Preparation

A bar of wrought WE43 alloy was provided by Magnesium Elektron Ltd. The composition of the alloy was given in **Table 2.1** in previous chapter. The samples were solution-treated at 525°C for 8 hours, followed by aging at 250°C for 16 hours to reach the peak hardness [98, 99]. Under this aging condition, finely dispersed Nd and Y rich  $\beta_1$  and  $\beta$  precipitates formed throughout the grains and along the grain boundaries, as shown in **Fig. 2.1(c)** in previous chapter.

The heat-treated samples were then mounted in Buehler EpoThin epoxy with an exposed surface area of 1 cm<sup>2</sup>. A Teflon insulated silver-plated copper wire was connected to the rear side for electrical connection. Before each electrochemical test, the samples were ground to 1200 grit in an alcohol-based lubricant, cleaned with anhydrous alcohol, and dried in flowing dry air.

### 3.2.2 Electrochemical Tests

All electrochemical tests were performed in a 0.1M NaCl (pH~6.5) solution prepared with laboratory grade reagents and deionized water. 200 mL of solution was used in each test. A conventional three-electrode configuration was used with the peak-aged WE43 sample as working electrode, a saturated calomel electrode (SCE) as reference electrode and a high-density graphite bar as counter electrode. An Ivium Vertex potentiostat/galvanostat controlled by IviumSoft software was used for all tests. Potentials presented in this study are all referred to the SCE.

An upside-down centrifuge tube filled with the test solution was placed over the sample during the tests to collect evolved hydrogen gas and monitor the hydrogen evolution rate. For



selected samples, an AmScope stereo microscope with a CCD camera was used to record the surface morphology change and hydrogen evolution sites under polarization.

Galvanostatic polarization with current density ranging from -10 to 10 mA/cm<sup>2</sup> was applied to investigate the sample responses and hydrogen evolution rates. The samples were held at open circuit for 10 minutes to reach a stable potential before application of the current. A total charge of 15 C/cm<sup>2</sup> was passed for each current density. Duplicated experiments were performed for each condition to verify the reproducibility.

The cathodic responses of anodic polarized samples were investigated by recording the cathodic potentiodynamic polarization curves after anodic polarization for a charge of 2 C/cm<sup>2</sup>. This amount of charge was chosen because localized corrosion features are visible on the sample surface but no significant change of solution pH was observed. The samples were held in the same test solution for 30 seconds after polarization before measuring the cathodic polarization curves. A baseline sample, without anodic polarization, was held at open circuit for 10 minutes and tested. The cathodic polarization scan was performed from the open circuit potential (OCP) downwards at a rate of 1 mV/s to -700 mV vs OCP. Each scan was performed twice on freshly anodic polarized samples to ensure reproducibility of the experiments.

### ***3.2.3 Microstructure Characterization***

A FEI Helios Nanolab 650 scanning electron microscope/focused ion beam (SEM/FIB) system was used for the microstructure characterizations. A standard site-specific liftout process was used for preparing cross section TEM samples [102], with the surface of the sample protected by depositing a layer of platinum (Pt) and a final cleaning step with 2kV Ga ions. A Leica

cryogenic stage (T=150 K) was used during the thinning process to minimize possible beam damage during ion milling (**Appendix I**).

A JEOL 2010F analytical TEM was used to perform cross sectional microstructure characterizations. A Gatan 636 cooling holder (T=150 K) was used during TEM observations to minimize degradation of the corroded regions during imaging (**Appendix I**). X-ray energy dispersive spectroscopy (EDS) mapping was performed using a Hitachi HD-2300A scanning transmission electron microscopy (STEM) equipped with an Oxford EDS detector and the EDS spectrum images were analyzed with the Oxford INCA software.

### **3.3 Results**

#### ***3.3.1 Hydrogen Evolution Rate under Galvanostatic Polarization***

The volume of collected hydrogen gas as a function of time under galvanostatic polarization was measured at different applied cathodic and anodic current densities. Under cathodic polarization (**Fig. 3.1(a)**), the hydrogen evolution rate increased with increasing applied current density, which is expected because reduction of water and evolution of hydrogen gas is the dominant cathodic reaction and the rate is proportional to the applied cathodic currents. Under anodic polarization (**Fig. 3.1(b)**), the hydrogen evolution rate also increased with increasing applied current density, which is an evidence of the NDE. From these measurements, an average hydrogen evolution rate, which is the average of the slopes between each data points shown in **Fig. 3.1**, was calculated and plotted as a function of the applied current density (**Fig. 3.2**). The hydrogen evolution rate decreased with decreasing applied cathodic current density and increased with

increasing applied anodic current density, i.e. a NDE phenomenon. A minimum hydrogen evolution rate was reached at open circuit condition.

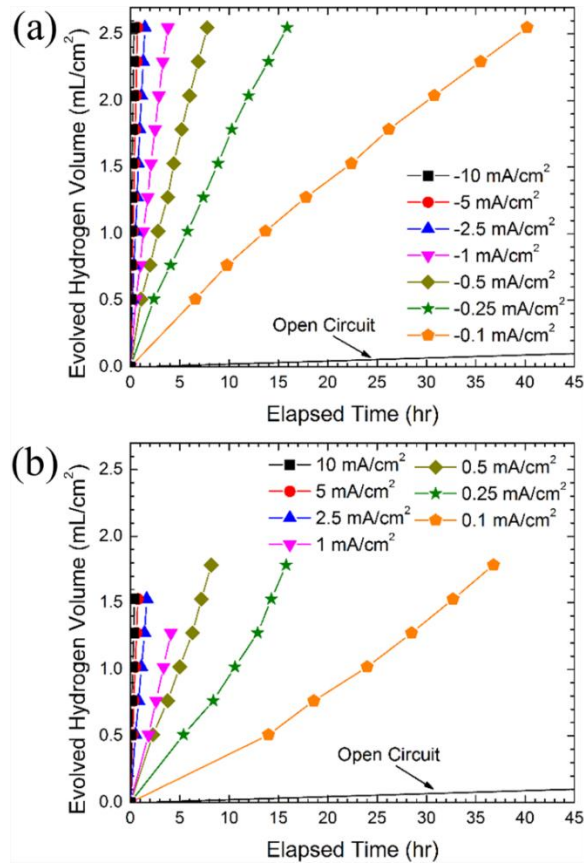


Figure 3.1 Volume of evolved hydrogen collected as a function of application time for peak-aged Mg-Y-Nd-Zr alloy in 0.1M NaCl solution under galvanostatic polarization at different (a) cathodic and (b) anodic current densities. A total charge of 15 C/cm<sup>2</sup> was applied.

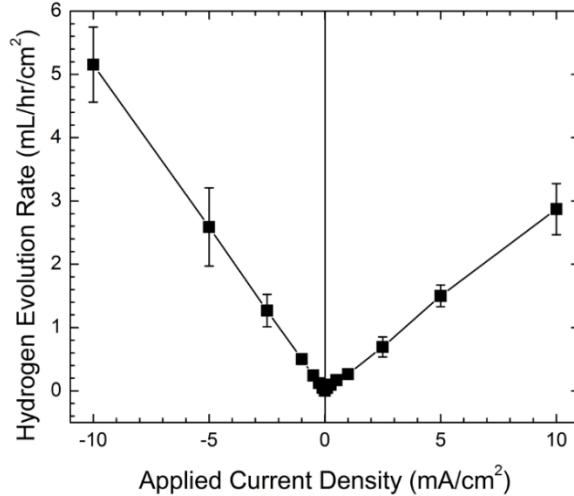


Figure 3.2 Average hydrogen evolution rates, calculated by averaging the slopes between each data points in **Fig. 3.1**, as a function of applied current density. The error bars shown here are the standard deviations of the slopes.

A polarization curve resulting from the galvanostatic polarization experiments is obtained by plotting the applied current density,  $i_{\text{appl}}$ , against the steady state potential measured at the end of each galvanostatic polarization (**Fig. 3.3(a)**). It should be noted that the steady state potentials here are not corrected for the ohmic potential drops. The current densities calculated from the hydrogen evolution rates,  $i_{\text{H}_2}$ , by assuming an ideal gas behavior for hydrogen [28], are also plotted in **Fig. 3.3(a)** for comparison. It is clear that  $i_{\text{H}_2}$  follows closely with  $i_{\text{appl}}$ , even though under anodic polarization the applied current opposes the cathodic reaction. The currents  $i_{\text{H}_2}$  and  $i_{\text{appl}}$  overlap with each other under cathodic conditions, while  $i_{\text{H}_2}$  are consistently lower than  $i_{\text{appl}}$  under anodic conditions.

The ratio between  $i_{\text{H}_2}$  and  $i_{\text{appl}}$  is plotted against the applied current density in **Fig. 3.3(b)**. Under cathodic polarization, the ratio is about 1 suggesting that the reaction rate of hydrogen

evolution is controlled by the applied cathodic currents. The  $i_{H_2}/i_{appl}$  ratio drops slightly below 1.0 under low cathodic current densities perhaps due to some dissolution of hydrogen gas into the test solution. Under anodic polarization, the  $i_{H_2}/i_{appl}$  ratio drops with increasing anodic current densities and is stabilized around 0.5 to 0.6 under large anodic polarization. These results are similar to prior observations on pure Mg [40, 116] and other Mg alloys [117].

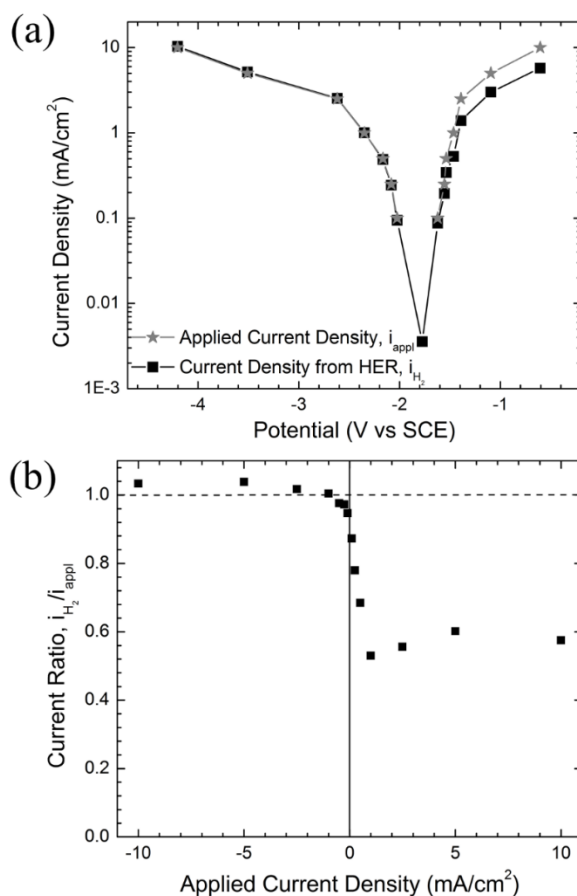


Figure 3.3 (a) Applied current density,  $i_{appl}$ , and current density inferred from hydrogen evolution rate,  $i_{H_2}$ , as a function of steady state potential. The potential values are not corrected for ohmic potential drops. (b) Ratio of the current density calculated from hydrogen evolution rate to the applied current density,  $i_{H_2}/i_{appl}$ , as a function of applied current density.

### 3.3.2 Localized Corrosion Induced by Anodic Polarization

During anodic polarization experiments, the evolution of response potential was also monitored and selected curves are shown in **Fig. 3.4**. For all anodic current densities, the potential increased initially and dropped after some amount of time that varied with the applied anodic current density. The initial potential increase suggests that the sample surface is passivated by the presence of a surface film formed after 10 minutes of immersion at open circuit. The subsequent drop indicates a breakdown of the surface film and correlates with the initiation of localized corrosion, which takes place more rapidly with increasing anodic current density.

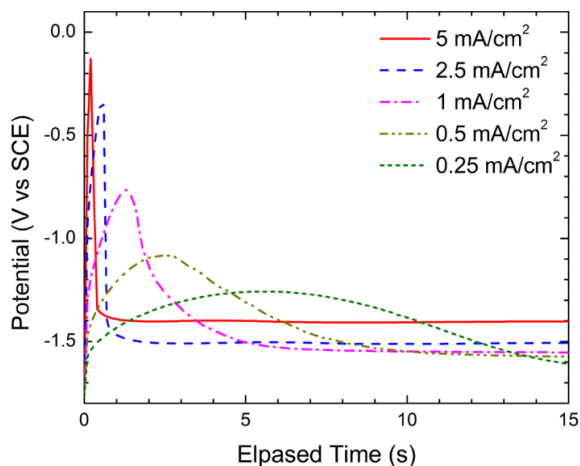


Figure 3.4 Evolution of the potential under galvanostatic anodic polarization for different applied current densities. The potentials here are not corrected for ohmic potential drops.

To correlate hydrogen evolution with localized corrosion, the initiation of localized corrosion under anodic polarization at 1 mA/cm<sup>2</sup> was monitored by *in situ* optical microscopy. **Fig.**

**3.5(a)** shows a snapshot of the surface at 2 seconds after application of the polarization. Rising streams of hydrogen gas are observed locally on the sample surface (arrowed). The larger hydrogen bubbles formed during initial holding at OCP and initiated on Zr-rich impurity particles as discussed in previous chapter. Another snapshot after application of the current for 60 seconds (**Fig. 3.5(b)**), with the current switched off, shows small localized corrosion regions (arrowed) at the sites where the hydrogen gas was seen to evolve. Comparing with unpolarized condition in previous chapter, we note that the large hydrogen bubbles remain unaffected by the anodic polarization.

The effect of applied anodic current density on the surface morphologies exposed to 15 C/cm<sup>2</sup> of charge under different anodic polarization is shown in **Fig. 3.6**. The coverage of the corroded region increased with increasing applied anodic current density. The corrosion regions formed preferentially around the edge of the samples, possibly due to an edge effect on the current density distribution, but localized corrosion can still be found in the center of the samples, especially under high anodic current densities. These corrosion morphology agrees with previous observations on pure Mg after anodic polarization [39, 118].

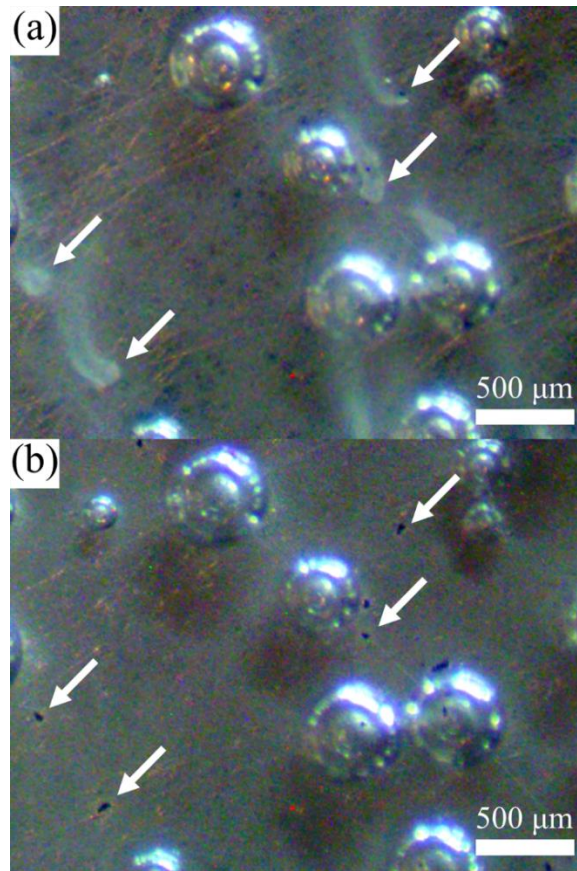


Figure 3.5 *In situ* OM observations. (a) Image taken at 2 seconds under anodic polarization at 1 mA/cm<sup>2</sup>. (b) The same area after 60 seconds of anodic polarization. The image was taken after the polarization stopped.



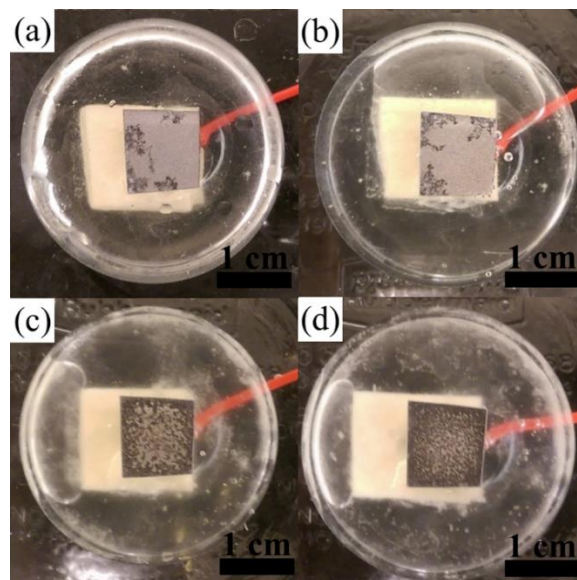


Figure 3.6 Surface morphology after galvanostatic anodic polarization at (a) 0.25, (b) 0.5, (c) 2.5 and (d) 10 mA/cm<sup>2</sup> (Charge passed: 15 C/cm<sup>2</sup>).

### 3.3.3 Microstructure of the Localized Corrosion

In order to understand the relationship between the localized corrosion induced by anodic polarization and the abnormal hydrogen evolution, galvanostatic polarization at 1 mA/cm<sup>2</sup> for 5 seconds was performed on the sample. According to the potential evolution shown in **Fig. 3.4**, localized corrosion has already initiated by this time. The polarized sample was removed from the test solution immediately and transferred to a SEM/FIB microscope for microstructure analysis of the localized corrosion regions.

Small holes, in a size of about a few  $\mu\text{m}$ , were found on the surface of the polarized sample at the locations where rising streams of hydrogen gas were observed (**Fig. 3.7(a)**). These holes confirm the local breakdown of surface film and the initiation of localized corrosion. Cross sectional observations at the hole shown in **Fig. 3.7(a)** revealed a localized corrosion region about

10  $\mu\text{m}$  wide and 5  $\mu\text{m}$  deep (**Fig. 3.7(b)**). Finely dispersed precipitates can be seen in both the uncorroded alloy and the corrosion region by high angle annular dark field (HAADF) STEM observation of the same cross section (**Fig. 3.7(c)**), finely dispersed precipitates can be seen in both the uncorroded alloy and the corrosion region. The corrosion region that is porous extends into the alloy by forming finger-like features, which are also porous (**Fig. 3.8**). The localized corrosion region expands with increasing polarization time, as shown in **Fig. 3.9**. No film-free region as suggested in previous models [21, 119] was observed at the front of the developing localized corrosion regions. The finger-like features are present at the propagation front of the corrosion region even after extended polarization time.

STEM EDS mapping (**Fig. 3.10**) was also performed in order to understand the chemistry of the localized corrosion region. The O distribution highlights the corrosion region and presents the same finger-like features shown in the secondary electron (SE) STEM image (**Fig. 3.10(a)**). The Cl distribution also follows closely with the corrosion region, implying that localized corrosion proceeds by reaction with the NaCl test solution. However, no Na peak was observed in the EDS spectrum. The distribution of Nd highlights the location of the precipitates, and the similarities between the corroded and uncorroded regions indicate that the precipitates do not dissolve during the propagation of the localized corrosion front. No interfacial or surface enrichment of O, Cl, or any of the alloying/impurity elements is observed.

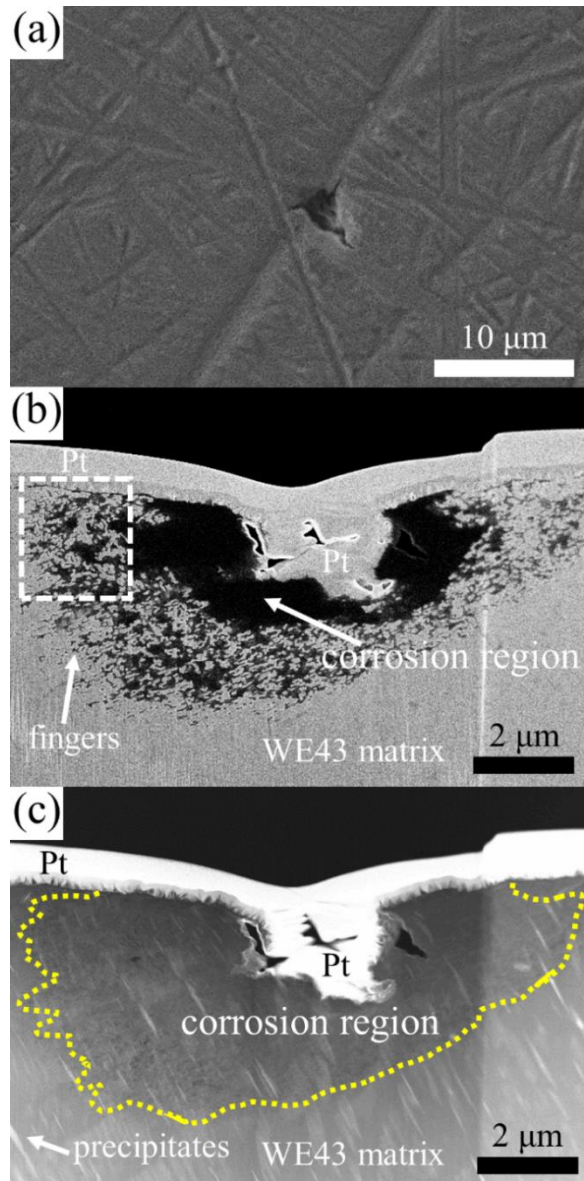


Figure 3.7 Same localized corrosion region formed after anodic polarization at  $1 \text{ mA/cm}^2$  for 5 seconds imaged with (a) top-view SEM image using the secondary electron (SE) detector, (b) cross sectional SEM image using the SE detector showing the finger-like corrosion front morphology, and (c) cross sectional high angle annular dark field (HAADF) STEM image showing the finely dispersed precipitates presented in both the corrosion region and WE43 matrix. Yellow dashed line outlines the interface between corrosion region and WE43 matrix.

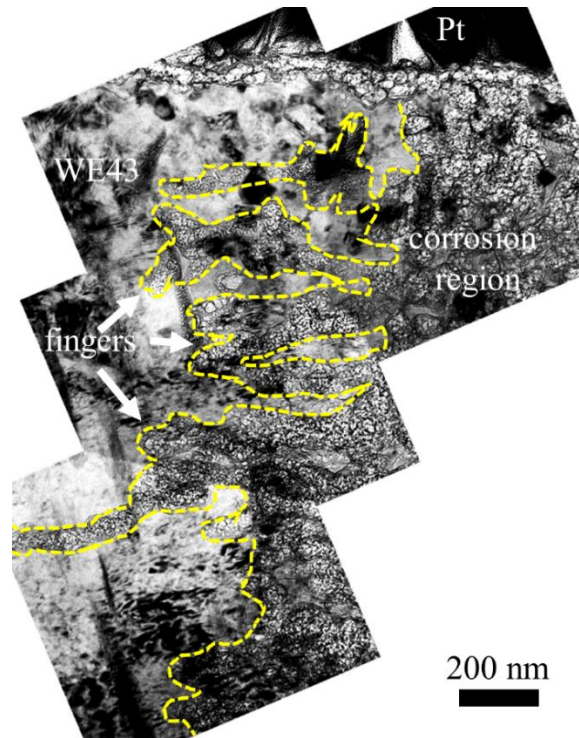


Figure 3.8 Cross sectional bright field (BF) TEM image of the edge of the same localized corrosion region (the box shown in **Fig. 3.7(b)**) formed after anodic polarization at  $1 \text{ mA/cm}^2$  for 5 seconds showing the porous structure and finger-like features. Yellow dashed line outlines the interface between corrosion region and WE43 matrix.

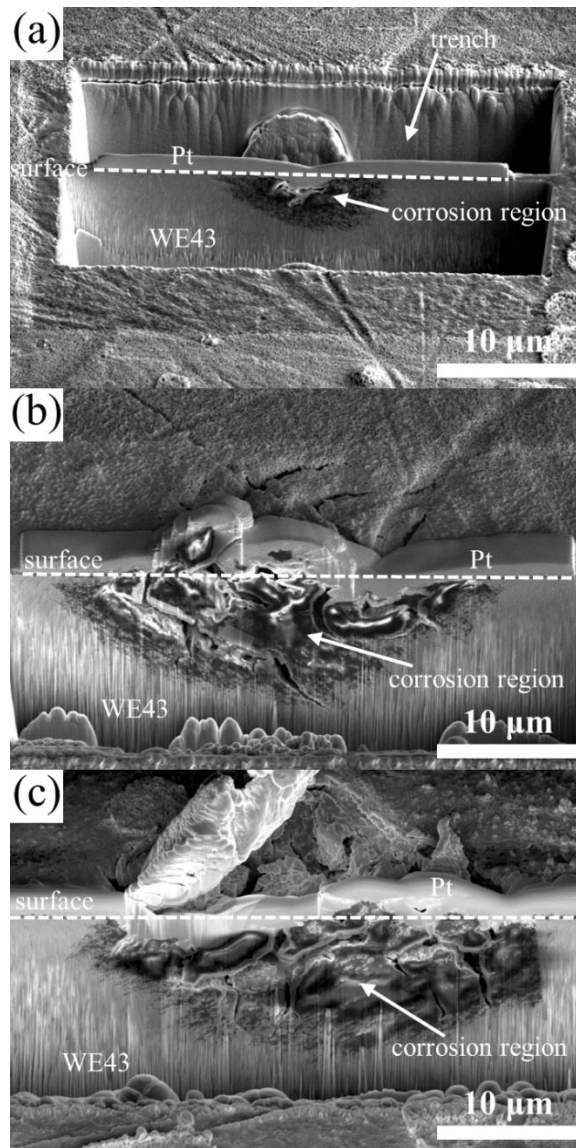


Figure 3.9 Cross sectional SEM/FIB images showing the evolution of localized corrosion regions after anodic polarization at  $1 \text{ mA/cm}^2$  for (a) 5, (b) 30 and (c) 120 seconds. (Another trench is also present on the opposite side in (a) because this is during a TEM specimen preparation.)

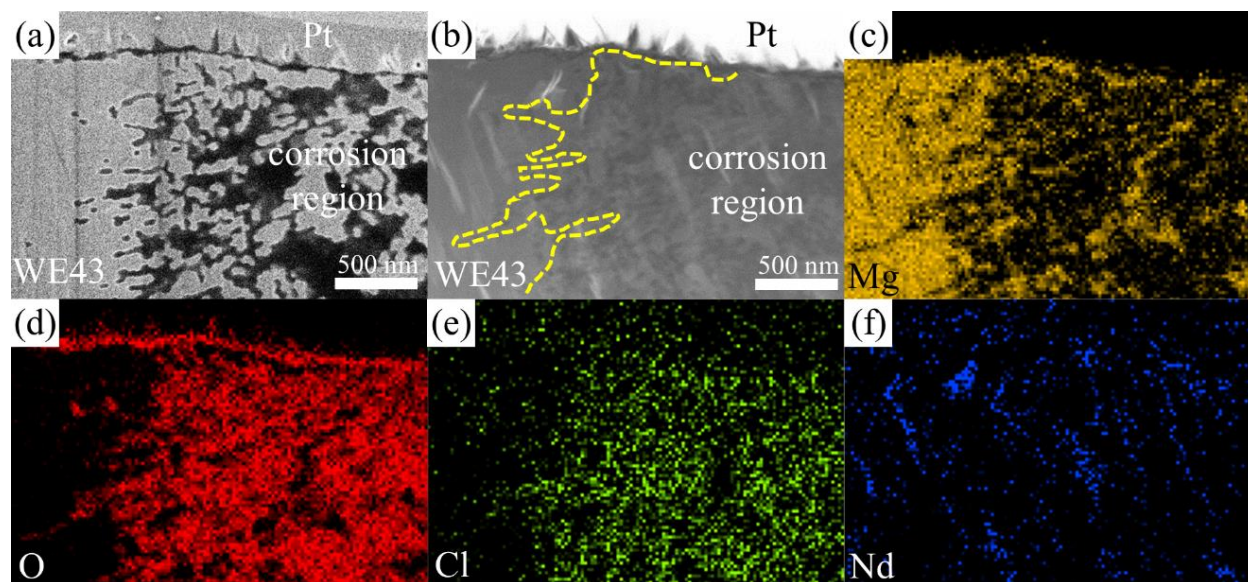


Figure 3.10 (a) SE, (b) STEM cross sectional images, and (c)-(f) the corresponding elemental EDS maps taken from the edge of the same localized corrosion region (the box shown in **Fig. 3.7(b)**) formed after anodic polarization at  $1 \text{ mA/cm}^2$  for 5 seconds. Yellow dashed line in (b) outlines the interface between corrosion region and WE43 matrix, which was determined using the O map.

The average composition of the corroded region obtained from 25 separate locations including Nd and Y-rich precipitates is shown in **Table 3.1**. The average O/Mg ratio of the localized corrosion region is  $2.1 \pm 0.3$ , which is close to the stoichiometry for  $\text{Mg(OH)}_2$ . Selected area electron diffraction (SAED) also confirms the presence of  $\text{Mg(OH)}_2$  in the corrosion region (**Fig. 3.11**).



Table 3.1 EDS chemical composition of the localized corrosion region after anodic galvanostatic polarization at 1 mA/cm<sup>2</sup> for 5 seconds averaged from 25 separate measurements.

	O	Mg	Cl	Y	Nd	Zr	Gd	O/Mg
at%	65.2	31.7	1.5	1.0	0.4	0.1	<0.1	<b>2.1±0.3</b>

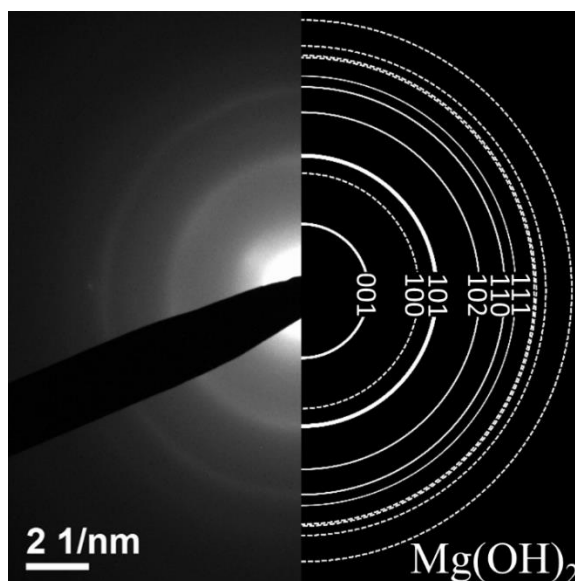


Figure 3.11 Selected area electron diffraction (SAED) from the corrosion region compared to Mg(OH)<sub>2</sub> diffraction ring pattern generated from Powder Diffraction File 44-1482.

### 3.3.4 Cathodic Response of Anodic Polarized Samples

It was previously suggested that the increase in the cathodic activity during anodic polarization may be responsible for the abnormal hydrogen evolution [39, 116]. Therefore, the cathodic response of the WE43 alloy after anodic polarization was also investigated. **Fig. 3.12(a)** shows selected cathodic polarization curves recorded after galvanostatic polarization at different

anodic current densities after 2 C/cm<sup>2</sup> of charge passed. The cathodic polarization curve moves toward higher cathodic current with increasing applied anodic current density. However, when comparing the cathodic polarization curves without prior anodic polarization, which was immersed at open circuit for 10 minutes, to those after anodic polarization, the cathodic current responses are in the same order of magnitude and higher than most of the curves after anodic polarization, even though the anodic polarized sample was covered by dark localized corrosion regions (**Fig. 3.12(b)**) and the un-polarized appeared uncorroded (**Fig. 3.12(c)**). Also, the measured hydrogen evolution rates during anodic galvanostatic experiments are a few orders of magnitude higher than at open circuit condition. The cathodic current densities at -2.3 V vs SCE were summarized in **Table 3.2**. This suggests that the increase of catalytic activity of sample surface after the formation of dark localized corrosion regions may not play a dominant role in the NDE behavior on peak-aged WE43 alloy.

Table 3.2 Current densities at -2.3 V vs SCE for cathodic polarization measurements on anodic polarized samples after 2 C/cm<sup>2</sup> of charge passed.

<b>Applied Anodic Current Density (mA/cm<sup>2</sup>)</b>	<b>10</b>	<b>5</b>	<b>2.5</b>	<b>1</b>	<b>0.5</b>	<b>0.25</b>	<b>0.1</b>	<b>No prior polarization</b>
<b>Cathodic Current Density at -2.3 V (mA/cm<sup>2</sup>)</b>	3.17	2.87	2.71	2.25	1.97	1.93	1.58	2.84



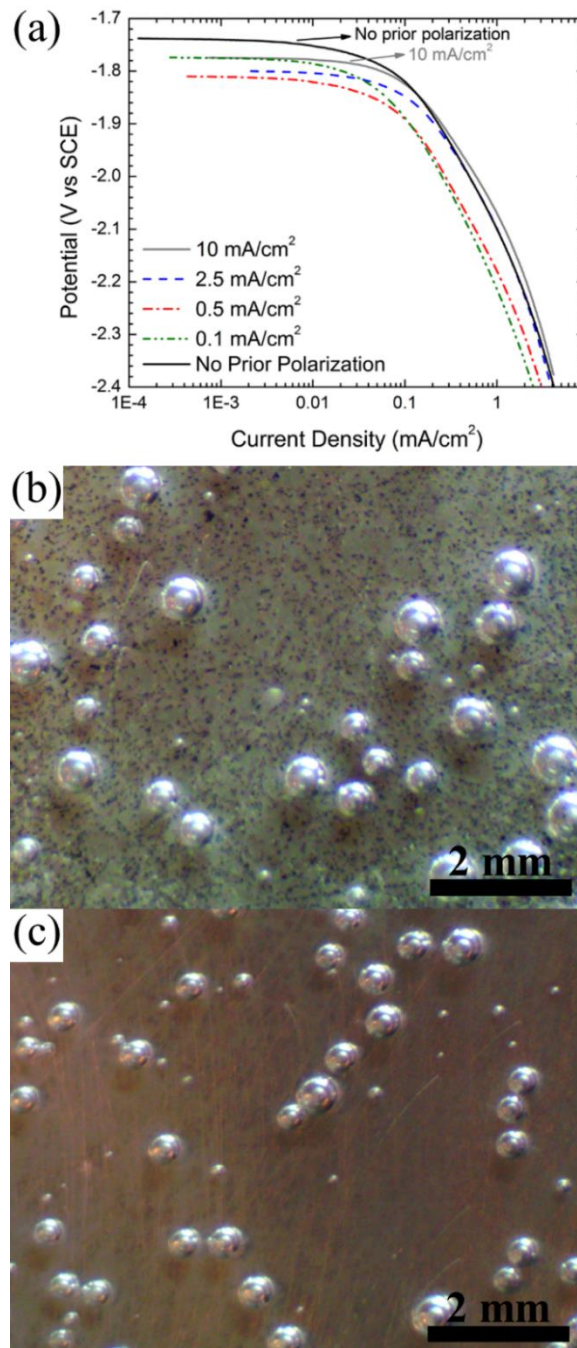


Figure 3.12 (a) Selected cathodic polarization curves of samples without prior polarization and after anodic polarization with 2 C/cm<sup>2</sup> of charge passed, and the corresponding surface morphology right before cathodic polarization test for samples (b) anodic polarized at 10 mA/cm<sup>2</sup> for 2 C/cm<sup>2</sup> and (c) immersed at open circuit for 10 minutes.

### 3.4 Discussion

Hydrogen evolution on Mg alloys can proceed from several sources. As shown in **Chapter 2**, the large hydrogen bubbles shown in **Fig. 3.5** are associated with Zr-rich intermetallic particles containing impurity elements. These particles serve as local cathodes for hydrogen evolution and are the sites for the accumulation of corrosion products protecting the surrounding surface from corrosion. This local cathodic effect not only occurs under free corrosion but is also observed on the anodic polarized samples. Similar behavior was observed in a binary Mg-Fe alloy where the alloy surrounding Fe particles appears undissolved after anodic polarization [117]. The second source of hydrogen during anodic polarization comes from localized corrosion sites (**Fig. 3.5**). Under anodic polarization, the rising streams of hydrogen bubbles coming from the localized region are the dominant source of hydrogen, while the hydrogen evolution from the impurity particles becomes negligible. The hydrogen evolution rates of the aged WE43 alloy under galvanostatic polarization increased with both applied cathodic and anodic current densities (**Fig. 3.2**), showing a clear NDE phenomenon, comparable to pure Mg [40, 120, 121] and a number of Mg alloys [117, 122, 123].

The abnormal hydrogen evolution response on Mg alloys is closely related to the initiation and propagation of localized corrosion. The initiation of localized corrosion can be linked to the breakdown of the surface film, as recorded by the potential evolution under anodic polarization (**Fig. 3.4**). The breakdown of the surface film may be rationalized by the forced dissolution of Mg due to applied anodic currents. This localized corrosion induced by anodic polarization has been reported in the literature for pure Mg under anodic polarization [39, 40, 46, 118, 119]. However, the structure and evolution of the localized corrosion had not been fully characterized. Taheri *et*

*al.*'s results [46] on pure Mg polarized in 0.01M NaCl at -1.0 V vs SCE for 0.5 hour suggest a bi-layered structure composed of an outer Mg(OH)<sub>2</sub>/MgO layer on top of an inner MgO layer. Similarly, Song *et al.* [124] showed that, for pure Mg polarized in saturated Mg(OH)<sub>2</sub> solution at 0 V vs SCE for 24 hours, localized corrosion regions were composed of a loose outer layer on a relatively dense inner layer, and both layers consisted of a mixture of MgO and Mg(OH)<sub>2</sub>. The reported structures disagree with the pure Mg(OH)<sub>2</sub> structure observed in the present work. We believe that the discrepancy comes from our use of a cryogenic stage limits the potential beam damage and modification of the corrosion film occurring during the ion thinning process of TEM specimens. The Mg(OH)<sub>2</sub> structure was also confirmed by the O/Mg ratio quantification from the EDS mapping. The outer corrosion film reported in both reports has a needle/columnar structure, which is characteristic of precipitation of Mg(OH)<sub>2</sub> from the test solution. The absence of this outer layer in the present work could be owing to the relatively short (5 seconds) polarization time, which leads to small pH fluctuation at the surface of localized corrosion regions.

Some of the NDE models [21, 119] proposed a so-called film-free region on the alloy surface ahead of the propagation front of the localized corrosion regions and in contact with the test solution. However, in the cross sectional characterizations shown in **Figs. 3.7-10**, no such film-free region was observed at the alloy surface of the corroded/uncorroded interface. Instead, the observations suggest that the propagation of localized corrosion region is inside the alloy and expands underneath the pre-existed surface film.

The similarities in the Nd distributions observed in corroded and uncorroded regions (**Fig. 3.10(f)**) indicate that the precipitates are not dissolved during the propagation of localized corrosion front. Even though the precipitates are incorporated in the localized corrosion regions,

they are believed to play a minor role on NDE because a similar abnormal anodic hydrogen evolution response was also observed on precipitate-free solution-treated WE43 samples.

To date, the detail mechanism of NDE is still unclear. However, the results in present thesis might provide some information about the mechanism. The ratio between the current density calculated from hydrogen evolution rate and the applied current density,  $i_{H_2}/i_{appl}$ , stabilized around 0.5 to 0.6 under large anodic polarization. Similar values were reported on not only pure Mg [20, 31, 40, 116], but also on Mg-Li alloy [117]. However, the implication of this ratio for the localized corrosion mechanism is still unclear.

Previous proposed “enhanced catalytic activity” model is believed not an important factor here. Indeed, while the NDE is clearly present during anodic polarization, the cathodic current response does not increase after anodic polarization (**Fig. 3.12**), in contrast with previous observations made on pure Mg [39, 40]. More experimental results on localized corrosion will be presented in next chapter and the development of the observed complex morphology of the corrosion front and the underlying mechanisms will be further discussed.

### 3.5 Conclusions

The structure and morphology of localized corrosion induced by anodic polarization, the hydrogen evolution response under galvanostatic polarization, and the cathodic responses after anodic polarization on a peak-aged WE43 alloy are investigated. The new findings are summarized as follows:

1. The early stages of localized corrosion regions induced by anodic polarization was characterized by TEM. Localized corrosion regions, which have a porous Mg(OH)<sub>2</sub> structure, propagate inside

the alloy, underneath the surface corrosion film with a finger-like propagation front. Neither a film-free region, interfacial or surface enrichment of elements, nor impurity particles, are observed.

2. No enhanced cathodic activation was observed when comparing samples with and without prior anodic polarization, indicating the proposed “enhanced catalytic activity” of localized corrosion regions may not play a dominant role in the abnormal hydrogen evolution on Mg alloys during anodic polarization.

**CHAPTER 4:**  
**Microstructure of Localized Corrosion Front on**  
**Pure Mg, Mg-Zn-Ca-Mn, and Mg-Y Alloys<sup>3</sup>**

#### **4.1 Motivation**

In **Chapter 3**, microstructure of localized corrosion initiated by anodic polarization was revealed on WE43 alloy. However, the propagation of localized corrosion and the relationships with underlying alloy structure, such as grain orientation and grain boundaries, are still unclear. Furthermore, localized corrosion also occurred during free immersion on some Mg alloys. Whether the localized corrosion mechanism is the same under free corrosion and anodic polarization or not is unknown. Therefore, Mg alloys with different chemistry and microstructure were investigated under both free immersion and anodic polarization in NaCl solutions in this chapter. The Mg alloys studied are a pure Mg for reference, a Mg-Zn-Ca-Mn alloy with  $\mu\text{m}$ -sized grain, where interfacial enrichment of Zn at the corrosion region/alloy interface was proposed to contribute to “enhanced catalytic/cathodic activity” [49, 51], and a solution treated binary Mg-Y alloy with mm-sized grain, where a solid solution of Y was linked to an improved corrosion

---

<sup>3</sup> The results presented in this chapter were submitted and to be published in:

P.W. Chu, E.A. Marquis, Microstructure of Localized Corrosion Front on Mg Alloys and the Relationship with Hydrogen Evolution, *Corros. Sci.*, under review (2017).

resistance [37]. Localized corrosion behavior and hydrogen evolution responses on the Mg alloys will be discussed based on microscopic observations and electrochemical quantifications.

## **4.2 Materials and Methods**

### ***4.2.1 Materials and Sample Preparation***

A 99.9 wt% pure Mg was provided by Canmet Materials, the Mg-Zn-Ca-Mn alloy was supplied by nanoMag, LLC, and the Mg-Y alloy was provided by Magnesium Elektron Ltd. The chemical compositions measured by inductively coupled plasma mass spectrometer (ICP-MS) are given in **Table 4.1**. Pure Mg and the Mg-Zn-Ca-Mn alloy were studied in the as-received state, while the Mg-Y alloy was solution treated at 550°C for 24 hours. Samples were cut and mounted in Buehler EpoThin epoxy with an exposed surface area of 1.45 cm<sup>2</sup> for the pure Mg and 1 cm<sup>2</sup> for Mg-Zn-Ca-Mn and Mg-Y alloys. All reported hydrogen evolution rates and current densities were normalized with respect to the exposed surface area. A Teflon insulated silver plated copper wire was connected to the rear side for electrical connection. Before tests, samples were ground to 1200 grit in an alcohol-based lubricant, cleaned with anhydrous alcohol, and dried in flowing dry air.

### ***4.2.2 Corrosion and Electrochemical Tests***

Free immersion without external polarization was performed in a 1M NaCl solution, while samples under anodic polarization were tested in a 0.1M NaCl solution. All test solutions were prepared with laboratory grade reagents and deionized water. Solutions were not deaerated. 125 mL of solution was used in each test. A conventional three-electrode configuration was used with

the Mg alloy as working electrode, a saturated calomel electrode (SCE) as reference electrode, and a high-density graphite bar as counter electrode. An Ivium Vertex potentiostat/galvanostat controlled by IviumSoft software was used for all tests. An AmScope stereo microscope with a CCD camera was used to record the surface morphology change and hydrogen evolution sites during tests.

Table 4.1 Chemical composition and impurity level of the studied Mg alloys measured by ICP-MS (wt%).

<b>Sample</b>	<b>Fe</b>	<b>Ni</b>	<b>Cu</b>	<b>Al</b>	<b>Zn</b>	<b>Ca</b>	<b>Mn</b>	<b>Y</b>
<b>Pure Mg</b>	0.002	0.0003	0.0006	0.004	0.009	0.05	0.002	-
<b>Mg-Zn-Ca-Mn</b>	0.002	0.0005	0.002	0.04	1.30	0.41	0.53	-
<b>Mg-Y</b>	<0.005*	<0.002*	<0.02*	<0.01*	-	<0.01*	<0.03*	1.05

\* Impurity level from industry standard AMS4371.

Galvanostatic polarizations with current density of 1 and 10 mA/cm<sup>2</sup> were applied to investigate the localized corrosion behavior and hydrogen evolution responses under anodic polarization. Samples were held under open circuit for 10 minutes to reach a stable potential before application of the polarization. An upside-down centrifuge tube filled with the test solution was placed over the sample during the tests to collect evolved hydrogen gas and monitor the hydrogen evolution rate. A total charge of 10 C/cm<sup>2</sup> was passed for all tested conditions. Details about quantification of the hydrogen evolution rate can be found in **Chapter 3**. A Thermo Scientific



XSeries 2 ICP-MS was used to quantify the amount of  $Mg^{2+}$  dissolved into the solution after anodic polarization tests. All tests were performed at least twice and exhibited good reproducibility.

#### ***4.2.3 Microstructure Characterization***

Samples for electron backscatter diffraction (EBSD) were ground and polished down to 0.05  $\mu m$  colloidal silica, and etched with 5 mL nitric acid, 15 mL acetic acid, 20 mL water, and 60 mL ethylene glycol for 3 seconds. EBSD was performed with a Tescan MIRA3 scanning electron microscopy (SEM) equipped with an EDAX EBSD detector operating at 20 kV. The EBSD patterns were identified by an EDAX TEAM software and analyzed with a TSL orientation imaging microscopy (OIM) software.

Grain boundary chemistry of Mg-Y alloy was analyzed by atom probe tomography (APT). APT samples were prepared with a site specific liftout process along the grain boundary [125] with a FEI Helios Nanolab 650 SEM/focused ion beam (FIB) dual-beam system. Atom probe tomography was performed with a Cameca local electrode atom probe (LEAP) 5000 XR operated in voltage mode. A specimen temperature of 50 K, a detection rate of 0.005 atoms per pulse using, a voltage pulse fraction of 20%, and a repetition rate of 200 kHz were used for data collection. Data reconstruction and analysis were performed using the Integrated Visualization and Analysis Software (IVAS) package 3.6.12.

Immediately after corrosion and electrochemical tests, selected samples were removed from the test solutions, rinsed with deionized water, and transferred immediately to a FEI Helios Nanolab 650 SEM/FIB dual-beam system for microstructure characterization. Cross sectional observations were performed by protecting the region of interest with a Pt layer, followed by site-

specific ion beam milling and SEM imaging. A standard liftout process was used for preparing cross section TEM samples [102], with the surface protected by a deposited Pt layer and a final cleaning step with 2kV Ga ions. A Leica cryogenic stage ( $T \sim 150$  K) was used during the thinning process to minimize ion beam induced degradation of the corrosion products (**Appendix I**).

A JEOL 2010F TEM was used to perform cross sectional observations and electron diffraction analysis. A Gatan 636 cooling holder ( $T = 150$  K) was used during TEM observations to minimize damage of the corrosion product during imaging (**Appendix I**). Diffraction d-spacings were calibrated with the top Pt protective layer. X-ray energy dispersive spectroscopy (EDS) mapping was performed using a Hitachi HD-2300A scanning transmission electron microscopy (STEM) equipped with an Oxford EDS detector, and EDS spectrum images were analyzed using the Oxford INCA software.

## 4.3 Results

### 4.3.1 Alloy Microstructures

Alloy microstructures were characterized before corrosion and electrochemical tests. Pure Mg had a grain size of about 1 mm (**Fig. 4.1(a)**), with few  $\mu\text{m}$ -sized particles containing Fe shown in **Fig. 4.2(a)**. The Mg-Zn-Ca-Mn alloy consisted of an average grain size of about 3  $\mu\text{m}$  (**Fig. 4.1(b)**), with 50-100 nm Mn-rich precipitates and 200-300 nm Zn- and Ca-rich precipitates dispersed inside the grains (**Fig. 4.2(b)**). Segregation of Zn and Ca to grain boundaries was observed by EDS mappings (**Fig. 4.2(c)**). Very occasionally,  $\mu\text{m}$ -sized Mn-rich particles containing minor amounts of Al and Fe with a similar morphology and size as shown in **Fig. 4.2(a)** were also observed. The Mg-Y alloy had an average grain size of about 1.8 mm (**Fig. 4.1(c)**), with

few  $\mu\text{m}$ -sized particles containing Fe that were similar in size to those observed in pure Mg. APT analyses revealed Y segregation to grain boundaries and a random solid solution of Y within the grains (**Fig. 4.3**).

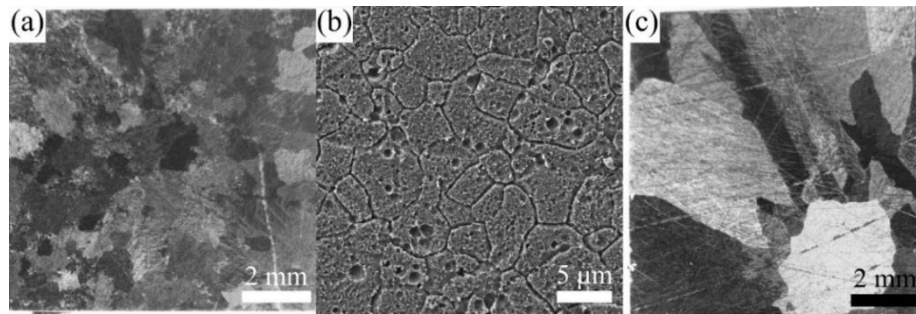


Figure 4.1 Grain structure of the investigated alloys. (a) pure Mg, (b) Mg-Zn-Ca-Mn, and (c) Mg-Y alloys. (a) and (c) are optical microscopy (OM) images, and (b) is a SEM secondary electron (SE) image. Samples were etched with Acetic Glycol for 10 seconds.

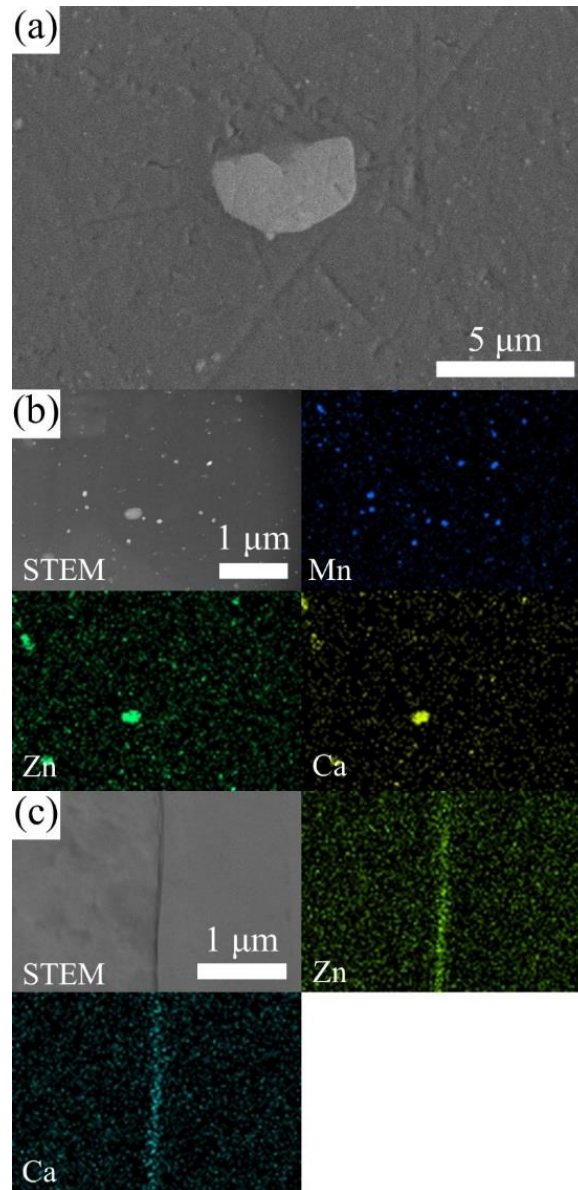


Figure 4.2 (a) a SEM back-scattered electron (BSE) image of a Fe-rich impurity particle on pure Mg. (b) high angle annular dark field (HAADF) STEM image of the precipitates structure in Mg-Zn-Ca-Mn alloy with the corresponding EDS elemental maps of Mn, Zn, and Ca. (c) phase-contrast bright field (BF) STEM image of a grain boundary in Mg-Zn-Ca-Mn alloy with the corresponding EDS elemental maps of Zn and Ca.

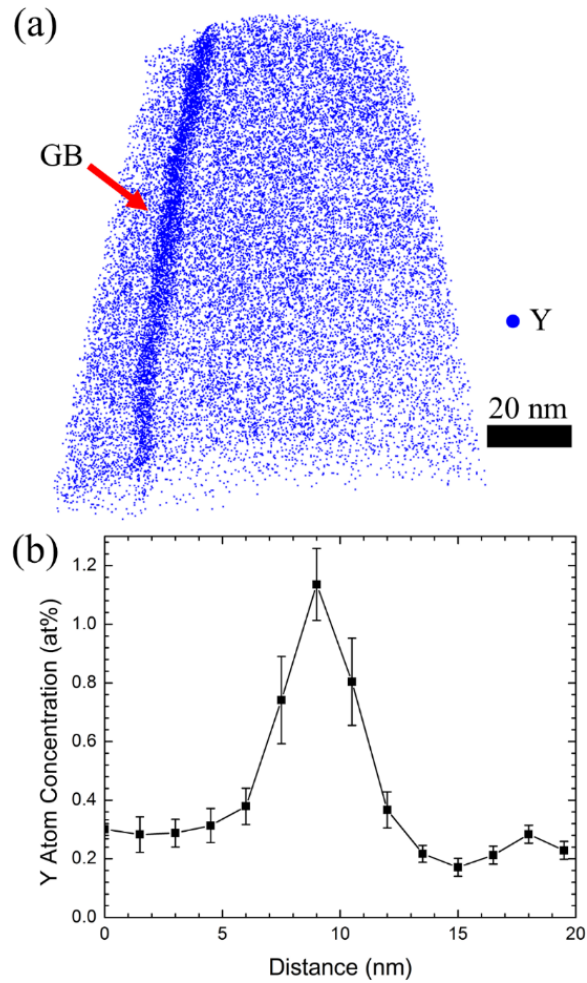


Figure 4.3 (a) APT reconstruction of a volume containing a grain boundary with Y segregation. (b) 1D concentration profile across the grain boundary (obtained using a cylinder of 10 nm diameter).

#### 4.3.2 Localized Corrosion and Hydrogen Evolution Sites

Localized corrosion behavior under free immersion without external polarization was first investigated. **Fig. 4.4** shows the surface morphology of the alloys immersed in 1M NaCl solutions for 1 hour. All investigated alloys exhibited localized corrosion. Localized corrosion on pure Mg propagated with a circular front (**Fig. 4.4(a)**). The circular form of the corrosion front agrees with

prior report on pure Mg under high  $\text{Cl}^-$  concentration [18]. On the Mg-Zn-Ca-Mn alloy, multiple sites initiated localized corrosion with filiform-like tracks spreading over the alloy surface (**Fig. 4.4(b)**). In contrast, localized corrosion on Mg-Y alloy in 1M NaCl appeared as a more continuous region but occurred on certain grains and stopped at grain boundaries (**Fig. 4.3(c)**).

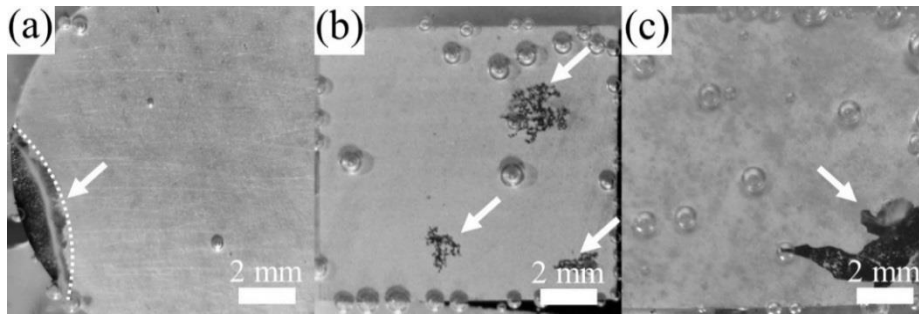


Figure 4.4 Surface corrosion morphology of (a) pure Mg, (b) Mg-Zn-Ca-Mn alloy, and (c) Mg-Y alloys immersed in 1M NaCl solution for 1 hour. White arrows indicate the localized corrosion regions. Dashed curve in (a) marked the circular propagation front.

The large hydrogen bubbles seen in **Fig. 4.4** were explained as originating from local cathodic sites on second phase particles containing impurity elements (**Fig. 4.2(a)**) as described in previous chapters. Higher magnification observations of the propagation fronts of localized corrosion revealed that hydrogen originates at the propagation fronts in all three alloys (**Fig. 4.5**). Little to no hydrogen evolution was observed in the dark filiform-like tracks left behind.

Similar hydrogen evolution behavior is observed under anodic polarization using a 0.1M NaCl solution. **Fig. 4.6** shows the actively propagating localized corrosion regions and hydrogen evolution sites on the Mg-Zn-Ca-Mn alloy that was anodically polarized at  $1 \text{ mA/cm}^2$ . Again, fine

streams of hydrogen bubbles evolved dominantly at the actively propagating localized corrosion fronts. The morphology of localized corrosion on the three alloys after anodic polarization at 10 mA/cm<sup>2</sup> for 100 seconds were qualitatively similar as revealed from the SEM images in **Fig. 4.7**. Localized corrosion under anodic polarization initiated in multiple locations and propagated as filiform-like tracks, similar to those observed on the Mg-Zn-Ca-Mn alloy under free immersion (**Fig. 4.2(b)**). The width of the corrosion tracks was wider on pure Mg than on Mg-Zn-Ca-Mn and Mg-Y alloys.

#### ***4.3.3 Microstructure Characterization of Localized Corrosion Fronts***

Actively propagating localized corrosion fronts, associated with the evolving streams of hydrogen, after both free immersion and anodic polarization were investigated in cross sections by site-specific FIB sectioning. A representative cross section for the Mg-Zn-Ca-Mn alloy after free immersion in 1M NaCl for 1 hour is shown in **Fig. 4.8**. Similar observations were made on pure Mg and Mg-Y alloy after free immersion.

A surface corrosion film about 500 nm to 1  $\mu$ m thick was present on top of the alloy ahead of the localized corrosion region. Localized corrosion appeared to propagate underneath this surface film and inside the alloy. Finger-like morphologies were identified at the propagating corrosion region/alloy interface. The morphology of the bottom interface appeared to follow the alloy grain structure and exhibited a continuous interface, indicating a possible correlation of the localized corrosion propagation with grain boundaries. Further evidence is visible in **Fig. 4.12** below. No film-free region at the propagating corrosion front was observed. The cracks observed in the corrosion products did not extend into the underlying alloy. These cracks likely formed by accumulation and breakout of hydrogen gas in the corrosion products or by dehydration of

Mg(OH)<sub>2</sub> once the samples were taken out of solution. Very similar cross sectional observations were made on the three alloys under anodic polarization (**Fig. 4.9**).

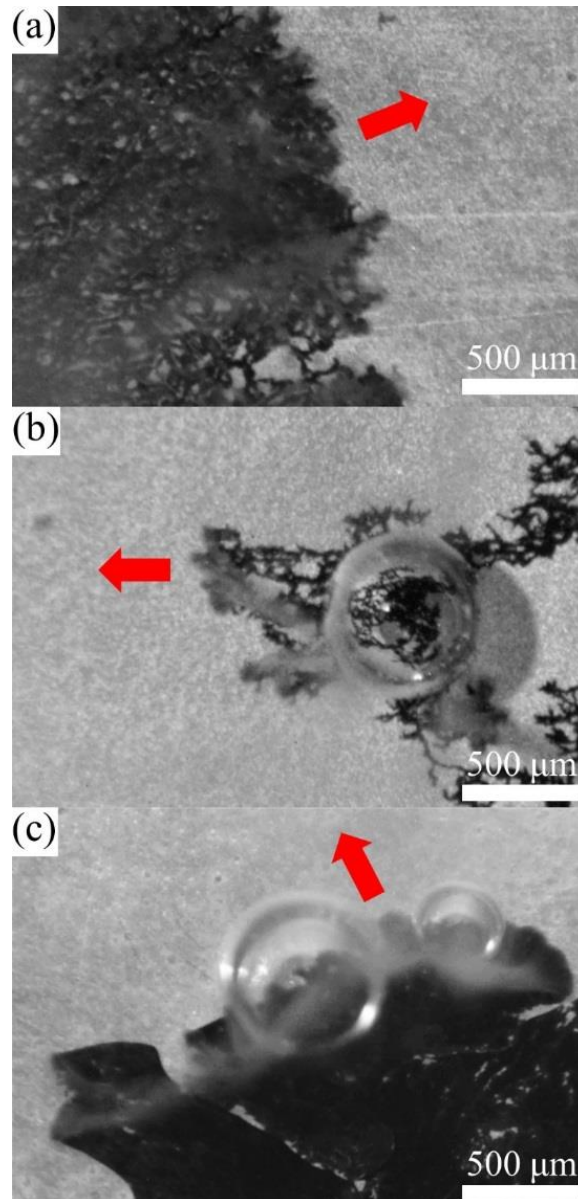


Figure 4.5 High magnification observation of actively propagating fronts of the localized corrosion on (a) pure Mg, (b) Mg-Zn-Ca-Mn, and (c) Mg-Y alloys in 1M NaCl solution. Red arrows indicate the propagation direction of localized corrosion.



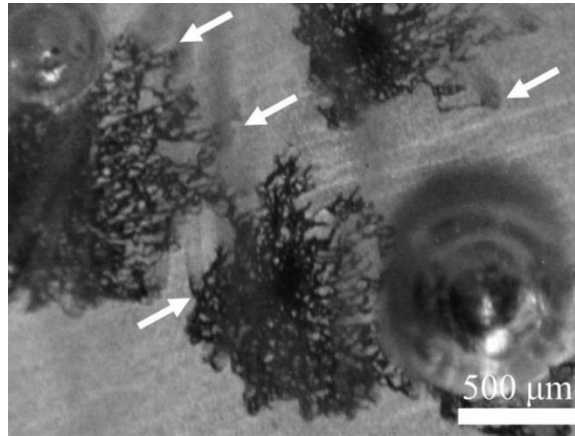


Figure 4.6 High magnification observation of actively propagating localized corrosion regions on Mg-Zn-Ca-Mn alloy in 0.1M NaCl solution under anodic polarization at  $1 \text{ mA/cm}^2$  for 300 seconds. Regions arrowed in the figure indicate some of the hydrogen evolution sites.

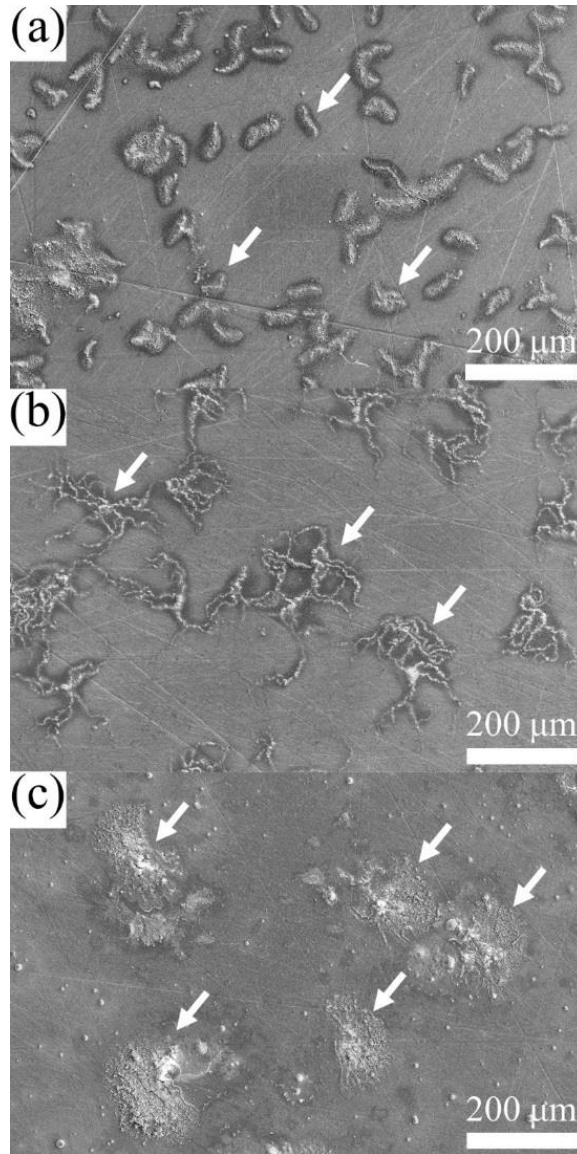


Figure 4.7 Surface corrosion morphology observed by SEM for (a) pure Mg, (b) Mg-Zn-Ca-Mn, and (c) Mg-Y alloys in 0.1M NaCl solution after anodic polarization at  $10 \text{ mA/cm}^2$  for 100 seconds. Regions arrowed in the figure indicate some of the localized corrosion regions. (All images are secondary electron images taken with 5kV electron beam using Everhart-Thornley detector.)

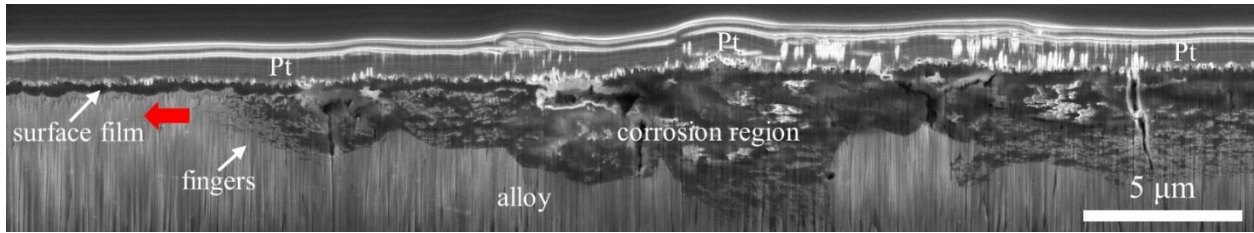


Figure 4.8 Cross sectional SEM image of an actively propagating localized corrosion front on Mg-Zn-Ca-Mn alloy immersed in 1M NaCl solution for 1 hour. The red arrow indicates the propagation direction. (Secondary electron image taken with 5kV electron beam using through lens detector.)

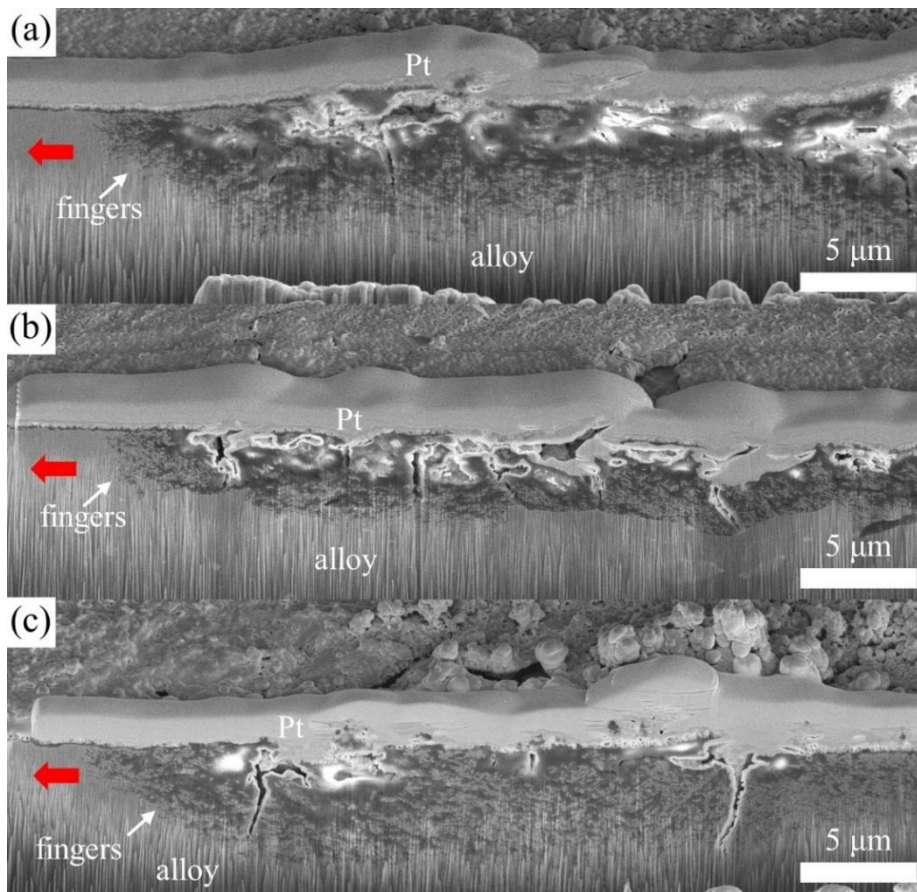


Figure 4.9 Cross sectional SEM image of a propagating localized corrosion region for (a) pure Mg, (c) Mg-Zn-Ca-Mn, and (e) Mg-Y alloys in 0.1M NaCl solution after anodic polarization at 10

$\text{mA/cm}^2$  for 100 seconds. The red arrows indicate the propagation direction. (All images are secondary electron images taken with 5kV electron beam using through lens detector.)

The interaction of localized corrosion propagation with grain boundaries was confirmed by correlative study of EBSD grain orientation mapping and *in-situ* corrosion monitoring. The EBSD grain orientation map of a Mg-Y sample is shown in **Fig. 4.10(b)**. During free immersion in 1M NaCl solution, localized corrosion propagation initiated in one grain on the edge of the sample, propagated across the surface and stopped at some of the grain boundaries (**Fig. 4.10(a)**), which was confirmed by site-specific SEM cross sections (**Fig. 4.10(c)** and **(d)**). After prolonged immersion, localized corrosion crossed the grain boundary and started propagate in the nearby grain, indicating the blocking effect of grain boundary might be temporary. Furthermore, the finger-like features at the localized corrosion/alloy interface exhibit preferential alignment on the (0001) basal planes.

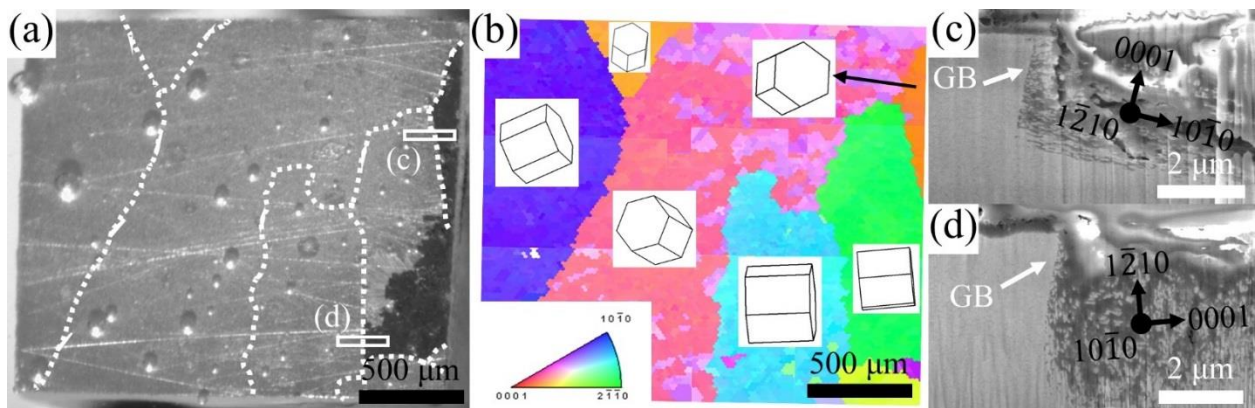


Figure 4.10 (a) Corrosion morphology of a Mg-Y sample after free immersion in 1M NaCl solution for 100 minutes and (b) the corresponding EBSD grain orientation map. (c) and (d) Cross sectional

SEM images of localized corrosion fronts stopping at grain boundaries (secondary electron images taken with 5kV electron beam using through lens detector). Locations of the cross sections are indicated by the white rectangles in (a).

To better understand the microstructure of the propagation front, cross sectional TEM/STEM observations were performed on propagating localized corrosion fronts on the Mg-Zn-Ca-Mn alloy under both free immersion and anodic polarization conditions, as shown in **Fig. 4.11** and **4.12**, respectively. Bright field (BF) TEM (**Fig. 4.11(a)**) revealed a nano-porous structure of the corrosion region, and propagation of localized corrosion underneath a surface film and inside the alloy with finger-like features at the corrosion region/alloy interface was confirmed (**Fig. 4.12(a)**). Electron diffraction analysis revealed the corrosion product has a  $\text{Mg}(\text{OH})_2$  structure (**Fig. 4.11(b)** and **4.12(b)**). STEM/EDS mappings also confirmed that the corrosion region is mainly composed of O and Mg (**Fig. 4.11(e), (f)** and **Fig. 4.12(e), (f)**), while minor amount of Cl was uniformly present (**Fig. 4.11(g)** and **Fig. 4.12(g)**). A Zn enrichment was observed at the interface between the Mg-Zn-Ca-Mn alloy and surface corrosion film for the sample under free immersion (**Fig. 4.11(h)**), which remained visible even after localized corrosion propagated underneath. However, no obvious Zn enrichment was observed at the surface corrosion film/alloy interface on the sample under anodic polarization (**Fig. 4.12(h)**). The reason behind the difference in Zn segregation at the surface film/alloy interface under two different test conditions is unclear. In both cases, no Zn enrichment at the corrosion region/alloy interface was observed. Zn, as well as Ca and Mn, were observed in fine precipitates, with no difference in their size and spatial distribution in the uncorroded alloy and in the localized corrosion region. With the exception of the precipitates,

similar microstructures were observed on pure Mg, Mg-Y alloy, and had been reported in previous chapter on the WE43 alloy after anodic polarization.

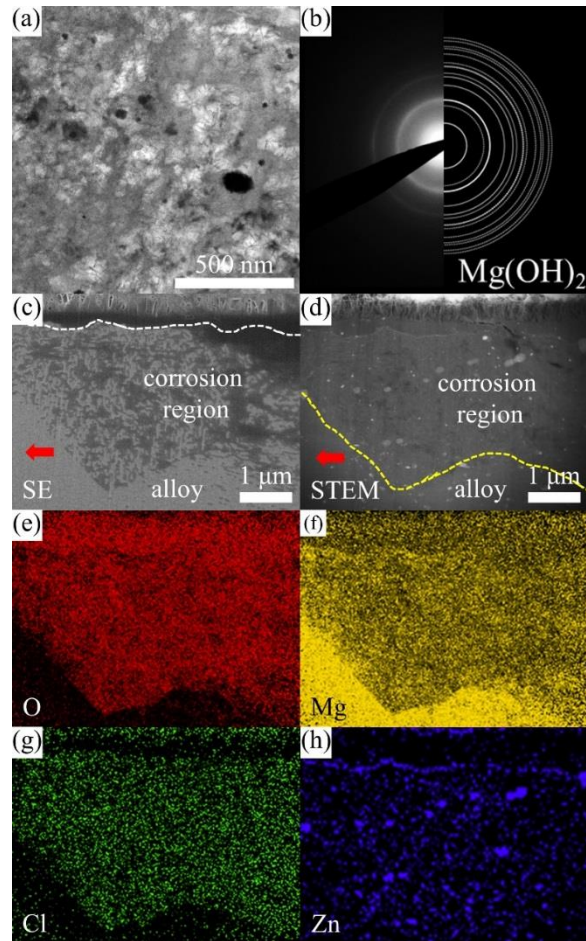


Figure 4.11 (a) High magnification bright field (BF) TEM image of the localized corrosion region on Mg-Zn-Ca-Mn alloys immersed in 1M NaCl solution for 1 hour and (b) the corresponding electron diffraction pattern. The reference  $\text{Mg}(\text{OH})_2$  diffraction ring pattern was generated from Powder Diffraction File 44-1482. Cross sectional (c) secondary electron (SE) and (d) high angle annular dark field (HAADF) STEM image of the active propagating localized corrosion front with the corresponding EDS elemental maps of (e) O, (f) Mg, (g) Cl, and (h) Zn. The red arrows in (c)



and (d) indicate the propagation direction. Dashed lines in (c) and (d) outline the interface between film/localized corrosion region and localized corrosion region/alloy, respectively.

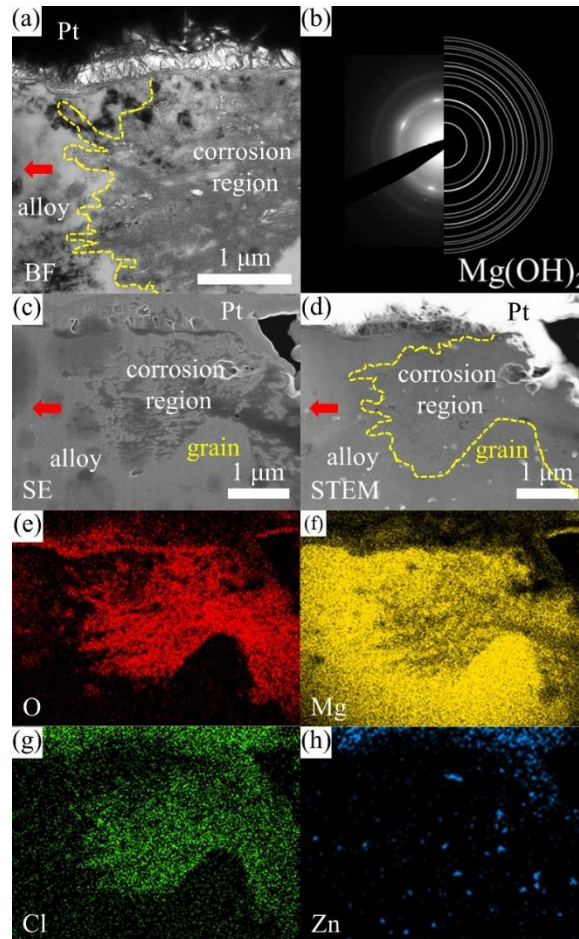


Figure 4.12 Cross sectional (a) bright field (BF) TEM, (c) secondary electron (SE), and (d) high angle annular dark field (HAADF) STEM images of an actively propagating localized corrosion front on Mg-Zn-Ca-Mn alloys in 0.1M NaCl solution after anodic polarization at 10 mA/cm<sup>2</sup> for 100 seconds, and (b) the corresponding electron diffraction pattern of the corrosion region and EDS elemental maps of (e) O, (f) Mg, (g) Cl, and (h) Zn. The reference Mg(OH)<sub>2</sub> diffraction ring pattern was generated from Powder Diffraction File 44-1482. The red arrows in (a), (c), and (d)

indicate the propagation direction. Dashed lines in (a) and (d) outline the interface between localized corrosion region and alloy.

#### ***4.3.4 Hydrogen Evolution Responses under Anodic Polarization***

Hydrogen gas was collected during anodic polarization tests to quantify the hydrogen evolution rate under different conditions. The average hydrogen evolution rates after a total passed charge of 10 C/cm<sup>2</sup> were plotted against the applied anodic current density for all tested alloys (**Fig. 4.13(a)**). A 0.1M Na<sub>2</sub>SO<sub>4</sub> solution was also used to investigate hydrogen evolution response in the absence of chloride ions. For all tested conditions, hydrogen evolution rate increased with increasing applied anodic current density, confirming that the negative difference effect is a universal phenomenon for all tested Mg alloys with and without Cl<sup>-</sup>. However, the hydrogen evolution rate on a particular alloy was always higher in NaCl solutions than in Na<sub>2</sub>SO<sub>4</sub> solutions.

The total amount of Mg<sup>2+</sup> dissolved into the test solution during anodic polarization tests was quantified by ICP-MS. The corrosion product inside the localized corrosion regions and on the alloy surface as corrosion film, which was mainly Mg(OH)<sub>2</sub>, was not dissolved and taken into the quantification. Therefore, the amount of Mg<sup>2+</sup> determined by ICP-MS corresponds to Mg that dissolved into the test solution, and did not form corrosion product or had re-dissolved during the tests. The amount of Mg<sup>2+</sup> was then converted to the unit of current density by assuming each Mg<sup>2+</sup> is directly related to two electrons. The average hydrogen evolution rates were also converted to the unit of current density by assuming ideal gas behavior of hydrogen [28]. These quantified values are summarized in **Fig. 4.13(b)** for the tests at anodic current density of 10 mA/cm<sup>2</sup> after 10 C/cm<sup>2</sup> of charge passed. Under all test conditions, the current density calculated from the amount of Mg<sup>2+</sup> dissolved into the test solution was always comparable to the applied anodic



current density. The current density calculated from the average hydrogen evolution rate, however, varied with both alloy microstructure and solution chemistry.

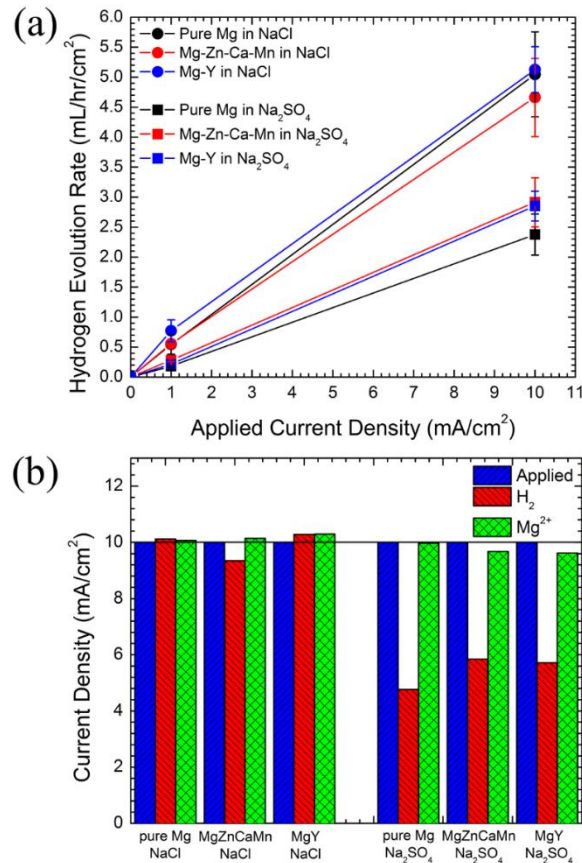


Figure 4.13 (a) Average hydrogen evolution rates of the investigated alloys in 0.1M NaCl and 0.1M Na<sub>2</sub>SO<sub>4</sub> solutions as a function of applied anodic current density. The error bars shown here are the standard deviations of the slopes during collection of hydrogen as described in previous chapter. (b) Comparison of average hydrogen evolution rates and amounts of Mg<sup>2+</sup> dissolved in the test solutions to the applied current density. (A total charge of 10 C/cm<sup>2</sup> was passed for all tests.)

## 4.4 Discussion

The three investigated alloys exhibited localized corrosion when tested under both free immersion and anodic polarization with similar corrosion characteristics. Localized corrosion propagated laterally underneath the surface corrosion film and inside the alloy, which remained shallow in depth with a thickness within 2 and 5  $\mu\text{m}$  depending on alloy grain size. Hydrogen evolution primarily took place at the propagating corrosion fronts. The corrosion products had similar chemistry and porous structure. We will first review these common characteristics in light of the existing literature, before a more general discussion of the corrosion mechanisms and origin of some of the observed differences in corrosion morphologies.

Agreeing with **Chapter 3**, the microstructure of localized corrosion tracks in NaCl solutions was primarily nano-porous  $\text{Mg}(\text{OH})_2$ . While other reports identified a MgO structure [49, 50] or aggregates of nanocrystalline MgO with a porous  $\text{Mg}(\text{OH})_2$  network [51], the presence of MgO as the corrosion products is understood in terms of decomposition of the corrosion products during post-immersion characterization. Indeed, it was shown that the transformation of  $\text{Mg}(\text{OH})_2$  to MgO by dehydration can be mitigated by the use of cryogenic stage during FIB milling (**Appendix I**).

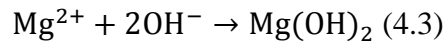
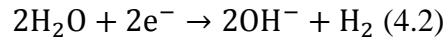
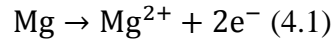
Through careful selection of the characterization locations to correspond to the active propagation sites, the present observations unambiguously revealed that the propagation front was constituted of localized corrosion tracks with finger-like features at the corrosion region/alloy interface. The preferential alignment of the finger-like features is reminiscent of the observed nanoscale canyon-like features developing along the (0001) planes underneath the localized corrosion regions in pure Mg [126] and AZ31 [127]. The discrepancy of interfacial structure with prior reports [49, 50] that highlighted smooth interfaces between alloy and corrosion regions can

be understood by considering the selected analysis locations. These past studies were performed on localized corrosion tracks at least 20  $\mu\text{m}$  away from the propagation fronts, and therefore were no longer the sites of active hydrogen evolution. In fact, this is consistent with the present observations showing a smooth interface along grain boundaries at the bottom of the corrosion layer (**Fig. 4.8** and **4.9(b)**) that is no longer actively propagating. In addition, it may be that the localized corrosion front characterized in Ref. [51] stopped at a grain boundary with Zn segregation, which would be consistent with the present grain boundary chemistry shown in **Fig. 4.2(c)** and **4.8**. However, it is clear that more work is needed to understand the morphology and chemistry of the corrosion microstructure, and the possible role of different Zn concentrations.

Rising streams of hydrogen bubbles always followed the actively propagating localized corrosion fronts (**Fig. 4.5** and **4.6**). This observation not only agrees with past literature on Mg alloys tested under free immersion [34, 44, 45, 53, 54, 90, 91], but also confirmed the observations by Fajardo *et al.* [40, 41, 55] that the abnormal hydrogen evolution on Mg alloys under anodic polarization is primarily associated with regions of anodic dissolution. Even though the cathodic localized corrosion tracks left on the surface could promote localized corrosion propagation by galvanic coupling under free immersion, they are not responsible for the hydrogen evolution observed here.

Comparison of the hydrogen evolution responses under anodic polarization in the presence or absence of chloride ions (0.1M  $\text{Na}_2\text{SO}_4$  solution in this study) showed that  $\text{Cl}^-$  is not necessary for the abnormal increase in hydrogen evolution rate to occur in agreement with prior work [30, 124, 128]. However, the presence of  $\text{Cl}^-$  in the solution promoted the dissolution of Mg under anodic polarization, leading to faster hydrogen evolution rates in each alloy (**Fig. 4.13**).

Because of the commonalities in characterized microstructure and electrochemical quantification, localized corrosion and the hydrogen evolution reaction under anodic polarization can be reasoned as follows for Mg alloys. The corrosion reactions of Mg in aqueous solutions are commonly written as [129]:



Where **reaction 4.1** is the anodic dissolution of Mg, **reaction 4.2** is the cathodic reduction of water and hydrogen evolution, and **reaction 4.3** is the precipitation of Mg(OH)<sub>2</sub> by reaction between Mg<sup>2+</sup> and OH<sup>-</sup>. The incorporation of Cl throughout the corrosion products confirms that propagation of localized corrosion happens by reaction between the alloy and the test solution, requiring ions and water molecules to pass through the porous corrosion products to reach the corrosion region/alloy interface. The balance of electrical flow can also be written as:

$$j_{\text{appl}} + j_{\text{H}_2} = j_{\text{Mg}^{2+}} + j_{\text{Mg}(\text{OH})_2} \quad (4.4)$$

Where  $j_{\text{appl}}$  is the applied anodic current and represents electrons collected by the potentiostat/galvanostat,  $j_{\text{H}_2}$  stands for electrons involved in hydrogen evolution through reduction of water (**reaction 4.2**),  $j_{\text{Mg}^{2+}}$  for Mg<sup>2+</sup> ions dissolved into the test solution measured by ICP-MS, and  $j_{\text{Mg}(\text{OH})_2}$  for the Mg<sup>2+</sup> reacting with OH<sup>-</sup> to form Mg(OH)<sub>2</sub> in the corrosion regions. **Fig. 4.13(b)** shows that  $j_{\text{appl}} \approx j_{\text{Mg}^{2+}}$  for all test conditions, and thus  $j_{\text{H}_2} \approx j_{\text{Mg}(\text{OH})_2}$ , which agrees with prior observations on pure Mg [30, 31]. This last relationship implies that the amount of hydrogen evolution is equal to the amount of localized corrosion products formed.

Comparison between the penetration depths of localized corrosion shown in **Fig. 4.8** and **4.9**, shows that application of anodic polarization did not increase the localized corrosion depth compared to free immersion. However, it promoted localized corrosion by increasing the number of localized corrosion sites (**Fig. 4.4** and **4.7**), and accompanied hydrogen evolution rate.

While the present observations found that the ratio between calculated current density associated with hydrogen evolution and applied current density is close to 1 when tested in NaCl solution (**Fig. 4.13(b)**), it is not always so. A current density ratio between hydrogen evolution and external applied current ( $i_{H_2}/i_{appl}$ ) of about 0.5 to 0.6 was reported on pure Mg [40, 117], Mg-Li alloy [117], and the Mg-Y-Nd-Zr alloy in **Chapter 3**. What controls the rates of dissolution reaction of Mg and associated hydrogen evolution reaction and this ratio is still unclear. However, these alloys differ by their microstructures and chemistry. In fact, the present observations point to the role of alloy microstructure and chemistry. While the overall localized corrosion response is similar for all three alloys, the number density of localized corrosion sites and width of the corrosion tracks differed significantly. Two possible factors are grain size and grain boundary chemistry. The circular propagation front in pure Mg indicates that grain boundaries play no particular role in this material where no solute are present to segregate at grain boundaries. Alternatively, localized corrosion propagation on the Mg-Zn-Ca-Mn and Mg-Y alloys was observed to stop at certain grain boundaries. In both alloys, significant solute segregation to grain boundaries is observed (**Fig. 4.2(c)** and **4.3**), which momentarily stopped the propagation of the corrosion front. We suspect that the windy localized corrosion pattern on Mg-Zn-Ca-Mn compared to the continuous patterns forming on Mg-Y is related to the noticeably smaller grain size of the Mg-Zn-Ca-Mn alloy, however the exact mechanism remains to be clarified.

## 4.5 Conclusions

Site-specific characterization on localized corrosion fronts in three different Mg alloys under both free immersion and anodic polarization conditions in NaCl solutions was performed to understand localized corrosion behavior and underlying mechanisms. The new findings are summarized as follows:

1. Site-specific cross sectional SEM observations and TEM/STEM imaging revealed that the localized corrosion regions under all test conditions were propagating inside the alloy and underneath a surface corrosion film that had formed during immersion. A finger-like morphology with preferential propagation on (0001) planes was identified at the propagating corrosion region/alloy interface.
2. Regardless of the test conditions, rising streams of hydrogen bubbles always evolved at the actively propagating localized corrosion fronts. By electrochemical quantifications, hydrogen evolution under anodic polarization was found to be related to the formation of localized corrosion products and follows local anodic dissolution of Mg.
3. Significant differences were observed in the density of localized corrosion sites, direction of propagation, and in the morphology of the localized corrosion tracks, which appeared to correlate with alloy grain size and grain boundary chemistry.

## **CHAPTER 5:**

### **Summary and Future Directions**

#### **5.1 Summary**

Corrosion behavior in aqueous solutions for pure Mg and Mg alloys with different chemistry and microstructure were investigated with a combination of multiscale characterization techniques and electrochemical analysis. The main findings are summarized as follow:

1. The cathodic Zr-rich impurity particles in Mg-Y-Nd-Zr alloy induced a microgalvanic effect on the alloy, resulting in evolution of large hydrogen bubbles and formation of Mg(OH)<sub>2</sub> corrosion domes on alloy surface. (**Chapter 2**)
2. A bi-layered surface corrosion film structure was revealed on the Mg-Y-Nd-Zr alloy under free corrosion. It consisted of a porous outer Mg(OH)<sub>2</sub> layer on top of an inner MgO layer. (**Chapter 2**)
3. The fine scale precipitates formed after aging treatment in Mg-Y-Nd-Zr alloy interacted with corrosion reaction fronts and slowed down the overall corrosion rate. (**Chapter 2**)
4. Localized corrosion on all investigated alloys consisted of a porous Mg(OH)<sub>2</sub> structure and propagated laterally underneath the surface corrosion film a few μm inside the alloy. A finger-like

morphology, aligned with the (0001) basal planes, was identified at the localized corrosion/alloy interface. (**Chapter 3 and 4**)

5. Segregation of alloying elements to the grain boundaries was found to stop the localized corrosion propagation momentarily. (**Chapter 4**)

6. Rising streams of hydrogen bubbles were found to follow the anodic dissolution of Mg and formation of corrosion products at the localized corrosion fronts, resulting in the observed negative difference effect. (**Chapter 3 and 4**)

Based on the characterized corrosion microstructure, a schematic description for the corrosion behavior on Mg alloys is proposed, as shown in **Fig. 5.1**. The Mg alloy in the illustration (**Fig. 5.1(a)**) contains impurity particles, fine scale precipitates throughout the grain, and segregation of alloying elements to the grain boundaries, which is a typical microstructure for commercial heat-treated Mg alloys. When exposed to air, a natural MgO layer forms on the Mg alloy. After being immersed in aqueous solutions (**Fig. 5.1(b)**), a uniform bi-layered surface corrosion layer forms on the surface, while microgalvanic couples develop between second phases and the Mg matrix. The surface corrosion film thickness on different grains varies because of different corrosion rates. The impurity particles, which contains noble elements, have the highest potential with respect to the Mg matrix. Therefore, a microgalvanic effect is triggered and cathodic reaction preferentially occurs on the impurity particles, resulting in evolving large hydrogen bubbles attached to the surface, local increase in pH, and the formation of Mg(OH)<sub>2</sub> corrosion domes.

At some point, localized corrosion initiates on the alloy surface, and propagates laterally inside the alloy and underneath the surface corrosion film (**Fig. 5.1(c)**). The localized corrosion fronts are focal anodic sites. Rising streams of hydrogen bubbles follow local dissolution of Mg



and evolve at the corrosion fronts. At the localized corrosion/alloy interface, finger-like features develop along the (0001) basal planes. Fine scale precipitates are incorporated into the localized corrosion region and do not impinge the localized corrosion propagation. After further immersion (**Fig. 5.1(d)**), localized corrosion propagation might be stopped by the grain boundaries with alloying element segregation. Meanwhile, the dome structure on top of the impurity particles continues to grow and cathodically protects the surrounding regions.

## **5.2 Future Directions**

### **5.2.1 Corrosion Mechanisms**

Elucidating the detailed mechanism of NDE is crucial to mitigating corrosion and hydrogen evolution response for different applications. We unambiguously showed that the rising streams of hydrogen bubbles, which contributes to the NDE, follow the local anodic dissolution of Mg, however the reaction sequences and species involved are still unclear. Recent computational work simulated the water reduction and hydrogen evolution reaction on the Mg surface to understand the reaction kinetics [130]. However, it was clearly shown that localized corrosion was propagating inside the alloy and underneath the surface corrosion film, implying there is no direct contact of Mg with the solution. The corrosion mechanism is therefore more complicated than simple surface reactions between Mg and water, and the corrosion products also need to be considered. Furthermore, the complex finger-like features at the corrosion fronts might also play an important role in controlling the anodic dissolution and hydrogen evolution reactions by changing the local electric field distribution.

As shown in prior studies [131, 132], the amount of hydrogen evolution under anodic polarization was suppressed when tested in a buffered aqueous solution, indicating the pH value, especially at the propagating localized corrosion fronts where hydrogen was evolving, might play an important role in NDE. As presented in **Chapter 4**, the abnormal hydrogen evolution showed a correlation with the formation of  $\text{Mg}(\text{OH})_2$  localized corrosion products, which is stable only under elevated pH value. Future development of high spatial resolution localized pH monitoring technique, as well as improvement of the spatial resolution of *in situ* localized electrochemical techniques to monitor surface reactions, such as SVET [18, 19] and SECM [32, 33] mentioned in previous chapters, might provide further insights about the NDE mechanism.

Hydrogen evolution rate has long been used as an index for corrosion rate of Mg alloys. However, the widely-applied hydrogen collection method [101] cannot resolve the instantaneous corrosion behavior on Mg alloys. Recent innovations for hydrogen evolution monitoring, such as gravimetric hydrogen measurement [133] and electrochemical balance [134], might uncover the missing information about not only NDE but the general corrosion behavior of Mg alloys.

The results presented in this thesis focused on the short-term corrosion behavior of Mg alloys. However, in field applications, Mg alloys are exposed to corrosive environments for months (biomedical applications) to years (automotive applications). While providing unique insights into the initiation and propagation of corrosion, it is unclear if the results of short-term corrosion tests can be extrapolated to estimate long term corrosion behavior. An open question is for instance whether the corrosion mode changes once the surface is entirely covered by corrosion products. Therefore, long term corrosion behavior will need to be investigated and included in the design of Mg alloys for practical applications.

### ***5.2.2 Alloy Investigation and Design***

Addition of alloying elements is still one of the most important factors that controls the corrosion response of Mg alloys. As reviewed in **Chapter 1**, change in chemistry of Mg can dramatically alter the cathodic and anodic responses of the alloy, resulting in change of corrosion response. Recently, novel Mg alloys with extraordinary high amount of alloying addition, such as Mg-38 at%Ti [135] and Mg-30 wt%Li [136] were produced by sputtering or complex thermo-mechanical process. These alloys can provide crucial information about the effect of different alloying elements and possible route to achieve superior corrosion resistive Mg alloys. Indeed, keeping the amount of alloying addition below the tolerance limit to prevent formation of harmful second phases is one of the most important factors when designing Mg alloys with better corrosion resistance. However, as presented in **Chapter 2**, Nd and Y rich fine scale precipitates do not induce microgalvanic acceleration of corrosion rate but improve the corrosion resistance by interacting with the corrosion reaction front, indicating the formation of second phases is not always harmful to corrosion properties. Similar improvement of corrosion resistance was reported in Mg alloys with finely dispersed long-period short stacking (LPSO) precipitates [137], suggesting a possible route to simultaneously improve the mechanical properties and corrosion resistance of Mg alloys. As presented in **Chapter 4**, grain boundary segregation of alloying elements was shown to stop the localized corrosion propagation momentarily. Therefore, developing a Mg alloy with proper grain boundary segregation might be another possible route of creating an effective corrosion barrier. However, selection of alloying elements and heat treatment might be critical and warrants further investigation. Grain size might not play a dominant role in the corrosion behavior of Mg alloys; however, it is still important to decouple its effect with other factors such as second phases. As reviewed in **Chapter 1**, it was shown that smaller grain size in Mg alloys resulted in slower

corrosion rate. Whether there is a lower limit of grain size that the corrosion rate would stop decreasing is unknown.

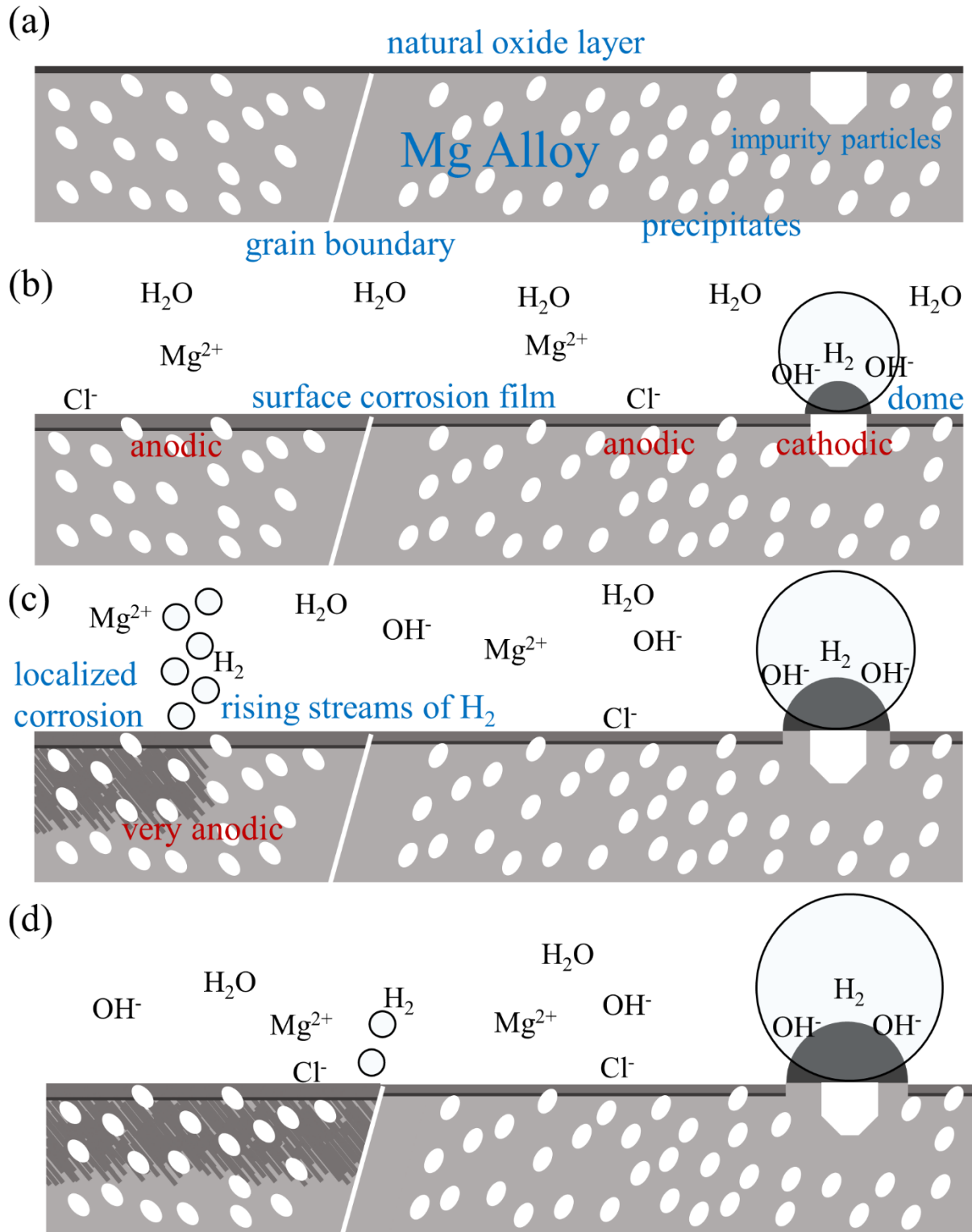


Figure 5.1 Schematic illustration of corrosion mechanism on Mg alloys. (a) to (d) shows the temporal evolution of a Mg alloy immersed in a NaCl solution. The grain on the right shows the

microgalvanic effect induced by the impurity particles, while the grain on the left shows the localized corrosion propagation inside the alloy.

## APPENDICES

### Appendix I Mitigation of Ion and Electron Beam Damage on the Corrosion Film with Cryogenic Stage

It was noted previously [56, 58, 62] that degradation of the surface corrosion film on Mg alloys takes place during TEM observation. Formation of MgO crystals [56, 57] was reported in the corrosion layer after prolonged observation by TEM. To remediate this issue, cryogenic sample stages ( $T \sim 150$  K) for both SEM/FIB and TEM instruments were used to clarify the amount of damage induced by the Ga ion beam and electron beam and properly interpret the observations. **Fig. A.1** compares two cross-sectional TEM liftout samples taken from close locations on the surface corrosion film of a solution-treated WE43 alloy immersed for 1 hour. One sample was thinned using the cryogenic SEM/FIB stage and the other without the stage. The corrosion film is more porous and less crystalline when thinned with the cryogenic stage.

Furthermore, after 40 minutes of continuous TEM observation on the same area at room temperature, i.e. without the TEM cryo-stage, the porosity of the corrosion film decreased dramatically for the cryo-thinned sample, while no significant changes were seen from the film thinned without using the cryogenic stage. This was interpreted as Ga beam milling at room temperature causing significant damage on the corrosion film, therefore further damage by TEM imaging became less obvious than for the cryo-thinned specimen.

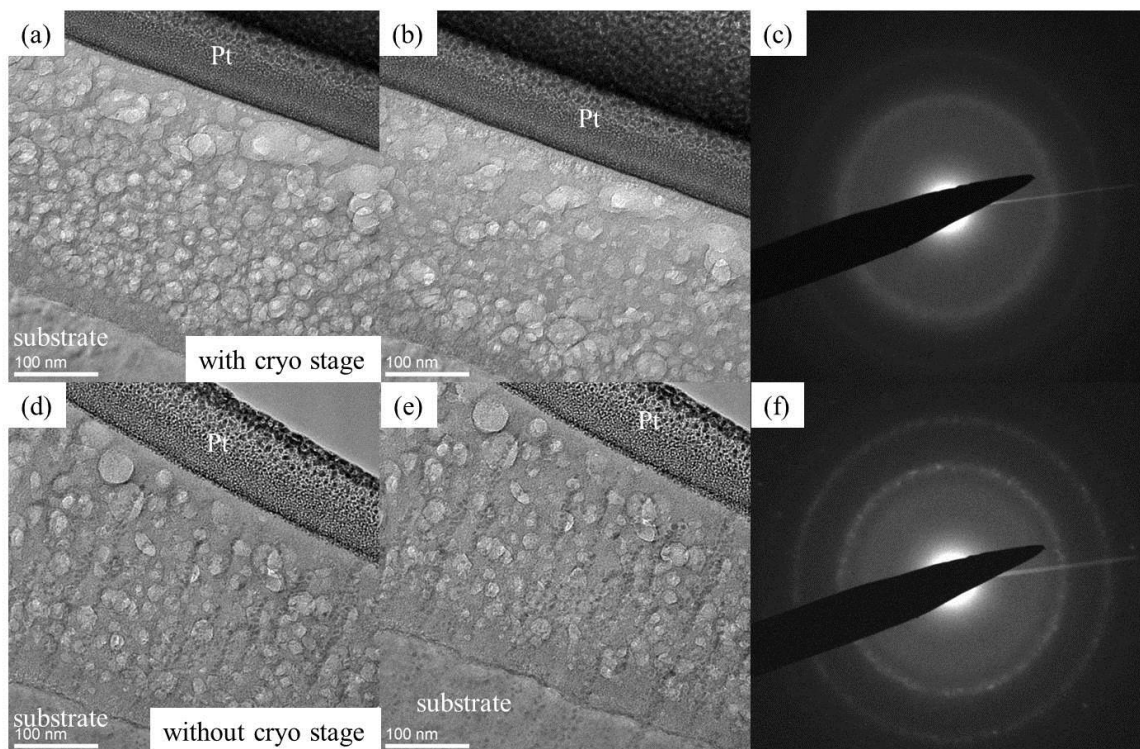


Figure A.1 Ga ion beam damage during cross sectional TEM sample preparation in SEM/FIB. (a) and (d) cross sectional TEM samples prepared with and without cryogenic SEM/FIB stage, respectively, (b) and (e) same region as (a) and (d) after 40 minutes continuous TEM observation, (c) and (f) selected area diffraction pattern for the corrosion film shown in (a) and (d).

In addition of damage introduced during sample preparation, it was also found that observing the corrosion film in STEM mode at room temperature with slow scan rate also caused serious damage on the microstructure of the corrosion film (**Fig. A.2(a) and (b)**). These images were prepared from the region close to the corrosion domes where needle-shaped  $\text{Mg}(\text{OH})_2$  redeposited on top of the surface corrosion film. Scanning focused electron beam across the sample slowly caused big holes to develop throughout the corrosion film, and changed the morphology of



the needle-shaped layer. However, if STEM imaging was performed with a cryogenic TEM stage, these microstructural changes were almost completely suppressed (**Fig. A.2(c)** and **(d)**).

The ion and electron beam induced degradation of the corrosion film is likely due to a combination of beam damage and local heating that accelerated the dehydration reaction of the corrosion film. Therefore, it is highly recommended to use cryogenic stages for both SEM/FIB sample preparation and TEM/STEM observation.

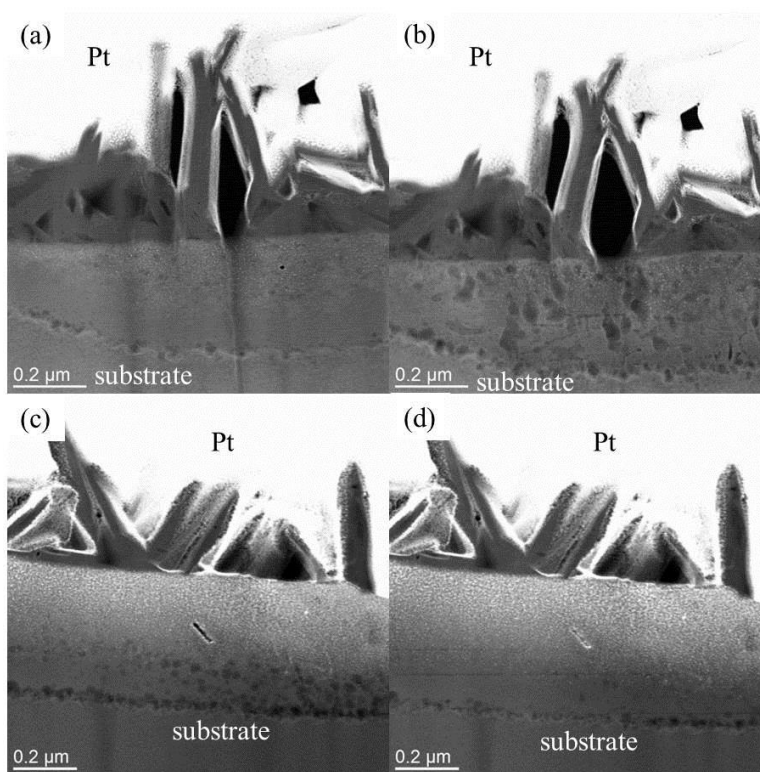


Figure A.2 Electron beam damage during cross sectional STEM observation. (a) and (b) cross sectional images before and after 50 minutes of continuous observation without cryogenic TEM stage, (c) and (d) cross sectional images before and after 50 minutes of continuous observation with cryogenic TEM stage. (Continuous STEM observation parameters: 512x512 with pixel dwell time 1000  $\mu$ s.)

## Appendix II Calibration of X-Ray EDS Quantification with MgO and Mg(OH)<sub>2</sub> Powders in STEM

It was previously argued that the O/Mg ratio obtained from EDS analysis is not reliable and EDS should not be used to infer the nature of the Mg corrosion film because of poor collection efficiency of elements with low atomic numbers for EDS [49]. To bypass this limitation, standard MgO and Mg(OH)<sub>2</sub> TEM specimens from MgO and Mg(OH)<sub>2</sub> powders purchased from Acros Organics were prepared by a liftout method [102] (**Fig. A.3(a)** and **(b)**). X-ray EDS mapping was performed using a Hitachi HD-2300A STEM equipped with an Oxford EDS detector. Analysis was performed using the software built-in  $K_{AB}$  factor values. By averaging over seven different locations on the EDS maps (**Fig. A.3(c)** and **(d)**), the measured O/Mg ratio for MgO and Mg(OH)<sub>2</sub> powders are  $0.9 \pm 0.1$  and  $1.7 \pm 0.1$ , respectively. While not perfect match with the expected values, these measurements clearly show that the two phases can be distinguished using EDS-measured O/Mg ratio. Therefore, we used the same imaging and quantification parameters as those used here.

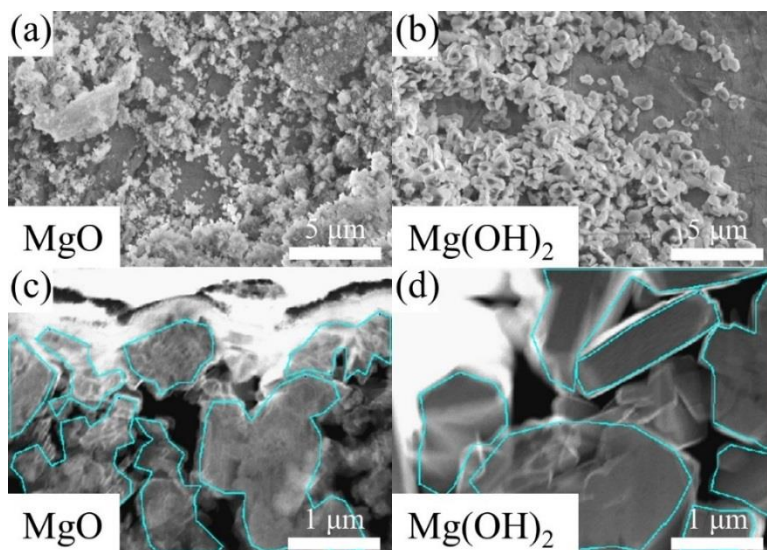


Figure A.3 (a) MgO and (b) Mg(OH)<sub>2</sub> powders used for preparation of TEM specimens, and locations of the EDS quantification (outlined with blue lines) used for O/Mg ratio on (c) MgO and (d) Mg(OH)<sub>2</sub> specimens.

## BIBLIOGRAPHY

- [1] G.L. Makar, J. Kruger, Corrosion of Magnesium, *Int. Mater. Rev.*, 38 (1993) 138-153.
- [2] M.M. Avedesian, H. Baker, *Magnesium and Magnesium Alloys*, ASM International, Park, OH, USA, 1999.
- [3] K.U. Kainer, *Magnesium Alloys and Their Applications*, Wiley Online Library, 2000.
- [4] F. Witte, The History of Biodegradable Magnesium Implants: A Review, *Acta Biomater.*, 6 (2010) 1680-1692.
- [5] N.T. Kirkland, N. Birbilis, M.P. Staiger, Assessing the Corrosion of Biodegradable Magnesium Implants: A Critical Review of Current Methodologies and Their Limitations, *Acta Biomater.*, 8 (2012) 925-936.
- [6] H.D. Yoo, I. Shterenberg, Y. Gofer, G. Gershinsky, N. Pour, D. Aurbach, Mg Rechargeable Batteries: An On-Going Challenge, *Energy & Environmental Science*, 6 (2013) 2265-2279.
- [7] M.-H. Grosjean, M. Zidoune, L. Roué, J.-Y. Huot, Hydrogen Production via Hydrolysis Reaction from Ball-Milled Mg-Based Materials, *International Journal of Hydrogen Energy*, 31 (2006) 109-119.
- [8] M. Esmaily, J.E. Svensson, S. Fajardo, N. Birbilis, G.S. Frankel, S. Virtanen, R. Arrabal, S. Thomas, L.G. Johansson, *Fundamentals and Advances in Magnesium Alloy Corrosion*, *Progress in Materials Science*, 89 (2017) 92-193.
- [9] A. Atrens, W. Dietzel, The Negative Difference Effect and Unipositive Mg+, *Adv. Eng. Mater.*, 9 (2007) 292-297.
- [10] G.S. Frankel, S. Fajardo, B.M. Lynch, Introductory Lecture on Corrosion Chemistry: a Focus on Anodic Hydrogen Evolution on Al and Mg, *Faraday Discuss.*, 180 (2015) 11-33.
- [11] G.L. Song, A. Atrens, Corrosion Mechanisms of Magnesium Alloys, *Adv. Eng. Mater.*, 1 (1999) 11-33.
- [12] N. Winzer, A. Atrens, G.L. Song, E. Ghali, W. Dietzel, K.U. Kainer, N. Hort, C. Blawert, A Critical Review of the Stress Corrosion Cracking (SCC) of Magnesium Alloys, *Adv. Eng. Mater.*, 7 (2005) 659-693.
- [13] E. Ghali, W. Dietzel, K.U. Kainer, General and Localized Corrosion of Magnesium Alloys: A Critical Review, *J. Mater. Eng. Perform.*, 13 (2004) 7-23.
- [14] G.L. Song, Recent Progress in Corrosion and Protection of Magnesium Alloys, *Adv. Eng. Mater.*, 7 (2005) 563-586.
- [15] M. Pourbaix, *Atlas of Electrochemical Equilibria in Aqueous Solutions*, (1974) 139-145.
- [16] T. Cain, L.G. Bland, N. Birbilis, J.R. Scully, A Compilation of Corrosion Potentials for Magnesium Alloys, *Corrosion*, 70 (2014) 1043-1051.
- [17] A. Atrens, G.L. Song, F. Cao, Z.M. Shi, P.K. Bowen, Advances in Mg Corrosion and Research Suggestions, *J. Magnesium Alloy*, 1 (2013) 177-200.
- [18] G. Williams, N. Birbilis, H.N. McMurray, Controlling Factors in Localised Corrosion Morphologies Observed for Magnesium Immersed in Chloride Containing Electrolyte, *Faraday Discuss.*, 180 (2015) 313-330.
- [19] G. Williams, H.N. McMurray, Localized Corrosion of Magnesium in Chloride-Containing Electrolyte Studied by a Scanning Vibrating Electrode Technique, *J. Electrochem. Soc.*, 155 (2008) C340.

- [20] M. Curioni, The Behaviour of Magnesium during Free Corrosion and Potentiodynamic Polarization Investigated by Real-Time Hydrogen Measurement and Optical Imaging, *Electrochim. Acta*, 120 (2014) 284-292.
- [21] M. Curioni, F. Scenini, T. Monetta, F. Bellucci, Correlation between Electrochemical Impedance Measurements and Corrosion Rate of Magnesium Investigated by Real-Time Hydrogen Measurement and Optical Imaging, *Electrochim. Acta*, 166 (2015) 372-384.
- [22] W. Beetz, On the Development of Hydrogen from the Anode, *The London, Edinburgh, and Dublin Philosophical Magazine and Journal of Science*, 32 (1866) 269-278.
- [23] Z.M. Shi, M. Liu, A. Atrens, Measurement of the Corrosion Rate of Magnesium Alloys Using Tafel Extrapolation, *Corros. Sci.*, 52 (2010) 579-588.
- [24] J.W. Turrentine, Reversed Electrolysis, *The Journal of Physical Chemistry*, 12 (1908) 448-467.
- [25] R.L. Petty, A.W. Davidson, J. Kleinberg, The Anodic Oxidation of Magnesium Metal: Evidence for the Existence of Unipositive Magnesium, *Journal of the American Chemical Society*, 76 (1954) 363-366.
- [26] G.L. Song, A. Atrens, Y. Li, B. Zhang, Negative Difference Effect of Magnesium, *Proc. Corrosion and Prevention-97*, Australasian Corrosion Association, Inc, (1997) 38.
- [27] G.L. Song, A. Atrens, Recent Insights into the Mechanism of Magnesium Corrosion and Research Suggestions, *Adv. Eng. Mater.*, 9 (2007) 177-183.
- [28] F. Cao, Z.M. Shi, J. Hofstetter, P.J. Uggowitzer, G.L. Song, M. Liu, A. Atrens, Corrosion of Ultra-High-Purity Mg in 3.5% NaCl Solution Saturated with Mg(OH)<sub>2</sub>, *Corros. Sci.*, 75 (2013) 78-99.
- [29] A. Samaniego, B.L. Hurley, G.S. Frankel, On the Evidence for Univalent Mg, *J. Electroanal. Chem.*, 737 (2015) 123-128.
- [30] J. Swiatowska, P. Volovitch, K. Ogle, The Anodic Dissolution of Mg in NaCl and Na<sub>2</sub>SO<sub>4</sub> Electrolytes by Atomic Emission Spectroelectrochemistry, *Corros. Sci.*, 52 (2010) 2372-2378.
- [31] L. Rossrucker, K.J.J. Mayrhofer, G.S. Frankel, N. Birbilis, Investigating the Real Time Dissolution of Mg Using Online Analysis by ICP-MS, *J. Electrochem. Soc.*, 161 (2014) C115-C119.
- [32] R.M. Souto, A. Kiss, J. Izquierdo, L. Nagy, I. Bitter, G. Nagy, Spatially-Resolved Imaging of Concentration Distributions on Corroding Magnesium-Based Materials Exposed to Aqueous Environments by SECM, *Electrochem. Commun.*, 26 (2013) 25-28.
- [33] U.M. Tefashe, M.E. Snowden, P.D. Ducharme, M. Danaie, G.A. Botton, J. Mauzeroll, Local Flux of Hydrogen from Magnesium Alloy Corrosion Investigated by Scanning Electrochemical Microscopy, *J. Electroanal. Chem.*, 720-721 (2014) 121-127.
- [34] O. Lunder, J.E. Lein, S.M. Hesjevik, T.K. Aune, K. Nişancioğlu, Corrosion Morphologies on Magnesium Alloy AZ91, *Materials and Corrosion*, 45 (1994) 331-340.
- [35] Y.W. Song, D.Y. Shan, R.S. Chen, E.-H. Han, Corrosion Characterization of Mg-8Li Alloy in NaCl Solution, *Corros. Sci.*, 51 (2009) 1087-1094.
- [36] Y.W. Song, D.Y. Shan, R.S. Chen, E.-H. Han, Effect of Second Phases on the Corrosion Behaviour of Wrought Mg-Zn-Y-Zr alloy, *Corros. Sci.*, 52 (2010) 1830-1837.
- [37] M. Liu, P. Schmutz, P.J. Uggowitzer, G.L. Song, A. Atrens, The Influence of Yttrium (Y) on the Corrosion of Mg-Y Binary Alloys, *Corros. Sci.*, 52 (2010) 3687-3701.
- [38] A. Samaniego, I. Llorente, S. Feliu, Combined Effect of Composition and Surface Condition on Corrosion Behaviour of Magnesium Alloys AZ31 and AZ61, *Corros. Sci.*, 68 (2013) 66-71.
- [39] N. Birbilis, A.D. King, S. Thomas, G.S. Frankel, J.R. Scully, Evidence for Enhanced Catalytic Activity of Magnesium Arising from Anodic Dissolution, *Electrochim. Acta*, 132 (2014) 277-283.
- [40] S. Fajardo, G.S. Frankel, Effect of Impurities on the Enhanced Catalytic Activity for Hydrogen Evolution in High Purity Magnesium, *Electrochim. Acta*, 165 (2015) 255-267.
- [41] S. Fajardo, C.F. Glover, G. Williams, G.S. Frankel, The Source of Anodic Hydrogen Evolution on Ultra High Purity Magnesium, *Electrochim. Acta*, 212 (2016) 510-521.
- [42] G. Williams, R. Grace, Chloride-Induced Filiform Corrosion of Organic-Coated Magnesium, *Electrochim. Acta*, 56 (2011) 1894-1903.
- [43] G. Williams, K. Gusieva, N. Birbilis, Localized Corrosion of Binary Mg-Nd Alloys in Chloride-Containing Electrolyte Using a Scanning Vibrating Electrode Technique, *Corrosion*, 68 (2012) 489-498.

- [44] G. Williams, H. ap Llwyd Dafydd, R. Grace, The Localised Corrosion of Mg alloy AZ31 in Chloride Containing Electrolyte Studied by a Scanning Vibrating Electrode Technique, *Electrochim. Acta*, 109 (2013) 489-501.
- [45] Z.P. Cano, J.R. Kish, J.R. McDermid, On the Evolution of Cathodic Activity during Corrosion of Magnesium Alloy AZ31B in a Dilute NaCl Solution, *J. Electrochem. Soc.*, 163 (2016) C62-C68.
- [46] M. Taheri, J.R. Kish, N. Birbilis, M. Danaie, E.A. McNally, J.R. McDermid, Towards a Physical Description for the Origin of Enhanced Catalytic Activity of Corroding Magnesium Surfaces, *Electrochim. Acta*, 116 (2014) 396-403.
- [47] D. Höche, C. Blawert, S.V. Lamaka, N. Scharnagl, C.L. Mendis, M.L. Zheludkevich, The Effect of Iron Re-Deposition on the Corrosion of Impurity-Containing Magnesium, *Physical Chemistry Chemical Physics*, 18 (2016) 1279-1291.
- [48] T. Cain, S.B. Madden, N. Birbilis, J.R. Scully, Evidence of the Enrichment of Transition Metal Elements on Corroding Magnesium Surfaces Using Rutherford Backscattering Spectrometry, *J. Electrochem. Soc.*, 162 (2015) C228-C237.
- [49] Z.P. Cano, M. Danaie, J.R. Kish, J.R. McDermid, G.A. Botton, G. Williams, Physical Characterization of Cathodically-Activated Corrosion Filaments on Magnesium Alloy AZ31B, *Corrosion*, 71 (2015) 146-159.
- [50] Z.P. Cano, J.R. McDermid, J.R. Kish, Cathodic Activity of Corrosion Filaments Formed on Mg Alloy AM30, *J. Electrochem. Soc.*, 162 (2015) C732-C740.
- [51] D. Rossouw, D. Fu, D. Leonard, M.P. Brady, G.A. Botton, J.R. Kish, Characterization of Localized Filament Corrosion Products at the Anodic Head on a Model Mg-Zn-Zr Alloy Surface, *Corrosion*, (2017).
- [52] S.H. Salleh, S. Thomas, J.A. Yuwono, K. Venkatesan, N. Birbilis, Enhanced Hydrogen Evolution on Mg(OH)<sub>2</sub> Covered Mg Surfaces, *Electrochim. Acta*, 161 (2015) 144-152.
- [53] Y. Yang, F. Scenini, M. Curioni, A Study on Magnesium Corrosion by Real-Time Imaging and Electrochemical Methods: Relationship between Local Processes and Hydrogen Evolution, *Electrochim. Acta*, 198 (2016) 174-184.
- [54] M. Curioni, J.M. Torrescano-Alvarez, Y.F. Yang, F. Scenini, Application of Side-View Imaging and Real-Time Hydrogen Measurement to the Investigation of Magnesium Corrosion, *Corrosion*, 73 (2017) 463-470.
- [55] S. Fajardo, C.F. Glover, G. Williams, G.S. Frankel, The Evolution of Anodic Hydrogen on High Purity Magnesium in Acidic Buffer Solution, *Corrosion*, 73 (2017) 482-493.
- [56] J.H. Nordlien, S. Ono, N. Masuko, K. Nisancioglu, Morphology and Structure of Oxide Films Formed on Magnesium by Exposure to Air and Water, *Journal of Electrochemistry Society*, 142 (1995) 3320-3322.
- [57] J.H. Nordlien, S. Ono, N. Masuko, K. Nisancioglu, A TEM Investigation of Naturally Formed Oxide Films on Pure Magnesium, *Corros. Sci.*, 39 (1997) 1397-1414.
- [58] J.H. Nordlien, K. Nişancioğlu, S. Ono, N. Masuko, Morphology and Structure of Oxide Films Formed on MgAl Alloys by Exposure to Air and Water, *J. Electrochem. Soc.*, 143 (1996) 2564-2572.
- [59] J.H. Nordlien, K. Nisancioglu, S. Ono, N. Masuko, Morphology and Structure of Water-Formed Oxides on Ternary MgAl Alloys, *Journal of Electrochemistry Society*, 144 (1997) 461-466.
- [60] M. Danaie, R.M. Asmussen, P. Jakupi, D.W. Shoesmith, G.A. Botton, The Role of Aluminum Distribution on the Local Corrosion Resistance of the Microstructure in a Sand-Cast AM50 Alloy, *Corros. Sci.*, 77 (2013) 151-163.
- [61] M. Danaie, R.M. Asmussen, P. Jakupi, D.W. Shoesmith, G.A. Botton, The Cathodic Behaviour of Al-Mn Precipitates during Atmospheric and Saline Aqueous Corrosion of a Sand-Cast AM50 Alloy, *Corros. Sci.*, 83 (2014) 299-309.
- [62] R.C. Phillips, J.R. Kish, Nature of Surface Film on Matrix Phase of Mg Alloy AZ80 Formed in Water, *Corrosion*, 69 (2013) 813-820.
- [63] K.A. Unocic, H.H. Elsentriecy, M.P. Brady, H.M. Meyer, G.L. Song, M. Fayek, R.A. Meisner, B. Davis, Transmission Electron Microscopy Study of Aqueous Film Formation and Evolution on Magnesium Alloys, *J. Electrochem. Soc.*, 161 (2014) C302-C311.

- [64] F. Zucchi, V. Grassi, A. Frignani, C. Monticelli, G. Trabanelli, Electrochemical Behaviour of a Magnesium Alloy Containing Rare Earth Elements, *J. Appl. Electrochem.*, 36 (2006) 195-204.
- [65] T. Takenaka, T. Ono, Y. Narazaki, Y. Naka, M. Kawakami, Improvement of Corrosion Resistance of Magnesium Metal by Rare Earth Elements, *Electrochim. Acta*, 53 (2007) 117-121.
- [66] K. Gusieva, C.H.J. Davies, J.R. Scully, N. Birbilis, Corrosion of Magnesium Alloys: the Role of Alloying, *Int. Mater. Rev.*, 60 (2015) 169-194.
- [67] N.T. Kirkland, M.P. Staiger, D. Nisbet, C.H.J. Davies, N. Birbilis, Performance-Driven Design of Biocompatible Mg Alloys, *JOM*, 63 (2011) 28-34.
- [68] N. Birbilis, G. Williams, K. Gusieva, A. Samaniego, M.A. Gibson, H.N. McMurray, Poisoning the Corrosion of Magnesium, *Electrochem. Commun.*, 34 (2013) 295-298.
- [69] G. Williams, H.A.-L. Dafydd, H.N. McMurray, N. Birbilis, The Influence of Arsenic Alloying on the Localised Corrosion Behaviour of Magnesium, *Electrochim. Acta*, 219 (2016) 401-411.
- [70] S.N. Xu, M.E. Ikpi, J.H. Dong, J. Wei, W. Ke, N. Chen, Effects of Cadmium alloying on the Corrosion and Mechanical Properties of Magnesium, *International Journal of Electrochemical Science*, 7 (2012) 4735-4755.
- [71] R.L. Liu, M.F. Hurley, A. Kvrnan, G. Williams, J.R. Scully, N. Birbilis, Controlling the Corrosion and Cathodic Activation of Magnesium via Microalloying Additions of Ge, *Scientific Reports*, 6 (2016) 28747.
- [72] M. Nezafati, K. Cho, A. Giri, C.S. Kim, DFT Study on the Water Molecule Adsorption and the Surface Dissolution Behavior of Mg Alloys, *Materials Chemistry and Physics*, 182 (2016) 347-358.
- [73] K.R. Limmer, K.S. Williams, J.P. Labukas, J.W. Andzelm, First Principles Modeling of Cathodic Reaction Thermodynamics in Dilute Magnesium Alloys, *Corrosion*, 73 (2016) 506-517.
- [74] A. Sumer, S. Chaudhuri, A First Principles Investigation of Corrosion Chemistry of Common Elemental Impurities in Mg-Al Alloys, *Corrosion*, 73 (2017) 596-604.
- [75] J.D. Hanawalt, C.E. Nelson, J.A. Peloubet, Corrosion Studies of Magnesium and Its Alloys, *Trans. AIME*, 147 (1942) 273-299.
- [76] D.S. Gandel, M.A. Easton, M.A. Gibson, N. Birbilis, CALPHAD Simulation of the Mg-(Mn, Zr)-Fe System and Experimental Comparison with As-Cast Alloy Microstructures as Relevant to Impurity Driven Corrosion of Mg-Alloys, *Materials Chemistry and Physics*, 143 (2014) 1082-1091.
- [77] A. Prasad, P.J. Uggowitzer, Z.M. Shi, A. Atrens, Production of High Purity Magnesium Alloys by Melt Purification with Zr, *Adv. Eng. Mater.*, 14 (2012) 477-490.
- [78] L. Yang, X.R. Zhou, S.M. Liang, R. Schmid-Fetzer, Z.Y. Fan, G. Scamans, J. Robson, G. Thompson, Effect of Traces of Silicon on the Formation of Fe-Rich Particles in Pure Magnesium and the Corrosion Susceptibility of Magnesium, *J. Alloy Compd.*, 619 (2015) 396-400.
- [79] A.D. Südhol, N.T. Kirkland, R.G. Buchheit, N. Birbilis, Electrochemical Properties of Intermetallic Phases and Common Impurity Elements in Magnesium Alloys, *Electrochem. Solid St.*, 14 (2011) C5-C7.
- [80] N. Birbilis, M.A. Easton, A.D. Sudholz, S.M. Zhu, M.A. Gibson, On the Corrosion of Binary Magnesium-Rare Earth Alloys, *Corros. Sci.*, 51 (2009) 683-689.
- [81] J.H. Liu, Y.W. Song, J.C. Chen, P. Chen, D.Y. Shan, E.H. Han, The Special Role of Anodic Second Phases in the Micro-Galvanic Corrosion of EW75 Mg Alloy, *Electrochim. Acta*, 189 (2016) 190-195.
- [82] Y.W. Song, D.Y. Shan, E.H. Han, Pitting Corrosion of a Rare Earth Mg Alloy GW93, *Journal of Materials Science & Technology*, (2017).
- [83] G.L. Song, A. Atrens, M. Dargusch, Influence of Microstructure on the Corrosion of Diecast AZ91D, *Corros. Sci.*, 41 (1998) 249-273.
- [84] M. Liu, D. Qiu, M.C. Zhao, G.L. Song, A. Atrens, The Effect of Crystallographic Orientation on the Active Corrosion of Pure Magnesium, *Scripta Materialia*, 58 (2008) 421-424.
- [85] K.S. Shin, M.Z. Bian, N.D. Nam, Effects of Crystallographic Orientation on Corrosion Behavior of Magnesium Single Crystals, *JOM*, 64 (2012) 664-670.
- [86] K. Hagihara, M. Okubo, M. Yamasaki, T. Nakano, Crystal-Orientation-Dependent Corrosion Behaviour of Single Crystals of a Pure Mg and Mg-Al and Mg-Cu Solid Solutions, *Corros. Sci.*, 109 (2016) 68-85.

- [87] G.L. Song, R. Mishra, Z.Q. Xu, Crystallographic Orientation and Electrochemical Activity of AZ31 Mg Alloy, *Electrochem. Commun.*, 12 (2010) 1009-1012.
- [88] B.Q. Fu, W. Liu, Z.L. Li, Calculation of the Surface Energy of HCP-Metals with the Empirical Electron Theory, *Appl. Surf. Sci.*, 255 (2009) 9348-9357.
- [89] B.J. Wang, D.K. Xu, J.H. Dong, W. Ke, Effect of the Crystallographic Orientation and Twinning on the Corrosion Resistance of An As-Extruded Mg–3Al–1Zn (wt.%) Bar, *Scripta Materialia*, 88 (2014) 5-8.
- [90] P. Schmutz, V. Guillaumin, R.S. Lillard, J.A. Lillard, G.S. Frankel, Influence of Dichromate Ions on Corrosion Processes on Pure Magnesium, *J. Electrochem. Soc.*, 150 (2003) B99-B110.
- [91] C.R. McCall, M.A. Hill, R.S. Lillard, Crystallographic Pitting in Magnesium Single Crystals, *Corrosion Engineering, Science and Technology*, 40 (2005) 337-343.
- [92] L.G. Bland, K. Gusieva, J.R. Scully, Effect of Crystallographic Orientation on the Corrosion of Magnesium: Comparison of Film Forming and Bare Crystal Facets using Electrochemical Impedance and Raman Spectroscopy, *Electrochim. Acta*, 227 (2017) 136-151.
- [93] K.D. Ralston, N. Birbilis, Effect of Grain Size on Corrosion: A Review, *Corrosion*, 66 (2010) 075005-075005-075013.
- [94] N. Birbilis, K.D. Ralston, S. Virtanen, H.L. Fraser, C.H.J. Davies, Grain Character Influences on Corrosion of ECAPed Pure Magnesium, *Corrosion Engineering, Science and Technology*, 45 (2010) 224-230.
- [95] G.R. Argade, S.K. Panigrahi, R.S. Mishra, Effects of Grain Size on the Corrosion Resistance of Wrought Magnesium Alloys Containing Neodymium, *Corros. Sci.*, 58 (2012) 145-151.
- [96] Y. Lu, A.R. Bradshaw, Y.L. Chiu, I.P. Jones, Effects of Secondary Phase and Grain Size on the Corrosion of Biodegradable Mg–Zn–Ca Alloys, *Materials Science and Engineering: C*, 48 (2015) 480-486.
- [97] B.L. Mordike, Creep-Resistant Magnesium Alloys, *Mat. Sci. Eng. A*, 324 (2002) 103-112.
- [98] G. Riontino, D. Lussana, M. Massazza, A Calorimetric Study of Phase Evolution in a WE43 Mg Alloy, *J Therm. Anal. Calorim.*, 83 (2006) 643-647.
- [99] E. Sitzmann, E.A. Marquis, Chemistry and Morphology of  $\beta'$  Precipitates in an Aged Mg–Nd–Y–Zr Alloy, *Phil. Mag. Lett.*, 95 (2015) 1-7.
- [100] Z.M. Shi, A. Atrens, An Innovative Specimen Configuration for the Study of Mg Corrosion, *Corros. Sci.*, 53 (2011) 226-246.
- [101] G.L. Song, A. Atrens, D. StJohn, An Hydrogen Evolutin Method for the Estimation of the Corrosion Rate of Magnesium Alloys, *Magnesium Technology 2001*, (2001) 255-262.
- [102] L.A. Giannuzzi, F.A. Stevie, A Review of Focused Ion Beam Milling Techniques for TEM Specimen Preparation, *Micron*, 30 (1999) 197-204.
- [103] A.D. Sudholz, K. Gusieva, X.B. Chen, B.C. Muddle, M.A. Gibson, N. Birbilis, Electrochemical Behaviour and Corrosion of Mg–Y Alloys, *Corros. Sci.*, 53 (2011) 2277-2282.
- [104] C. Antion, P. Donnadieu, F. Perrard, A. Deschamps, C. Tassin, A. Pisch, Hardening Precipitation in a Mg–4Y–3RE Alloy, *Acta Mater.*, 51 (2003) 5335-5348.
- [105] G.L. Song, A. Atrens, Understanding Magnesium Corrosion: A Framework for Improved Alloy Performance, *Adv. Eng. Mater.*, 5 (2003) 837-858.
- [106] J. Przondziono, W. Walke, E. Hadasik, J. Szala, J. Wiczorek, Corrosion Resistance Tests of Magnesium Alloy WE43 After Extrusion, *Metalurgija*, 52 (2013) 243-246.
- [107] S. Moon, C. Yang, S.-I. Pyun, A Novel Method to Detect Cathodic Second-Phase Particles in Mg Alloys, *J. Solid State Electr.*, (2015) 1-9.
- [108] A.E. Coy, F. Viejo, P. Skeldon, G.E. Thompson, Susceptibility of Rare-Earth-Magnesium Alloys to Micro-Galvanic Corrosion, *Corros. Sci.*, 52 (2010) 3896-3906.
- [109] J.P. Li, P. Wang, Y.C. Guo, G.E. Thompson, X.R. Zhou, S. Zhong, T. Hashimoto, Microstructure and Microgalvanic Corrosion of an Extruded Mg-10Gd-2Y-0.5Zr Magnesium Alloy, *Mater. Sci. Forum*, 765 (2013) 683-687.
- [110] R.M. Asmussen, W.J. Binns, P. Jakupi, D. Shoesmith, The Influence of Microstructure on the Corrosion of Magnesium Alloy ZEK100, *Corrosion*, 71 (2015) 242-254.



- [111] M. Taheri, R.C. Phillips, J.R. Kish, G.A. Botton, Analysis of the Surface Film Formed on Mg by Exposure to Water Using a FIB Cross-Section and STEM-EDS, *Corros. Sci.*, 59 (2012) 222-228.
- [112] M. Taheri, M. Danaie, J.R. Kish, TEM Examination of the Film Formed on Corroding Mg Prior to Breakdown, *J. Electrochem. Soc.*, 161 (2013) C89-C94.
- [113] M.P. Brady, G. Rother, L.M. Anovitz, K.C. Littrell, K.A. Unocic, H.H. Elsentriecy, G.L. Song, J.K. Thomson, N.C. Gallego, B. Davis, Film Breakdown and Nano-Porous Mg(OH)<sub>2</sub> Formation from Corrosion of Magnesium Alloys in Salt Solutions, *J. Electrochem. Soc.*, 162 (2015) C140-C149.
- [114] M.P. Brady, M. Fayek, H.H. Elsentriecy, K.A. Unocic, L.M. Anovitz, J.R. Keiser, G.L. Song, B. Davis, Tracer Film Growth Study of Hydrogen and Oxygen from the Corrosion of Magnesium in Water, *J. Electrochem. Soc.*, 161 (2014) C395-C404.
- [115] H. Ardelean, A. Seyeux, S. Zanna, F. Prima, I. Frateur, P. Marcus, Corrosion Processes of Mg–Y–Nd–Zr Alloys in Na<sub>2</sub>SO<sub>4</sub> Electrolyte, *Corros. Sci.*, 73 (2013) 196-207.
- [116] G.S. Frankel, A. Samaniego, N. Birbilis, Evolution of Hydrogen at Dissolving Magnesium Surfaces, *Corros. Sci.*, 70 (2013) 104-111.
- [117] A. Samaniego, N. Birbilis, X. Xia, G.S. Frankel, Hydrogen Evolution During Anodic Polarization of Mg Alloyed with Li, Ca, or Fe, *Corrosion*, 71 (2014) 224-233.
- [118] D. Lysne, S. Thomas, M.F. Hurley, N. Birbilis, On the Fe Enrichment during Anodic Polarization of Mg and Its Impact on Hydrogen Evolution, *J. Electrochem. Soc.*, 162 (2015) C396-C402.
- [119] G. Williams, N. Birbilis, H.N. McMurray, The Source of Hydrogen Evolved from a Magnesium Anode, *Electrochem. Commun.*, 36 (2013) 1-5.
- [120] S. Thomas, N.V. Medhekar, G.S. Frankel, N. Birbilis, Corrosion Mechanism and Hydrogen Evolution on Mg, *Curr. Opin. Solid St. M.*, 19 (2015) 85-94.
- [121] Z.M. Shi, J.X. Jia, A. Atrens, Galvanostatic Anodic Polarisation Curves and Galvanic Corrosion of High Purity Mg in 3.5% NaCl Saturated with Mg(OH)<sub>2</sub>, *Corros. Sci.*, 60 (2012) 296-308.
- [122] Z.M. Shi, J.X. Jia, A. Atrens, Galvanostatic Anodic Polarization Curves and Galvanic Corrosion of AZ31B in 0.01 M Na<sub>2</sub>SO<sub>4</sub> Saturated with Mg (OH)<sub>2</sub>, *Adv. Eng. Mater.*, 14 (2012) 324-334.
- [123] Z.M. Shi, J.X. Jia, A. Atrens, Galvanostatic Anodic Polarisation of WE43, *J. Magnesium Alloy*, 2 (2014) 197-202.
- [124] G.L. Song, K.A. Unocic, The Anodic Surface Film and Hydrogen Evolution on Mg, *Corros. Sci.*, 98 (2015) 758-765.
- [125] K. Thompson, D. Lawrence, D.J. Larson, J.D. Olson, T.F. Kelly, B. Gorman, In Situ Site-Specific Specimen Preparation for Atom Probe Tomography, *Ultramicroscopy*, 107 (2007) 131-139.
- [126] L. Yang, X.R. Zhou, M. Curioni, S. Pawar, H. Liu, Z.Y. Fan, G. Scamans, G.E. Thompson, Corrosion Behavior of Pure Magnesium with Low Iron Content in 3.5 wt% NaCl Solution, *J. Electrochem. Soc.*, 162 (2015) C362-C368.
- [127] S. Pawar, T.J.A. Slater, T.L. Burnett, X. Zhou, G.M. Scamans, Z. Fan, G.E. Thompson, P.J. Withers, Crystallographic Effects on the Corrosion of Twin Roll Cast AZ31 Mg Alloy Sheet, *Acta Mater.*, 133 (2017) 90-99.
- [128] G.L. Song, A. Atrens, D. StJohn, X.L. Wu, J. Nairn, The Anodic Dissolution of Magnesium in Chloride and Sulphate Solutions, *Corros. Sci.*, 39 (1997) 1981-2004.
- [129] A. Atrens, G.L. Song, M. Liu, Z.M. Shi, F. Cao, M.S. Dargusch, Review of Recent Developments in the Field of Magnesium Corrosion, *Adv. Eng. Mater.*, 17 (2015) 400-453.
- [130] C.D. Taylor, A First-Principles Surface Reaction Kinetic Model for Hydrogen Evolution under Cathodic and Anodic Conditions on Magnesium, *J. Electrochem. Soc.*, 163 (2016) C602-C608.
- [131] L. Rosrucker, A. Samaniego, J.P. Grote, A.M. Mingers, C.A. Laska, N. Birbilis, G.S. Frankel, K.J.J. Mayrhofer, The pH Dependence of Magnesium Dissolution and Hydrogen Evolution during Anodic Polarization, *J. Electrochem. Soc.*, 162 (2015) C333-C339.
- [132] S. Lebouil, O. Gharbi, P. Volovitch, K. Ogle, Mg Dissolution in Phosphate and Chloride Electrolytes: Insight into the Mechanism of the Negative Difference Effect, *Corrosion*, 71 (2015) 234-241.
- [133] S. Fajardo, G.S. Frankel, Gravimetric Method for Hydrogen Evolution Measurements on Dissolving Magnesium, *J. Electrochem. Soc.*, 162 (2015) C693-C701.

- [134] L. Bottini, M. Santamaria, M. Curioni, Development of an Electrochemical Balance to Measure Quantitatively Hydrogen Generation during Electrochemical Processes, *J. Electrochem. Soc.*, 164 (2017) C618-C625.
- [135] G.L. Song, K.A. Unocic, H. Meyer, E. Cakmak, M.P. Brady, P.E. Gannon, P. Himmer, Q. Andrews, The Corrosion and Passivity of Sputtered Mg–Ti Alloys, *Corros. Sci.*, 104 (2016) 36-46.
- [136] W.Q. Xu, N. Birbilis, G. Sha, Y. Wang, J.E. Daniels, Y. Xiao, M. Ferry, A High-Specific-Strength and Corrosion-Resistant Magnesium Alloy, *Nature Materials*, 14 (2015) 1229-1235.
- [137] S. Izumi, M. Yamasaki, Y. Kawamura, Relation between Corrosion Behavior and Microstructure of Mg-Zn-Y Alloys Prepared by Rapid Solidification at Various Cooling Rates, *Corros. Sci.*, 51 (2009) 395-402.